https://doi.org/10.15388/vu.thesis.835
https://orcid.org/0000-0003-4714-9980

VILNIUS UNIVERSITY
STATE RESEARCH INSTITUTE CENTER FOR PHYSICAL SCIENCE AND TECHNOLOGY (FTMC)

Muhammad Mujahid

Triple Cation Perovskite Layer Fabrication and Investigation of their Optoelectronic Properties for Tandem Solar Cells

DOCTORAL DISSERTATION

Natural Sciences,
Physics (N 002)

VILNIUS 2025

The dissertation was prepared between 2021 and 2025 at State Research Institute Center for Physical Science and Technology.

Academic Supervisor – Prof. Habil. Dr. Steponas Ašmontas (State Research Institute Center for Physical Science and Technology, Natural Sciences, Physics – N 002)

The Doctoral Dissertation will be defended in a Public Meeting of the Dissertation Defence Panel:

Chairman – Prof. Habil. Dr. Saulius Antanas Juršėnas (Vilnius University, Natural Sciences, Physics – N 002).
Members:
Assoc. Prof. Dr. Zigmas Balevičius (State Research Institute Center for Physical Science and Technology, Natural Sciences, Physics – N 002),
Prof. Dr. Algirdas Baškys (State Research Institute Center for Physical Science and Technology, Technology Sciences, Electrical and Electronic Engineering – T 001),
Dr. Marius Franckevicius (State Research Institute Center for Physical Science and Technology, Natural Sciences, Physics – N 002),
Assoc. Prof. Dr. Pavels Onufries (Riga Technical University, Natural Sciences, Physics – N 002)

The dissertation shall be defended at a public meeting of the Dissertation Defence Panel at 11:00 AM (hour)/ on 15 October 2025 in room D401 of the State Research Institute Center for Physical Science and Technology.
Address: Sauletekio al. 3, LT-10257, Vilnius, Lithuania
Tel. +37064515550; e-mail: office@ftmc.lt

The text of this dissertation can be accessed at the libraries of Vilnius University, as well as on the website of Vilnius University:
www.vu.lt/lt/naujienos/ivykiu-kalendorius

https://doi.org/10.15388/vu.thesis.835
https://orcid.org/0000-0003-4714-9980

VILNIAUS UNIVERSITETAS
VALSTYBINIS MOKSLINIŲ TYRIMŲ INSTITUTAS FIZINIŲ IR TECHNOLOGIJOS MOKSLŲ CENTRAS

Muhammad Mujahid

Trigubo katijoninio perovskito sluoksnio gamyba ir jų optoelektroninių savybių tyrimas tandeminiams saulės elementams

DAKTARO DISERTACIJA

Gamtos mokslai
Fizika (N 002)

VILNIUS 2025

Disertacija rengta 2021_–2025_ metais Valstybinio mokslinių tyrimų instituto Fizinių ir technologijos mokslų centre.

Mokslinis vadovas – prof. habil. dr. Steponas Ašmontas (Valstybinis mokslinių tyrimų institutas, Fizinių ir technologijos mokslų centras, gamtos mokslai, fizika – N 002).

Gynimo taryba:
Pirmininkas – prof. habil. dr. Saulius Antanas Juršėnas (Vilniaus universitetas, gamtos mokslai, fizika – N 002).
Nariai:
doc. dr. Zigmas Balevičius (Valstybinis mokslinių tyrimų institutas, Fizinių ir technologijos mokslų centras, gamtos mokslai, fizika – N 002),
prof. dr. Algirdas Baškys (Valstybinis mokslinių tyrimų institutas, Fizinių ir technologijos mokslų centras, technologijos mokslai, elektros ir elektronikos inžinerija – T 001),
dr. Marius Franckevičius (Valstybinis mokslinių tyrimų institutas, Fizinių ir technologijos mokslų centras, gamtos mokslai, fizika – N 002),
doc. dr. Pavels Onufries (Rygos technikos universitetas gamtos mokslai, fizika – N 002).

Disertacija ginama viešame Gynimo tarybos posėdyje 2025_ m. _spalio mėn. 15 d. _11 val. Fizinių ir technologijos mokslų centro D401 salėje Adresas: Saulėtekio al. 3, LT - 10257 Vilnius, Lietuva, tel. +37064515550; el. paštas office@ftmc.lt

Disertaciją galima peržiūrėti Vilniaus bibliotekoje ir VU interneto svetainėje adresu: https://www.vu.lt/naujienos/ivykiu-kalendorius

ABBREVIATIONS

PV	photovoltaic
PSCs	Perovskite solar cells
SC	Solar cell
PCE	power conversion efficiency
$CaTiO_3$	calcium titanate
$MAPbI_3$)	methylammonium lead iodide
Cs	cesium
Rb	rubidium
FA	formamidinium
MA	methylammonium
ETL	electron transport layers
TSC	tandem solar cell
CO_2	carbon dioxide
Se	selenium
Pt	Platinum
Au	gold
LEDs	light-emitting diodes
P_m	maximum power point
I	currents
V	voltages
FF	fill factor
I_{sc}	short circuit current
V_{oc}	open circuit voltage
mc-Si	monocrystalline silicon
poly-Si	polycrystalline
a-Si	amorphous silicon
CIGS	copper indium gallium selenide
CdTe	cadmium telluride
BIPV	building-integrated PVs
Si	Silicon
Ge	Germanium
DSSCs	dye-sensitized solar cells
ETA	extremely thin absorber
Spiro-MeOTAD	2, 2′, 7, 7′-tetrakis(N,N dimethoxypheny lamino)-9,9′spirobifluorene
DFT	density functional theory
PL	photoluminescence

UV	ultraviolet
Eg	bandgap energy
MPSCs	Mesoporous PSCs
FTO	fluorine-doped tin oxide
PPSCs	planar PSCs
VBM	valence band maximum
CBM	conduction band maximum
HTMs	hole-transporting materials
SHJ	Si heterojunction
DOS	density of states
HC	hot carriers
HOMO	highest occupied molecular orbital
LUMO	lowest unoccupied molecular orbital
IGZO	indium-gallium-zinc oxide
ZnO	zinc oxide
TiO_2	titanium dioxide
SnO_2	tin oxide
PCBM	6,6-phenyl-C61-butyric acid methyl ester
MPPT	maximum power point tracking
LO	longitudinal optical
EDOS	electron density of states
SQ	Shockley-Queisser
ETJ	epitaxial tunnel junction
SPT	series-parallel tandem
WB	wide band
NB	narrow band
TCO	transparent conductive oxide
IEC	International Electrotechnical Commission
ISOS	International Summit on Organic Stability
MgF_x	magnesium fluoride
LiF	lithium fluoride
$FAPbI_3$	formamidinium lead iodide
J_{SC}	short-circuit current densities
DMF	N, N-Dimethylformamide
ITO	Indium tin oxide
PbI_2	lead iodide
PVD	Physical vapor deposition
QCM	quartz crystal thickness monitors
SEM	Scanning electron microscopy

SE	Secondary electrons
BSE	backscattered electrons
EDX	Energy Dispersive X-ray
TRPL	transient PL
TPV	Transient PV
SMU	source measurement unit
J–V	Current-voltage
DMSO	dimethylsulfoxide
CsI	Cs iodide
CB	chlorobenzene
TBP	4-tert-butylpyridine
XRD	X-ray diffraction
Li-TFSI	Li-bis ((trifluormetil) sulfonil) imido

CONTENTS

ACKNOWLEDGMENT

I would like to thank most sincerely my supervisor, Prof. Dr. Steponas Ašmontas, whose unconditional support, profound advice, and strictness in scientific matters led to the formation of this work in all its constituent aspects. His passion for researching perovskite solar cells has motivated me to push beyond my limits and venture into a new dimension of science. The time I spent with him was a huge honor and a significant privilege that helped him grow under his supervision.

I would like to thank the State Research Institute of Physical Sciences and Technology (FTMC) for providing me with the opportunity, resources, and support to conduct this research, as well as for fostering a collaborative environment. The exceptional facilities and thought-provoking academic community provided by the institute have played a pivotal role in enriching my studies.

I would also like to thank my coworkers, Aurimas Ceskus, Jonas Gradauskas, Asta Griguceviene, Andzej Lucun, and Edmundas Sirmulis, who are also my friends, for openly discussing some issues and providing practical assistance in the laboratory. Specifically, I would also like to express a special debt of gratitude to Oleksandr Masalskyi and Ihor Zharchenko, who accompanied me on this trip over the last four years and helped me endure even the most complicated situations with their constant support and friendship.

I would also like to thank my Supervisor for the Master's degree, Prof. Dr. Duan Yu, who introduced me to the wonderful world of perovskites and allowed me to investigate their potential in his research laboratory. This thesis is built on the encouragement he received at an early age.

Lastly, my family to whom I owe it all. To my parents, who had the emotional foundation of this undertaking, a quiet, steady faith in me, to which I owe, unconsciously, but irrevocably, a debt of gratitude. And to my wife, who, through her unlimited patience, understanding, and love, provided me the impetus to write this work, without whom this work would not have been possible.

CV

Name:	Muhammad
Surname:	Mujahid
Email:	Muhammad.mujahid@ftmc.lt

Education:

2011-2015	B.E Electronics Quaid-e-Awam University of Engineering Sciences and Technology, Nawabshah, Pakistan.
2018-2021	Master of Science (Microelectronics and Solid State Electronics) State Key Laboratory on Integrated Optoelectronics, Jilin University, China

Work Experience:

2015-2017	Junior Lecturers Punjab College University Campus (University of Central Punjab)
2022-Till date	Junior Researcher State Research Institute for Physical Science and Technology (FTMC), Vilnius, Lithuania

1. INTRODUCTION

Solar energy has emerged as a prominent alternative to conventional fossil fuel-based energy sources in response to growing global energy demands and the need to mitigate environmental issues, including pollution and climate change [1]. Amid growing interest in renewable energy systems, solar photovoltaic (PV) technology is distinguished by its capacity to directly transform solar energy into electricity without causing environmental degradation or depleting natural resources. Perovskite solar cells (PSCs) have garnered significant attention from researchers among the diverse photovoltaic technologies due to their exceptional optoelectronic properties, cost-effective processing, straightforward fabrication, and rapidly improving power conversion efficiency (PCE). The history of perovskite compounds dates back to 1839 when German mineralogist Gustav Rose first identified calcium titanate ($CaTiO_3$) and named it in honor of Russian mineralogist Lev Perovski [2]. Despite substantial research on perovskite structures across various applications, including catalysis, superconductors, and ferroelectrics, its potential utility in PVs remained primarily overlooked until recently. A significant advancement occurred in 2009 when Kojima et al. documented the practical application of methylammonium lead iodide ($MAPbI_3$) as an active photovoltaic (PV) absorber material, achieving encouraging initial efficiencies [3]. The breakthrough generated significant research interest, leading to vigorous development operations in PSC technology.

Following this foundational study, intensive research endeavors have focused on optimizing perovskite composition and fabrication processes, resulting in efficiency gains that exceed and reduce the gap with conventional silicon-based PVs. Despite these advancements, single-cation perovskite compositions demonstrated inherent stability and performance constraints under operational settings [4]. Mixed-cation perovskites were developed to mitigate these constraints, resulting in substantial improvements in stability, efficiency, and a reduction in hysteresis effects. Recent advancements have highlighted triple cation perovskites, including cesium (Cs), formamidinium (FA), and methylammonium (MA), as particularly advantageous due to their enhanced optoelectronic capabilities, superior structural stability, and increased environmental resilience [5].

Triple-cation perovskite compositions have enhanced performance metrics, particularly in tandem solar cell (TSC) topologies [5, 6]. These utilize various PV materials to harness more sunlight, thereby elevating

overall solar cell efficiency beyond the thresholds of single-junction devices. Incorporating triple-cation perovskites into TSCs entails sophisticated production and characterization procedures. To achieve optimal performance, it is essential to meticulously regulate the shape, thickness, and homogeneity of each perovskite layer. Moreover, comprehending the complex charge transport dynamics and recombination processes in these novel perovskite structures is essential for optimizing efficiency and stability.

This thesis thoroughly addresses the fundamental problems by achieving the production and characterization of customized triple-cation perovskite films for TSC applications. The project involves integrating sophisticated deposition processes, including spray pyrolysis for the deposition of electron transport layers (ETL) and spin-coating methods for the deposition of perovskite absorbers and hole transport layers (HTL). The experimental techniques encompass comprehensive optical and electrical characterizations, including absorption spectroscopy, transmittance assessments, transient photovoltage evaluations, and rigorous PV performance studies. This extensive study aims to elucidate the essential mechanisms of charge formation, transport, and recombination in triple-cation perovskite layers. This finding is expected to substantially enhance the advancement of efficient, stable, and commercially viable perovskite TSCs. This research directly contributes to the overarching objective of transitioning to renewable and sustainable energy systems, tackling essential global concerns in energy security and environmental sustainability. This work signifies a significant advancement toward the practical and extensive adoption of advanced PV technology in the renewable energy sector.

1.1. Aim of the Thesis

This thesis aims to synthesize triple-cation perovskite layers and comprehensively investigate their optoelectronic properties, specifically designed for use in high-performance TSCs. The research will enhance performance metrics, including efficiency, stability, and reproducible results, by developing and refining novel fabrication processes. To improve PV efficiency, a primary goal is to clarify the interaction among various solar cell layers, including the electron transport layer (ETL), the perovskite absorber, and the hole transport layer (HTL).

Furthermore, the thesis aims to comprehensively elucidate and identify critical elements that affect the optoelectronic properties of triple-cation perovskite films. The research uses advanced experimental techniques to

investigate charge carrier transit, absorption mechanisms, transmittance characteristics, and recombination processes. These outcomes will substantially enhance the technological advancements and market feasibility of perovskite-based PV systems.

1.2. Tasks of the research project

Develop and enhance techniques for producing triple cation perovskite layers.

Fabricate the electron transport layer utilizing spray pyrolysis and spin coating techniques.

Using spin coating, produce perovskite and hole transport layer in an inert glovebox environment.

Conduct optical characterization, encompassing absorption and transmittance assessments.

Assess the PV performance by measuring the efficiency metrics of the solar cells produced.

Conduct a comprehensive analysis and evaluate findings to identify performance limitations and propose targeted improvements.

1.3. Thesis Statements

- The transient photovoltage measurements in single-junction perovskite solar cells allow the detection of the presence of hot carriers and their influence on photovoltage generation. The photovoltage induced across the solar cells under pulsed laser excitation consists of two components having opposite polarities. The fast component follows the laser pulse shape and is caused by the heating of charge carriers by light, and the slow component is the typical photovoltage resulting from electron-hole pair generation.
- The negative impact of hot carriers on the power conversion efficiency of perovskite solar cells can be mitigated by reducing the band bending near the charge transport layers or by employing a multi-junction cell structure, which better utilizes the solar spectrum and minimizes the thermalization losses.
- The addition of tin to lead halide perovskite materials reduces the power conversion efficiency of solar cells due to a reduced bandgap and an increase in the number of non-radiative defects and surface recombination rate.

1.4. Relevance

The experiments carried out in this thesis have utilized perovskite layers, as described by Burshka et al.[7] and Saliba et al.[8] Based on these tested techniques, the thesis addresses the current gaps in existing knowledge and provides a detailed exploration of the photophysical mechanisms in single-junction perovskite solar cells. It was found that when a single-junction perovskite solar cell is illuminated with a short laser pulse, the induced photovoltage consists of two components of opposite polarity. The fast component is aligned by the light heating of the charge carriers, and the slow component is the photovoltage resulting from the generation of electron-hole pairs.

The thesis proposes strategies to mitigate the negative impact of hot charge carriers on the energy conversion efficiency of perovskite solar cells. It is proposed to reduce band bending at charge transfer interfaces or to utilize multi-junction structures to more effectively utilize the entire solar spectrum and minimize losses due to thermalization.

The findings indicate that the reductions in bandgap and proliferation of non-radiative defects triggered by tin addition cause a significant drop in power conversion efficiency, which is primarily attributed to the unfavorable effects on open-circuit voltage and short-circuit current due to elevated surface recombination rates.

The research results presented in this dissertation expand the existing knowledge base on the performance-limiting factors of perovskite solar cells, providing insights into how the cell architecture and composition can be optimized to overcome these challenges.

1.5. List of Scientific Publications

P1. Ašmontas S., Gradauskas J., Griguceviciene A., Leinartas K., Lucun A., Mujahid* M., Petrauskas K., Selskis A., Sužiedėlis A., Šilėnas A., and Širmulis E., Triple-cation perovskite/silicon tandem solar cell, *Ukrainian Journal of Physical Optics* (2022), Vol. 23, Issue 4, pp. 193 – 200. Q2 (IF: 3.9)

P2. Steponas Ašmontas, Muhammad Mujahid*, Recent Progress in Perovskite Tandem Solar Cells, *Nanomaterials* (2023), **13**(12), 1886. Q2 (IF: 4.3)

P3. Muhammad Mujahid*, Aurimas Čerškus, Jonas Gradauskas ,Asta Griguceviˇcienė, Raimondas Giraitis, Konstantinas Leinartas, Andžej Lučun 1,Kazimieras Petrauskas, Algirdas Selskis, Algirdas Sužiedėlis, Aldis

Šilėnas, Edmundas Širmulis, Steponas Ašmontas. Unveiling the Influence of Hot Carriers on Photovoltage Formation in Perovskite Solar Cells, *Materials* 2025, **18**(1), 85. Q2, (IF: 3.2)

P4. Muhammad Mujahid *, Jonas Gradauskas, Algirdas Sužiedelis ˙, Edmundas Širmulis and Steponas Ašmontas *, Recent Advancements in Understanding Hot Carrier Dynamics

in Perovskite Solar Cells, Energies 2025, 18(13), 3543. Q1 (IF=3.1)

Other Publications by the author not included in the dissertation

P1. "Progress of High-Throughput and Low-Cost Flexible Perovskite Solar Cells"

Muhammad Mujahid, Chen Chen, Wei Hu, Zhao-Kui Wang, Yu Duan DOI: 10.1002/solr.201900556, Journal: Solar

RRL, Volume 04, Issue 08, Page 1900556, 17 January 2020, (IF =9.173).

P2. "A Review of Perovskites Solar Cell Stability" Rui Wang, Muhammad Mujahid, Yu Duan, Zhao-Kui Wang, Jingjing Xue, and Yang Yang, DOI: 10.1002/adfm.201808843, Journal: Advanced Functional Materials, Volume 29, Issue 47, Page 1808843, 12 February 2019, (IF=18.808)

P3. "White Light-Emitting Devices Based on Inorganic Perovskite and Organic Materials"

Shuming Chen, Chen Chen, Cong Bao, Muhammad Mujahid, Ye Li, Ping Chen, and Yu Duan, DOI:10.3390/molecules24040800, Journal: Molecules, Volume 24, Issue 04, Page 800, 22 February 2019 (IF=4.927)

P4. "Hybrid perovskite charge generation layer for highly efficient tandem organic light-emitting diodes" Cong Bao, Chen Chen, Mujahid Muhammad, Xingjuan Ma, Zhaokui Wang, Yunfei Liu, Ping Chen, Shuming Chen, Bin Liu, Jintao Wang, Yu Duan, DOI: 10.1016/j.orgel.2019.06.022, Journal: Organic electronics, Volume 73, Page 299, October 2019, (IF=3.868)

P5. "A Novel Nucleation Inducer for Ultrathin Au Anodes in High Efficiency and Flexible Organic Optoelectronic Devices" Haoran Wang, Zhenyu Wang, Xiangchen Xu, Wenzhuo Zhao, Dan Wu, Mujahid Muhammad, Yunfei Liu, Chen Chen, Bin Liu, and Yu Duan, DOI: 10.1002/adom.201901320, Journal: Advanced Optical Materials, Volume 08, Issue 04, Page 1901320, 18 December 2019 (IF=10.050)

P6. "Surface functionalization of graphene cathode to facilitate ALD growth of electron transport layer and realize highperformance flexible perovskite solar cells"

Xiangchen Xu, Haoran Wang, Jintao Wang, Mujahid Muhammad, Zhenyu Wang, Ping Chen, Wenzhuo Zhao, Bonan Kang, Jian Zhang, Chuannan Li, and Yu Duan, DOI: 10.1021/acsaem.9b02191, Journal: ACS Applied Energy Material, Volume 03, Issue 05, Page 4208, April 28, 2020, (IF=6.024)

P7. "Recent advances in semitransparent perovskite solar cells" Muhammad Mujahid, Chen Chen, Jian Zhang, Professor, Chuannan Li Professor, Yu Duan Professor, DOI: 10.1002/inf2.12154, Journal: Infomat, Volume 03, Issue 01, Page 101, 18 May 2020, (IF=24.798)

P8. Processing and preparation method for high-quality opto-electronic perovskite film,

Zheng Chen, Ping He, Dan Wu, Chen Chen, Muhammad Mujahid, Ye Li, Yu Duan. DOI:

10.3389/fmats.2021.723169 Journal: Frontiers in Materials, Volume 8, Page 723169 (IF=3.515)

1.6. Conferences

C1. Muhammad Mujahid*, Steponas Ašmontas. Triple cation perovskite/silicon tandem solar cell, *Apropos 18 Conference,* Sauletekio av. 3 Vilnius, Lithuania, 5-7 October 2022.

C2. M.Mujahid*, Ašmontas S. Triple cation perovskite/silicon tandem solar cell, *FizTech2022 conference*, Sauletekio av. 3 Vilnius, Lithuania, 19 – 20 October, 2022.

C3. Muhammad Mujahid*. A Road Map to Perovskite Perovskite Tandem Solar Cells. *13th Conference of Doctoral Students and Young Scientists FizTeCh-2023*, Sauletekio av. 3 Vilnius, Lithuania, 18 October 2023.

C4. S. Ašmontas, A. Čerškus, J. Gradauskas, A. Grigucevičienė, R. Juškėnas, K. Leinartas, A. Lučun, O. Masalskyi, M. Mujahid*, K. Petrauskas, A. Selskis, A. Sužiedėlis, E. Širmulis, Laser induced photoresponse in perovskite solar cells. *International Conference, Laser Technologies*. (LTLA 2023)" June 29-30, 2023, Truskavets, Ukraine.

C5. Steponas Ašmontas, Jonas Gradauskas1, Asta Grigucevičienė ,Konstantinas Leinartas ,Andžej Lučun1, Muhammad Mujahid*,Kazimieras Petrauskas, Edmundas Širmulis, Algirdas Sužiedelis. Photovoltage formation in perovskite solar cell under laser excitation. *The international APROPOS 19 conference.* Sauletekio av. 3, Vilnius, Lithuania, 1-4 October 2024.

C6. Muhammad Mujahid*, Steponas Ašmontas. Investigation of Photovoltage Formation in Perovskite Solar Cells. *FizTeCh 2024*. Saulėtekio al. 3, Vilnius, 15-17 October, 2024.

C7. E. Širmulis, S. Ašmontas, A. Čerškus, J. Gradauskas, A. Grigucevičienė, R. Giraitis, K. Leinartas, A. Lučun, M. Mujahid*, K. Petrauskas, A. Selskis, A. Sužiedėlis, A. Šilėnas. Photoelectric behavior of perovskite solar cells excited with a nanosecond laser pulse. Truskavets, Ukraine, June 26-27, 2025.

1.7. Author's Contribution

The author's direct contributions are:

Enhancement and advancement of TiO_2 ETL fabrication techniques by spray pyrolysis and spin coating procedures.

Manufacturing perovskite absorbers ($MAPbI_3$) and Spiro-OMeTAD HTL within an inert glovebox.

Conducting precise optical measurements, including absorption, transmittance, and efficiency assessments.

Conducting comprehensive experimental data analysis and interpreting outcomes.

Developing and communicating research articles and showcasing significant findings at scientific conferences organized by FTMC.

2. LITERATURE REVIEW

2.1. General Background in Renewable Energy and PV

Recent technological advancements over the past decade have led to a rise in global energy consumption. A gradual societal shift toward the sustainable utilization of resources, including the production of clean and sustainable energy, follows this[9, 10]. An ongoing discussion among scientists and policymakers centers on prioritizing economic and social growth, which includes reducing carbon dioxide (CO_2) emissions[11]. The rising global energy demand has led to heightened environmental pollution, contributing to global warming and an energy crisis. A significant study has examined the origins of CO_2 emissions and explored techniques for their reduction, aiming to mitigate their impact on global warming. Nonrenewable energy consumption is identified as a significant contributor to CO_2 emissions, with fossil fuels accounting for over 80% of global energy usage[12]. Renewable, sustainable energy sources are being widely adopted by developing countries to address the growing concern over carbon emissions and the steadily decreasing reserves of fossil fuels. As an indicator of the ongoing shift in global energy production, development, and consumption patterns, emerging renewable technology in developing countries is rapidly expanding and finding widespread use. Since the onset of the 21st century, energy systems based on renewable sources, including wind, PV, biomass, and nuclear, have proliferated through both small- and large-scale implementations[13]. The capacity to be renewed, replicated, or reclaimed makes anything renewable. Renewable energy is power that can be used repeatedly without depleting natural resources. Renewable sources will be revitalized shortly. The produced energy may be utilized immediately or stored in batteries. Renewable energy is generated by harnessing diverse forms of energy from various sources. Renewable energy sources capable of fulfilling residential energy needs provide the ability to deliver energy services with little or virtually no emissions of air pollutants and greenhouse gases[14]. Developing renewable energy systems will enable the resolution of critical issues, such as enhancing energy supply dependability and optimizing organic fuel efficiency. Decentralized harvesting of renewable energy is a viable solution for meeting the energy needs of rural and small-scale communities in a dependable, cost-effective, and environmentally friendly manner. To ensure a sustainable future, replacing non-renewable

energy sources with renewable ones is essential. Wind, sun, biomass, hydropower, and other renewable energy sources are examples of assets that have the potential to provide electricity repeatedly[15]. There will be less need for people to leave rural areas for cities if renewable energy projects are developed and implemented in these areas.

Solar energy is the most widely utilized renewable energy source globally; however, its effectiveness is limited by the amount of solar radiation received and the efficiency of solar energy capture systems[16]. Solar technology has been deployed in various forms, such as photobiological applications, solar power generation, photochemical reactions, and solar thermal energy. Solar energy is a compelling resource for the future, with PV technology being the most widely adopted. The considerable advancements in research within this domain have led to a quick decline in costs, which substantially facilitates its spread and has impacted governmental energy policies.

PVs involve the direct conversion of sunlight into electricity using thin layers of semiconductors, which possess characteristics intermediate between those of metals and insulators. Solar cells are based on the groundbreaking research of numerous Nobel laureates from the 20th century, a pivotal period in the history of science[17]. Around the turn of the century, German scientist Max Planck was intensely preoccupied with the mystery of how the sun and other hot things produce their light[18]. That energy could only exist in discrete levels was an assumption he had to make to harmonize theory with experiment. The idea that light consists of microscopic "particles" (later called photons) whose energies vary according to their colors was first proposed by Albert Einstein in his "miraculous year" (1905)[19]. The development of quantum mechanics, which reached its peak with Edwin Schrödinger's wave equation in 1926, was prompted by Einstein's revolutionary hypothesis[20]. For solid materials, Wilson found the solution to this equation in 1930. Because of this, he clarified the characteristics of semiconductors, which have intermediate electrical properties, and the difference between insulators and metals, which are excellent electrical conductors[21]. The semiconductor material must absorb a significant portion of the sunlight spectrum. The absorption characteristics of the material determine the region near the surface that is most effective in absorbing light. An electric field must be applied at the junction to separate the electrons and holes created by absorbed light quanta to avoid their recombination. The French physicist Alexandre Edmond Becquerel is widely acknowledged as the one who first observed what is now often referred to as

the "PV effect" or the "Becquerel effect." Almost all solar cells operate on this principle[22]. Coupled to platinum electrodes, Becquerel demonstrated that illuminating silver chloride in an acidic solution would produce a voltage and current. Not long after Becquerel's electrochemical cell, similar proofs were forthcoming, the most striking of which involved the employment of selenium (Se) in conjunction with platinum (Pt) or gold (Au) to form a solid-state device[23]. The first solid-state solar cell, the Schottky solar cell, was created by American inventor Charles Fritts using a thin coating of Au on Se. These cells convert approximately 1% of solar energy into useful electricity[24].

2.2. FUNDAMENTAL PRINCIPLES OF PV TECHNOLOGIES

People used to admire the sun because they believed it was the source of life. Understanding the sun as an energy source developed later, with the advancement of education and the Industrial Revolution. The discovery's significance reached its peak in the modern era when it became clear that using fossil fuels for electricity could alter the Earth's average temperature[25]. Solar radiation, which can be converted into energy in various ways, is the primary source of all renewable energy on Earth. Due to its broad spectrum of wavelengths, which spans from short-wave infrared to ultraviolet (UV), this radiation is perceived as white light[26]. Power generation relies heavily on this kind of radiation. A significant aspect of this radiation is the PV effect, which directly converts it into electricity. Direct conversion of solar radiation into electricity, free of the need for a heat engine, is known as PV conversion. The fundamental benefit of PV devices is that they can provide outputs ranging from microwatts to megawatts; they are also simple in design, robust, and require little maintenance[27]. Their versatility makes them ideal for a wide range of applications, including, but not limited to, power generation, water pumping, remote buildings, solar home systems, communications, space vehicles and satellites, reverse osmosis facilities, and megawatt-scale power plants. The demand for PVs continues to rise annually due to their wide range of applications. A fully developed PV industry is expected to emerge in the next century. Intense research is driving current trends in the PV sector, which means that PV cells are becoming more affordable and efficient at converting sunlight into electricity. This is making solar power a more attractive option for consumers. No matter where you live in a rapidly developing megacity or a little town, PV solar cells will be on your roof or your neighbor's[28]. This means that practically everyone will have heard about PVs.

The process of converting light into electricity begins with a semiconductor absorbing light. To be absorbed by the substance, photons must have the correct energy[29]. Semiconductor materials are used in PV cells to transform light into power. A band of prohibited energy known as the band gap separates the valence and conduction bands in these materials; the width of this band varies with the chemical composition and structure of the substance. Crystalline silicon has a band gap of 1.1 eV, hydrogenated amorphous silicon of 1.7 to 1.9 eV, and gallium arsenide of 1.5 eV[30]. Differentiating between direct and indirect gap materials can be done by examining the location of the valence band maximum (VBM) and conduction band minimum within the Brillouin zone. Electrons in a semiconductor material are in a valence band and strongly bonded in covalent bonds with nearby atoms when the material is at equilibrium. A photon's energy is transferred to an excited electron, which moves from the valence band to the conduction band and creates a hole (a positive charge) in the valence band as a result of absorption. That is why the semiconductor can produce electron-hole pairs that can move about as they absorb light. Excited electrons and holes can recombine spontaneously, dissipating the photon's energy, as stated in the principle of detailed balance. Some electrons and holes recombine to form excitons, which are localized pairs of electrons and holes with an excited energy state when they are physically close. After that, a portion of these excitons relax by a photoemissive process and radiatively decay to the ground state through spontaneous emission. The process is utilized in organic light-emitting diodes (LEDs) to generate light. Examining the solar spectrum, which provides the number of photons for each wavelength, is also critical. Semiconductor materials are used in PV cells to transform light into power. A band of prohibited energy known as the band gap separates the valence and conduction bands in these materials; the width of this band varies with the chemical composition and structure of the substance. The Sun's intrinsic fusion process produces radiation with a power of 3.8×10^{20} W, making it comparable to a nuclear reactor[31, 32]. Surface temperatures are only 5,800 K, whereas temperatures in the Sun's core are ten million degrees[33]. At this temperature, the extraterrestrial sunlight's spectrum is similar to that of a black-body radiator. The intensity and structure of the solar spectrum on Earth vary because the atmosphere absorbs light of different wavelengths at varying rates. Direct radiation from the Sun and a diffuse component caused by atmospheric radiation scattering[34]. When planning concentrated solar PV systems, it is crucial to consider the ratio of diffuse to direct radiation.

The local solar spectrum and absorption are both affected by the distance that the sun's radiation must travel through the atmosphere. The amount of radiation that can be converted into energy heavily depends on the absorption characteristics of the PV materials used[35]. The two most important mechanisms that govern light absorption in semiconductors are transitions within bands and the excitation of electrons from the valence band to the conduction band by photons. If the absorption is phonon-assisted, a photon with a minimum energy ΔE that is either equal to or slightly lower than the semiconductor's forbidden band gap Eg is used in the first process, known as basic absorption[36, 37]. To transform radiation into free electrons and holes, which are the semiconductor's electrical carriers, this transition is crucial to the PV process [38]. Only one electron-hole pair is created when a photon's energy exceeds E_G; the extra energy is diffused as thermal energy and wasted during PV conversion. Free carrier absorption is the second process; it raises the energy of free carriers but is useless for energy conversion. According to Sclar, extrinsic absorption occurs in an extrinsic semiconductor between the energy bands and the energy level associated with the impurity[39]. This absorption is irrelevant primarily in PV conversion, although it serves infrared detectors well. There has been enormous development in PV technology since its inception, with initial advancements focusing on reducing costs and increasing efficiency. PV technology is noteworthy not just for the clean energy it can provide, but also for the way it could revolutionize the energy sector by delivering a distributed, reliable, and long-term power supply. This is the primary reason for the significance of PV technology [40]. The success of solar energy as a viable alternative to conventional fossil fuels has been significantly influenced by the rapid advancements in device designs and materials.

One essential feature of solar cells is their efficiency. The efficiency of a PV cell is defined as the ratio of its electrical output to the energy it receives from the sun. A cell's efficiency in converting energy into usable form is determined by dividing its power output at its maximum power point (P_m) by the product of its surface area (A_c) and the incoming light (E_I, in W/m^2).

$$\eta = \frac{P_m}{P_{incident}} = \frac{P_m}{E_I * A_c} \qquad (1)$$

A PV cell can function within a range of currents (I) and voltages (V). The maximum power point (P_m) of an irradiated cell can be determined by continuously increasing the resistive load on the cell from zero (a short circuit) to a very high value (an open circuit)[41]. This is the load for which the cell can deliver the maximum electrical power at the specified level of

irradiation, and it is the point at which V × I is maximized. The maximum power generated by the cell under illumination is equivalent to the product of I_{sc} (short circuit current) and V_{oc} (open circuit voltage) in the ideal case, where the I-V characteristic is rectangular. The Boltzmann equation, which gives the I-V characteristic its exponential shape in practice, restricts the maximum power to the product $I_{max} \times V_{max}$ (**Figure 1**). The fill factor (FF), which is calculated by dividing the available power at the maximum power point (P_m) by the ideal maximum power ($V_{oc} \times I_{sc}$), is another term that defines the overall behavior of a solar cell [42, 43].

$$FF = \frac{V_{max} * I_{max}}{V_{oc} * I_{sc}} \quad (2)$$

$$\eta = \frac{P_{max}}{I_{incident}} = \frac{V_{max} * I_{max}}{E_I * A_c} \quad (3)$$

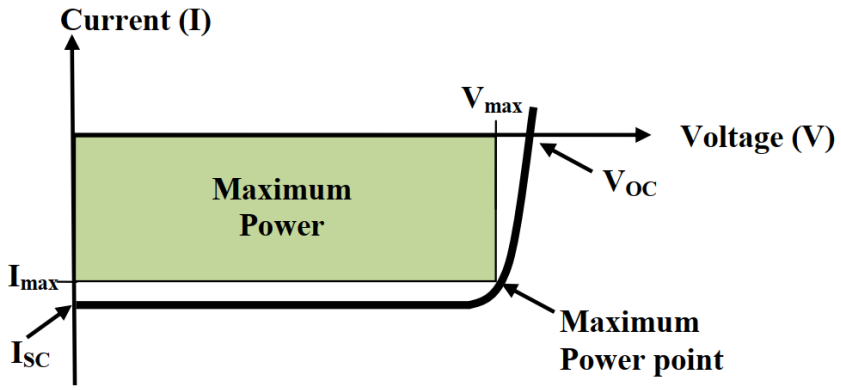

Figure 1. I-V characteristics of a p-n junction PV cell.

From a historical perspective, Bell Laboratories achieved a significant milestone in 1954 by manufacturing the first Si-based solar cell [44]. Despite their inefficiency, these precursor cells established the foundation for subsequent developments. An innovative selenium cell, as demonstrated by the research of Charles E. Fritts, exhibits light-dependent resistance that varies from approximately 500 ohms to 9 ohms [24]. A study that mentioned a roughly 6% efficiency was a significant milestone in improving the efficiency of PV cells [45]. Through subsequent efforts by Hoffman Electronics, the improvement was around 10% to 15% by 1961[46]. According to the study, a pair of electrons and holes can be created by light with a wavelength of less than 1.2 μm [45]. However, the maximum theoretical efficiency of single-junction solar cells diminishes as the

wavelength of the light decreases, limiting their use. A monolithic stack with a six-junction inverted metamorphic structure was utilized in a recent study to achieve a solar conversion efficiency of 47.1% [47]. In the following decades, efficiency and cost reduction experienced consistent progress, driven by the development of new technologies and the increasing energy demand. Thin-film solar cells were among the numerous varieties of PV cells that experienced a surge in popularity during this period, and the utilization of PV technology expanded beyond its initial application in space exploration [48].

Wafer-based Si and various thin-film technologies are among the technologies that comprise the current PV market. The variety of existing and potential future alternatives has been categorized from first-generation to third-generation technologies. The various materials used for PV solar cell systems are shown in **Figure 2**. These materials primarily consist of Si, cadmium-telluride, copper-indium-gallium-selenide, and copper-gallium-sulfide.

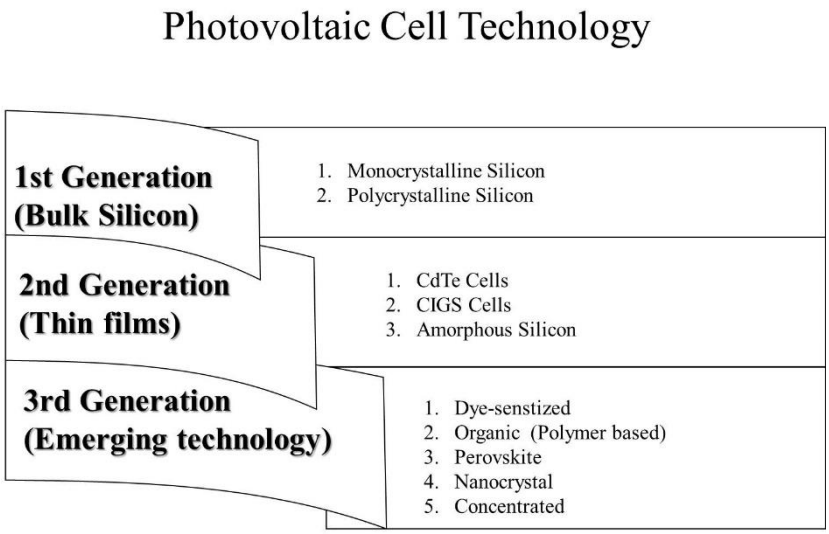

Figure 2. PV generation

Si is the primary component of first-generation solar cells, also known as conventional or classic solar cells [49]. Although the efficiency of these cells varies between 6 and 15%, it has increased considerably over time due to ongoing research and development [50]. Single-crystalline, also called monocrystalline Si (mc-Si), and multiple-crystalline, often called polycrystalline (poly-Si), are the two main types of first-generation solar

cells. The high cost of raw materials and low efficiency are two primary drawbacks of first-generation solar cells. When exposed to high temperatures, their efficiency decreases drastically, resulting in a corresponding decrease in power output.

Materials such as amorphous Silicon (a-Si), copper indium gallium selenide (CIGS), and cadmium telluride (CdTe) are used to make second-generation solar cells, also known as thin-film solar cells [51]. A key concern with first-generation cells was their high cost, so second-generation PV solar cells primarily aim to lower it. To achieve this, thin-film methods are employed, which involve reducing the amount of material used while simultaneously enhancing its quality and performance. They may tolerate higher temperature fluctuations and are thinner than conventional solar cells. These cells are well-suited for use in lightweight, portable solar panels for outdoor applications and building-integrated PVs (BIPV) [52]. Ongoing research and development aims to enhance efficiency, lifespan, and cost-effectiveness, making them more competitive with standard solar cells. Their adaptability and affordability are contributing to their rising popularity [53].

Technologies that use PVs based on more recent chemical compounds are considered third-generation. Third-generation solar cells may drastically reduce the cost of solar power. A further benefit of third-generation solar cells is their increased efficiency compared to earlier generations. This means that the same quantity of sunlight can now produce more electricity [54, 55]. From organic and dye-sensitized solar cells, which are inexpensive and have low efficiency, to III-V multi-junction cells, which are expensive and have high efficiency, the third generation of solar cells encompasses a wide range of approaches, from tandem and perovskite to organic and emerging concepts. These cells have a variety of uses, from building integration to space applications [56].

2.2.1. Physics of Solar Cells and PV Effect

The use of UV light to enhance the sensitivity of sparking was discovered in 1887 by the German physicist Heinrich Hertz [57]. The enhanced sensitivity was later ascribed to light-pushing electrons by J.J. Thompson, who had previously identified the electron in 1897 [58]. The result mentioned above, however, was at odds with the conventional view of electromagnetic radiation, which held that light acted like transverse waves. The idea that light consists of individual photons or energy quanta was

ambiguous until Albert Einstein made it explicit [59]. As stated in Planck's formula, the energy of a photon is directly proportional to its frequency [60].

$$E = \hbar\nu = \frac{\hbar c}{\lambda} \qquad (4)$$

$\hbar$ for Planck's constant, which has a value of 1.055×10^{-34} J.s., v for electromagnetic radiation's frequency, and c for the speed of light, which is 3×10^{8} m/s. Light, or electromagnetic radiation, can only be emitted or absorbed in discrete elements, but it propagates according to linear wave equations. Therefore, it has the dual properties of a wave and a particle. Thus, when light hits a metal, the photons either collide with the atoms or knock the electrons out of the metal atom if the photon's frequency is high enough. Here, we have the photoelectric effect. One of the most effective methods for utilizing solar energy is PV technology. A PV cell is an electrical device composed of specific semiconductor materials, such as Si, that exhibit a particular property known as the bulk PV effect. In the PV effect, light is absorbed and released as electrons; an electric current is generated by collecting these free electrons. One of the most essential parameters in turning solar energy into electricity is the efficiency of solar cells, which is dependent on temperature. The rate of electron-hole recombination inside the solar cell increases with temperature. The Arrhenius equation governs this temperature-induced acceleration, which results in reduced efficiency. Due to changes in their dynamics, charge carriers are less effective in generating electrical currents at high temperatures. To maximize the performance of solar cells, a detailed investigation into the correlation between temperature and efficiency is required. The bandgap characteristics of the materials used in solar cells are affected by changes in temperature [61]. The energy difference between the conduction band minimum and valence band maximum, or bandgap, is an essential parameter in photon absorption. The range of photons that semiconductors may absorb can be affected by temperature changes in their bandgap. Although they may be more prone to thermal losses, materials with narrower bandgaps have the potential to absorb photons with lower energies [62, 63].

A PV cell's "fuel source" is incident photons from the sun. These photons cover the visible, UV, and infrared spectrums. Not every photon that hits the cell can enter it. Some bounce off the cell's front surface, while other layers of the front surface parasitically absorb others. As a result, not every photon that reaches the semiconductor can produce an electron-hole pair. Absorption of photons with energies below the bandgap results in either no absorption or the conversion of the photons into heat (for example, free

carrier absorption). Some may pass through the device and into the cell, while others may be absorbed by layers on the cell's back (like metal contacts). Photons can escape the front even if internally reflected at the back surface. Although increasing the thickness of the Si substrate would help reduce some of the losses on the cell's back side, doing so would be prohibitively expensive. It would also limit the usage of very thick wafers due to bulk carrier recombination. As the incident light's wavelength approaches the band-gap energy, Si's absorption coefficient decreases rapidly because it is an indirect band-gap material. 1.12 eV is the correct wavelength. Therefore, the thickness required to absorb all the light is directly proportional to the wavelength of the light. Essential to this situation are the photon management structures.

2.2.2. Solar Spectrum

The ultraviolet to infrared spectrum encompasses a wide range of electromagnetic radiation that the sun emits. Light rays of different wavelengths make up the spectrum, determining its form and intensity. Solar radiation, also known as solar irradiance, is a term used to describe it. Spectral irradiance, measured in Wm^{-2} nm^{-1}, is the amount of energy that falls on a horizontal unit area at a given time and wavelength. The distribution of irradiance across different wavelengths is presented in the solar spectrum [64]. Several factors, including the Earth-Sun distance, the angle at which the sun's rays reach the Earth's atmosphere, weather conditions, and the level of air pollution, influence the intensity of the solar spectrum received by Earth. The air mass (AM) is a constant component that defines the atmospheric parameter, typically significantly affecting the solar spectrum. The shortest path that sunlight takes through Earth's atmosphere before reaching the surface determines this. The photovoltaic technology that turns sunlight into electricity relies on solar cells, which are extremely sensitive to the wavelength and intensity of the sun's rays [65]. The UV, visible, and infrared parts of the sun's spectrum are the most fundamental divisions. See **Figure. 3** for a comparison of the spectrum responsivities of some prominent technologies [64, 66]. Behind it is the plot of the AM1.5 reference spectrum.

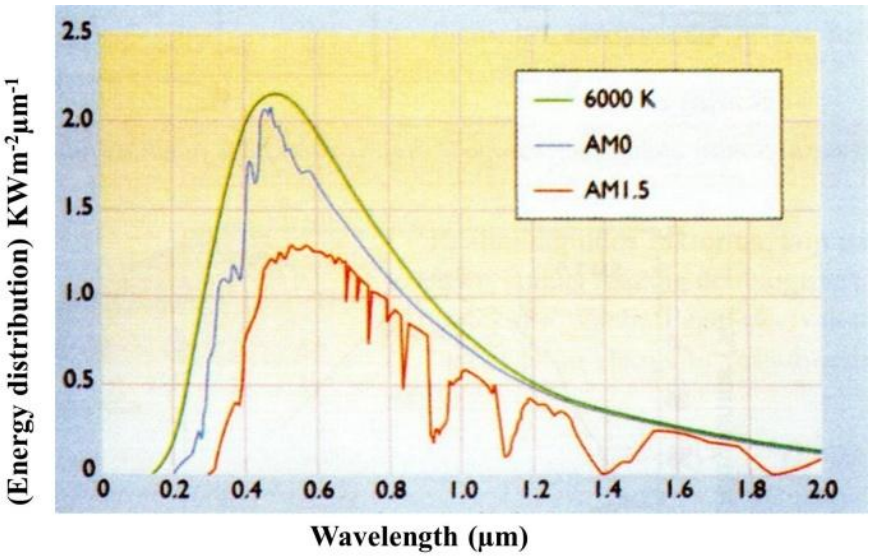

Figure 3. Comparison of the solar spectrum above the atmosphere-AM0 and the standardized AM1.5 incident on the earth's surface with the spectrum of blackbody radiation at 6000K.

The path that direct radiation travels through the air is characterized by the concept of air mass. The calculation of this path length involves determining the ratio of the direct optical path length to the path length measured at the zenith, which is oriented vertically upwards. With an increase in the direct optical path length, there is a notable increase in the scattering of shorter wavelength light, which has a higher frequency. This phenomenon results in a larger proportion of longer-wavelength light being observed by the observer. Consequently, variations in air mass exhibit a significant relationship with changes in the solar spectrum [67, 68]. The observed spectral shift linked to variations in air mass has prompted studies into the correlation between air mass changes and PV performance. Passow et al. observe that changes in air mass ranging from 1.0 to 5.0 lead to performance variations of up to 5% in cSi modules and topping 5% in CdTe modules [69]. The reference solar spectra for solar energy applications illustrate the terrestrial solar spectral irradiance that strikes a particular surface under defined atmospheric conditions. The measurements refer to the direct normal spectral irradiance and the global spectral irradiance on a sun-facing surface tilted at 37°, commonly designated as AM1.5D and AM1.5G, respectively, due to their alignment with the AM1.5 conditions [70].

2.2.3. Properties of Semiconductors

Solar cells are composed of semiconductors. Those that conduct electricity, such as metals, are classified as conductors, whereas those that obstruct electricity are termed insulators. Semiconductors possess properties that are midway between those of metals and insulators. By leveraging these qualities, semiconductors convert light into electricity, produce light from electricity, enhance electrical signals, and facilitate switching actions. Si is a primary semiconductor that powers computers and converts light into electricity. The atomic structure of Si resembles that of diamond, with interatomic lengths being greater than those of carbon in diamond. Ge was also utilized for first-stage transistors, with a structure analogous to Si, differing only in the lattice constant. The Fermi level is positioned equidistantly between the valence and conduction bands in intrinsic semiconductors, such as silicon (Si) and germanium (Ge). Conduction does not exist at absolute zero, as conductivity is a temperature-dependent phenomenon. At elevated temperatures, limited quantities of electrons can transition to the conduction band, thereby generating a measurable current. Extrinsic semiconductors incorporate additional energy levels.

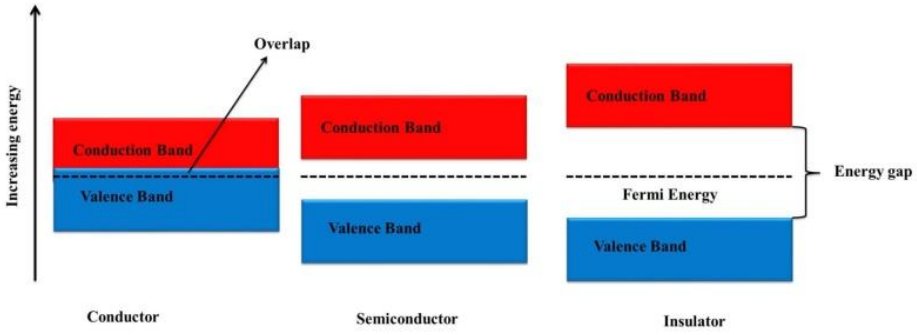

Figure 4. Comparison of the band gaps

The temperature-dependent increase in conductivity can be approximated using the Fermi function, which facilitates the determination of the conduction band occupancy. The energy level is shown in **Figure 4.** The Fermi Function provides the probability that a specific electron energy level will be occupied at a designated temperature [71]. The Fermi function is expressed as

$$f(E) = \frac{1}{e^{\frac{E-E_f}{kT}}+1} \qquad (5)$$

The function demonstrates that at typical temperatures, most energy levels up to the Fermi level E_F are occupied, with only a limited number of electrons possessing energies exceeding the Fermi level.

Due to its semiconductor characteristics and technological advantages, Si has emerged as a predominant semiconductor material. Energy gaps (bandgaps, *Eg*) are crucial in semiconductor applications. Figures **5a** and **5b** illustrate that electrons are present in the conduction and valence bands. Conversely, the region devoid of energy levels for electrons is referred to as the energy gap (bandgap), a critical parameter that significantly influences the motion of semiconductors.

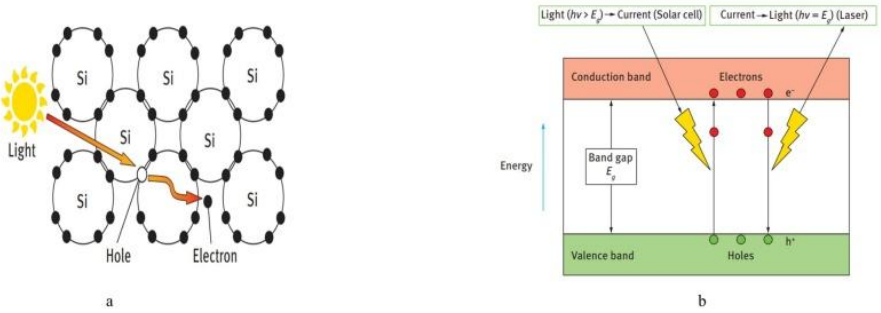

Figure 5. a) Generation of electron and hole by the light excitation of Si. B) The emission and absorption of light.

Irradiating semiconductors with light higher than the bandgap energy (*Eg*) causes the valence band electrons to be stimulated to the conduction band. Electric current flows due to the creation of holes by the excitation of electrons. A photon's energy is proportional to its wavelength in the following way:

$$E_g(eV) = \frac{1240}{\lambda(nm)} \qquad (6)$$

2.2.4. The p-n Junction

A semiconductor diode is a building block of a solar cell, specifically engineered to convert sunlight into usable electricity. An n-type diode is a semiconductor made from a single crystal of a material, such as silicon, with pentavalent impurities. A p-type diode is made of a semiconductor material with trivalent impurities. In each area, the doping process produces more mobile carriers, which are referred to as majority carriers. An area of positively charged donor atoms near the n-zone is created when semiconductors from the n- and p-regions come into contact because

electrons from the n-section diffuse into the p-section. Also, when holes go from the p-region to the n-region, they leave behind a network of acceptor atoms with negative charges in the p-n junction, close to the p-zone. Light with energy E_g is released when electrons from the conduction band fall into the valence band to mix with holes. When semiconductors are doped, they can form interfacial structures known as pn junctions, which enable efficient emission or excitation.

Semiconductors have numerous applications and can be utilized in various devices, such as solar cells and laser diodes. Electrons and holes are created when light hits solar cells. Next, the current is generated by transferring these electrons to n-type Si and p-type Si, respectively. It is crucial for solar cells that the Fermi level and the band slope, which are determined by the internal electric field, coincide. The internal electric field slants the energy band, and although n-type and p-type Si have distinct Fermi levels, they coincide at the pn-junction interface. Next, the voltage causes electrons and holes to migrate in opposite directions, resulting in the flow of current. Particularly crucial to solar cells and other devices is the pn-junction, which is created between the absorber and the electron membrane. This is the region closest to which most electrons and holes are produced. Under illumination, no current flows through solar cells whose terminals are in an open circuit. The resulting voltage is the open-circuit (V_{OC}) and is an electromotive force. While no voltage is applied, the current density in a short circuit is known as J_{SC}.

2.3. Solar Cells

There are various types of solar cells, each with its unique benefits and applications. Considerations, including efficiency, cost, and application, dictate the type of solar cells used. The main uses and varieties of solar cells are listed in Table 1.

Table 1: Types of solar cells and their applications

Type of solar cell	Application
Monocrystalline	Residential and commercial
Polycrystalline	Utility-scale installations
Thin-film	Building-integrated PV
Multi-junction	Concentrated solar power
Bifacial	Dual-sided solar panels

There are various types of solar cells, each with its advantages and disadvantages. Despite their high production cost, monocrystalline Si solar cells made from single-crystal Si wafers are widely used in commercial and residential installations due to their high efficiency [72]. Built from many Si crystals, polycrystalline Si cells are an affordable substitute for monocrystalline cells, albeit with a slightly lower efficiency. They are used in various contexts, including residential and commercial buildings [73]. The PV market is dominated by crystalline Si cells, which are directly correlated with the efficiency of solar systems. Additionally, despite their lower cost, amorphous Si solar cells are less efficient than other Si cells. A variety of consumer products are powered by Si solar cells, which are composed of amorphous thin films. With the advancement of the solar industry, larger amorphous Si solar modules are also becoming accessible. Large-scale utility solar farms often utilize CdTe solar cells due to their competitive efficiency and low manufacturing costs. BIPV is one of the many applications for CIGS cells that strike a balance between price and efficiency [74, 75]. There are numerous thin-film technologies, including amorphous Si. A film of this solar cell can be affixed to low-cost substrates, such as glass or plastic. Cadmium telluride/cadmium sulfide cells, gallium arsenide cells, copper indium diselenide/cadmium sulfide cells, and thin multi-crystalline Silicon are additional thin-film technologies. There are numerous benefits to thin film cells, including their high suitability for large-scale applications, their ability to be deposited on inexpensive substrates or building materials, and their ease of mass production. Additionally, they are more straightforward to deposit and assemble [76]. Designed for specific applications where high efficiency is crucial, multi-junction solar cells comprise several layers of different semiconductor materials. These cells, which are widely used in high-efficiency terrestrial installations, concentrator PVs, and space applications, are designed to capture a specific spectrum of sunlight [77]. The lightweight and flexible nature of organic solar cells, which use organic materials as the active layer, is well recognized. Primarily used in portable and specialized applications, they can be produced at a low cost [78].

2.3.1. History and Evolution of Perovskite Materials

In 1839, physicist Gustav Rose used "Perovskite" to describe $CaTiO_3$ [79]. He did this in honor of the Russian scientist Perovski. Scientist Goldschmidt subsequently applied it to crystalline groups with structures in 1926. Perovskites are most commonly found in nature as di-cation oxides.

However, they can also be found in various formulations with silicate components, including hydroxides, fluorides, arsenides, chlorides, and intermetallic compounds [80]. Magnetism, ferroelectricity, and two-dimensional electronic conductivity are some essential physical characteristics exhibited by perovskites, an oxide class with the chemical formula ABO_3 [81]. In today's optoelectronic world, "perovskite" typically refers to metal halide perovskites, which have the formula ABX_3. In this formula, A represents monovalent cations such as $CH_3NH_3^+$ (MA^+), $CH(NH_2)_2^+$ (FA^+), and Cs^+, B represents divalent metal cations like Pb_2^+ and Sn_2^+, and X stands for halide ions like I^-, Br^-, and Cl^-. The bigger A^+ cation in this structure works in tandem with twelve X^- anions to fill a cuboctahedral void, and the smaller B_2^+ cation works in tandem with six X^- anions to fill an octahedral vacuum. Materials science, chemistry, and physics have recently shown great interest in halide perovskites. Before M. Era et al. investigated the electrical characteristics of 2D layered halide perovskites and their application to electroluminescent devices[82], Wells' 1892 synthesis of lead halide perovskites received little attention [83]. The semiconducting channels of field-effect transistors were made of organic-inorganic hybrid perovskite (OIHP) by Kagan et al. in 1999 [84]. The efficiency of dye-sensitized solar cells (DSSCs) was 3.8% in 2009 and 2.6% in 2006 when Miyasaka et al. utilized organometallic perovskites $CH_3NH_3PbI_3$ and $CH_3NH_3PbBr_3$, respectively [3, 85]. A cell architecture comparable to the extremely thin absorber (ETA) DSSC was developed by Park et al. in 2011, employing $CH_3NH_3PbI_3$ nanoparticles and TiO_2 surface treatments; they attained an efficiency of 6.5% [86] .Park and Gratzel et al. (2012) integrated perovskites into a TiO_2 scaffold and substituted the liquid-based HTL with solid-state spiro-MeOTAD because of corrosion issues with liquid electrolytes, improving efficiency to 9.7 % [87].

Halide perovskite semiconductors are well-suited for use in solar cells due to their numerous desirable properties, such as high carrier mobility (~25 $cm^2V^{-1}S^{-1}$) [88], low charge recombination rate on a microsecond time scale, intense absorption in the visible region [89], and a long carrier diffusion length of up to approximately 1 μm [90]. Their weak exciton binding energy is around 45 meV [91]. In addition, advancements have been made in designing interface engineering [89], growing perovskites efficiently [90], improving materials for hole transport [91], and modifying their properties through chemical composition modifications [92]. In contrast to polycrystalline perovskites, which have a defect density of around 10^{16} cm^{-3}, single-crystalline $MAPbI_3$ has a density of around 10^{10} cm^{-3} [93]. With

a diffusion length of around 175 μm, the carrier lifetime for single-crystalline $CH_3NH_3PbI_3$ perovskites can reach several hundred microseconds. The $CH_3NH_3PbI_3$ perovskite material also has the unusual ability to transport holes due to its ambipolar transport feature [94, 95]. Extensive theoretical investigations have supplemented experimental studies to understand better the electrical properties, potential, and constraints of perovskite materials for use in various devices. Before the experimental report of the first PSC, first-principles simulations were used to study the electronic structures of halide perovskites. One computer modeling approach to studying the electrical structure of many-body systems is first-principles calculation based on density functional theory (DFT). This theory states that density functionals, among which the exchange-correlation functional is the sole one that is not well-defined, can be used to identify the parameters of a many-electron system. The findings may vary depending on the approximation used for the exchange-correlation functionals.

2.3.2. Structure and Bandgap Engineering in Perovskites

The crystal structure of the hybrid halide perovskite compounds is identical to that of calcium titanate ($CaTiO_3$). Their typical formula is ABX_3. An organic cation denoted as A = [methylammonium, formamidinium], a divalent metal, denoted as B = (Pb_2^+; Sn_2^+), and a halide X = (Cl^-; Br^-; I^-) form the usual components of halide perovskites with the ABX_3 structure [96]. Two elements must be considered to predict the stability and morphological characteristics of a perovskite: the octahedral factor μ and the Goldschmidt tolerance factor. The ideal value of the tolerance factor t is 1, which allows for preserving a cubic structure with good symmetry [97, 98]. The expression for the tolerance factor t as a function of the ionic radii of the ions at the A, B, and X sites is

$$t = \frac{(R_A + R_X)}{\sqrt{2}(R_A + R_X)} \quad (7)$$

$$\mu = \frac{R_A}{R_X} \quad (8)$$

At a tolerance factor of about 0.9, the perovskite crystal structure is stable, and at *t=1*, a perfect cubic lattice is created. When *t* is less than 0.8 or larger than 1, the perovskite lattice can transform into a non-perovskite structure, an orthorhombic or tetragonal crystal lattice, or a deformed version of its usual shape. For instance, hexagonal or ilmenite-type $FeTiO_3$ structures are generated. Conversely, the octahedral factor determines the stability of the [BX_6] cuboctahedron. As demonstrated by empirical investigations, a stable perovskite structure is achieved when the value is 0.414 or higher

[99]. On the other hand, a non-perovskite or distorted morphology that affects the perovskite structure can occur if the A cation's size is slightly off, since this causes the tolerance factor to become aberrant and the [BX_6] cuboctahedron to tilt to adjust. Additionally, it has been established that the PCE of PSC is directly correlated with the perovskite crystal orientation, as determined in previous studies. It has been demonstrated that CH_3NH_3 aids in the structural cohesiveness of $MAPbI_3$ perovskites but does not contribute to their optical or electrical response [100]. Because the valence and conduction bands are produced by combining the metal and halide orbitals, the metal-halide relationship primarily affects the optoelectronic properties of ABX_3 perovskite. Band edge energy levels are not directly affected by the A-site cation. However, lattice contraction and octahedral tilting can indirectly affect band locations [89, 101]. A higher short circuit current density and PCE are achieved when the perovskite layer's crystal orientation is correct at the interface with appropriate charge transport layers.

Due to its exceptional electronic characteristics, there has been much anticipation of hybrid organic-inorganic metal halide perovskites as a potential material for use in solar devices. Visual representations in **Figure 6** show that colloidal halide perovskites of various compositions produce distinct color indices when exposed to UV light [102]. Depending on the halide composition, which can range from $CsPbBr_3$ to $CsPbCl_3$, the photoluminescence (PL) peaks of the $CsPbX_3$ perovskite colloidal solution appear in the 700-405 nm (1.77-3.06 eV) range (**Figure 6**) [103]. In this way, achieving intermediate band gaps by combining several halides is possible. For example, the band gap from 2.4 eV in $CsPbBr_3$ (with half of the Br atoms replaced with Cl atoms) increases to about 2.7 eV. This suggests that altering their compositions can efficiently modify the optoelectronic properties of halide perovskites.

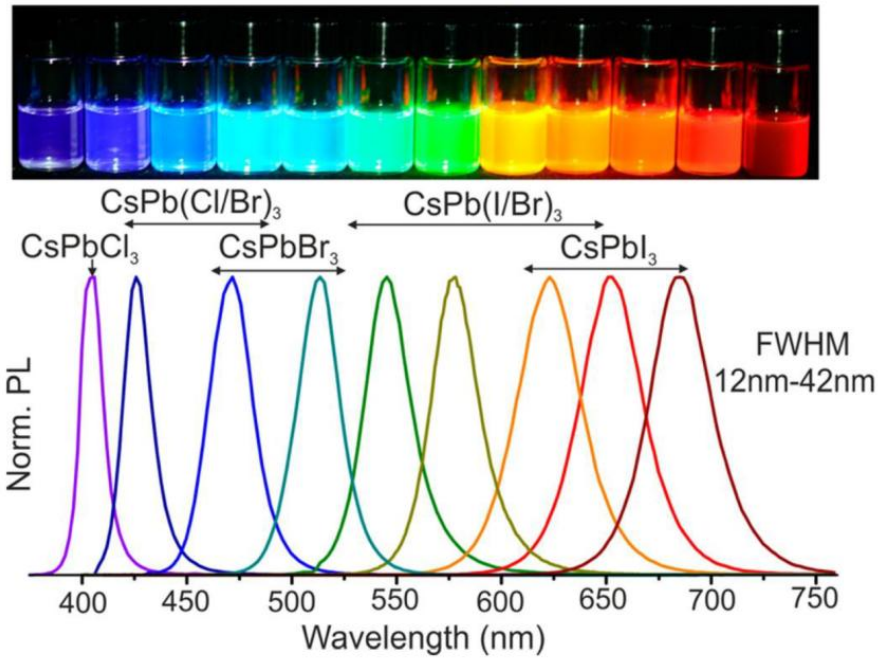

Figure 6. In the upper right corner of the figure, colloidal solutions in toluene shine under a UV lamp with a wavelength of 365 nm. The bandgap energies of these colloidal perovskites, where X can be Cl, Br, or I, can be adjusted by changing their size and composition [102].

The unique electronic characteristics of hybrid perovskites are primarily explained by the fact that the Pb cation has an occupied 6s orbital located below the top of the valence bands, as opposed to the vacant outer s orbitals of other cations [104]. Halide perovskites exhibit remarkable electronic structures, featuring both ionic and covalent characteristics. The VBM strongly binds with Pb s and I p, whereas the Pb p state mainly causes the conduction band minimum (CBM). The valence band and conduction band of the hybrid perovskite structure of $MAPbI_3$ are formed by the iodine ions at the X-site and the lead anion. At the B-site, respectively. The organic cation at the A-site contributes to the structural stability and tolerance factor of the perovskite structure. The relationship between the energy levels of halide perovskites and the cations at their A-sites has also been researched. The energy states associated with the atomic orbitals of A-site cations do not directly impact the VBM and CBM, unlike those of B and X elements. The explanation instead lies in the fact that halide perovskites have substantially shallower Fermi levels compared to the energy levels of A-site molecules [105]. Nevertheless, the experimental findings showed that the energy levels

can be adjusted by changing the cations at the A-site. The alterations in the B−X bond length and tilt of the BX_6 octahedral structure, which are influenced by the sizes and forms of A-site cations, have been the primary areas of theoretical investigation aimed at understanding these phenomena [106].

An element's band gap is its energy dispersion, measured from its VBM to its minimum conduction band. Band-gap modification is crucial in perovskite materials, as it directly impacts their optoelectronic properties. This characteristic defines the spectrum of electromagnetic radiation that a material may absorb and transform into an electrical signal. Perovskites' versatility in adjusting the band gap from a low to a high range has made them a desirable material for various applications, including solar cells, LEDs, photodetectors, high-energy fields, and particle detection systems. Due to their adjustable band-gap alignment with solar energy, metal halide perovskites are an encouraging family of materials for highly efficient PSCs. Compositional engineering, methods for reducing and mixing dimensions, and pressure-induced band gap modulation have all been covered in this area [107]. Every site on a perovskite lattice can undergo a chemical substitution, and there are good instances of this in the literature. Identifying the chemical difference between the three methods is critical. The band gap deformation potential describes the physical reaction to a hydrostatic volume change in the limit of a minor perturbation [108, 109]. The deformation potential α_V, as given in equation, may be used to indicate the effect of cell volume on the semiconductor bandgap.

$$\alpha_V = \frac{\partial E_g}{\partial lnV} \qquad (9)$$

The symbol Eg represents bandgap energy, whereas V represents cell volume. Most ambient-phase perovskites have a positive trend in α_VAccording to the initial results [110]. As a result of this upward tendency, the bandgap energy drops first, and then the crystal lattice constant or cell volume drops as well [111]. The increased orbital overlap resulting from the shorter bonds is the primary reason this phenomenon aligns well with experimental findings. As a result of pressure-induced phase transitions, crystal deformation or tilt can reduce orbital overlap, leading to a blue shift in the bandgap. Compression behavior of perovskite materials is very material-specific and intricate [112]. The esteemed team of researchers, led by H. Zhu, conducted an extensive investigation into pressure-induced bandgap engineering. Their study aimed to understand the causes of pressure-induced redshifts, blueshifts, and amorphization [113]. The optical characteristics of $FAPbI_3$ perovskite materials were studied under different

pressure settings. Using in situ absorption and PL measurements, they observed a strong correlation between the amorphization of $FAPbI_3$ nanocrystals and changes in optical characteristics brought about by pressure-driven phase transitions. The out-of-phase band-edge states are stabilized as the lattice expands since the fundamental band gap is determined at the boundary of the Brillouin zone (R for the pseudocubic structure). As the temperature drops (lattice contraction), the band gap drops from 1.61 eV at 300 K to 1.55 eV at 150 K, marking the beginning of a phase change, according to temperature-dependent photoluminescence [114]. Following the equation, smaller molecular cations are expected to have lower band gap values. The band gap is 0.3 eV smaller when NH_4^+ is used instead of $CH_3NH_3^+$ in the perovskite structure [115].

The Goldschmidt tolerance factor of $CH_3NH_3PbI_3$ is 0.91, indicating instability due to tilting of the cationic lead. A nonperovskite structure is preferred, and NH_4PbI_3 has a tolerance factor of 0.76. Because they do not conform to spherical symmetry, more asymmetric molecular ions ($NH_2CHNH_2^+$, or FA) can also cause "built-in" structural distortions. Band gap engineering must consider the physical and chemical stresses connected with molecular substitution [116]. Perovskites with distinct band gaps are used to create perovskite-based TSCs that can absorb a broader range of light. This method may surpass the Shockley-Queisser PCE limit seen in single-junction PSCs [117]. The energy band-gap of methylammonium lead iodide ($MAPbI_3$), a material with a high PCE and widely utilized, can be varied from 1.6 eV to 2.3 eV by changing the ratio of bromine to iodine [118]. Using a similar method, the band gap of formamidinium lead tri-halides (FAPbX3) could be tuned from 1.48 eV to 2.23 eV [119]. Optimization of metal halide perovskites for use as bottom or top cell absorbers in tandem or single-junction solar cells is achieved through compositional bandgap tuning. Compared to B- and X-site replacements in the ABX_3 phases, A-site substitution has a less direct effect on the edge of the band structure, i.e., E_g [120, 121].

2.3.3. Basics of PSC

A PSC is typically composed of a transparent electrode, which is generally made of conductive oxide; charge transport layers, which include an ETL and an absorber layer that is sandwiched between the charge transport layers; and a counter electrode, which is typically made of metal. The absorber material used in PSC devices, known as "perovskite," takes on the crystal structure of ABX_3. Strong optical absorption from the s-p anti-

bonding coupling, high electron and hole mobilities and diffusion lengths, outstanding structural defect tolerance and shallow point defects, low surface recombination rate, and favorable grain boundaries, because they do not encourage electron-hole recombination, are some of the favorable properties that make this type of material ideal for use as a PV absorber [122, 123]. The method of operation of PSCs is that Perovskite materials can effectively absorb photons with energy that is larger than the band gap width of the materials. This occurs when the cell is exposed to sunlight. Because of this, holes are created in the valence band, and excited electrons move from the valence band to the conduction band. Both of these phenomena will occur. After that, the electrons and holes inject themselves into the transport layer at the interface between the perovskite layer and the transport layer by way of the transport layer. The carrier is being delivered to the electrode to fulfill the goal of supplying energy to the external circuit, thereby generating electricity through PVs.

Several processes are involved in the operation of solar cells, including light absorption, charge separation, charge transit, and charge collection. The selection of light harvesters and the investigation of their optoelectronic properties are both necessary steps in the construction of these devices. For instance, a p-i-n junction is needed if the light harvester is an intrinsic semiconductor. On the other hand, a p-n junction is required if the light harvester possesses an n-type or p-type feature. This is because n-types and p-types are capable of transferring electrons or holes to the light harvester. Organometallic perovskite materials possess balanced charge transport capabilities, enabling them to be applied to both p-i-n junction and p-n junction types of devices [124]. There have been three recent breakthroughs in common PSCs: the mesoporous PSC (n-i-p), the planar PSC (n-i-p), and the planar PSC (p-i-n). The transparent conducting layer situated at the top of the ETL in the n-i-p configuration allows light to pass through because it is transparent. On the other hand, the p-i-n structures belong to the inverse configuration [125]. With their low-cost components, easy manufacturing method, and high PCE, Mesoporous PSCs (MPSCs) have recently garnered considerable attention. Before the compact layer, there is a fluorine-doped tin oxide (FTO) layer in MPSC [126]. This layer typically serves as both a hole blocker and an electron collector. The absorber layer around the ETL forms a tightly capping layer, and then an intermixed layer is created by penetrating it. The top electrode and HTL are sequentially deposited over the absorber layer to complete the device construction [127]. When scaling up, it is undesirable to have a high temperature, as the mesoporous layer requires

a lower temperature. When it comes to increasing PCE or improving stability, the question of whether a mesoporous layer is required at all remains open to debate. The use of planar PSCs (PPSCs) has become increasingly appealing as a result of its specific features, which include their low-temperature production procedure, low cost, and straightforward processing [128]. A compact ETL layer is what differentiates the planar n-i-p structure from the intermixed layer that is present in the mesoporous architecture (perovskite-ETL) [127]. Both ETL/Perovskite and Perovskite/HTL are available interfaces; as a result, ETL and HTL can separate the e-h pairings in an efficient and fast manner. PSCs with inverted structures (p-i-n) show great promise for highly effective and flexible PV devices [126]. Several advantages, including straightforward processing methods, high stability, and minimal hysteresis, are among the numerous benefits that PSCs with an inverted structure possess. Because the extraction layer of a carrier of the n-i-p structure is inverted, the planar p-i-n architecture is usually referred to as an inverted planar structure. This is because of the inversion of the structural layer. When constructing the p-i-n architecture, it is common practice to employ a planar structure that has a small HTL dimensions.

Additionally, it is a well-known fact that PSC devices consist of an active layer stacked between ultrathin carrier transport layers. These materials include an HTL and an ETL. There is a correlation between the energy levels, electron affinities, and ionization potentials of the bands and the band alignment. The ultra-thin layers, which have low electron affinities and ionization potentials, are used as materials that transport holes. In contrast, the materials that transport electrons are those with larger electron affinities and lower ionization potentials [129, 130].

2.3.4. Electron Transport Layer

Electrons are injected from the absorber layer into the ETL, also referred to as the electron-collecting layer or the electron-extraction layer. These electrons are then carried via electron-transporting materials (ETMs) while being collected by the electrode [131]. In addition to its role as a hole-blocking layer, the electron-transport layer also prevents holes from being released upon the front electrode [127]. Band alignment with the perovskite layer is the most significant property of an ETL. This means that the ETL must have a higher highest occupied molecular orbital (HOMO) and lowest unoccupied molecular orbital (LUMO) than the perovskite active layer. To facilitate photon absorption by the perovskite absorber, it should have a high

transmittance in the UV-visible spectrum. For the ETL or HTL to collect excitons generated by light absorption across the perovskite layer, the layer must first be separated. ETL generally consists of indium-gallium-zinc oxide (IGZO), zinc oxide (ZnO), titanium dioxide (TiO_2), tin oxide (SnO_2), 6,6-phenyl-C61-butyric acid methyl ester(PCBM), etc [127]. The role of the ETL in PSCs is illustrated schematically in **Figure 7**.

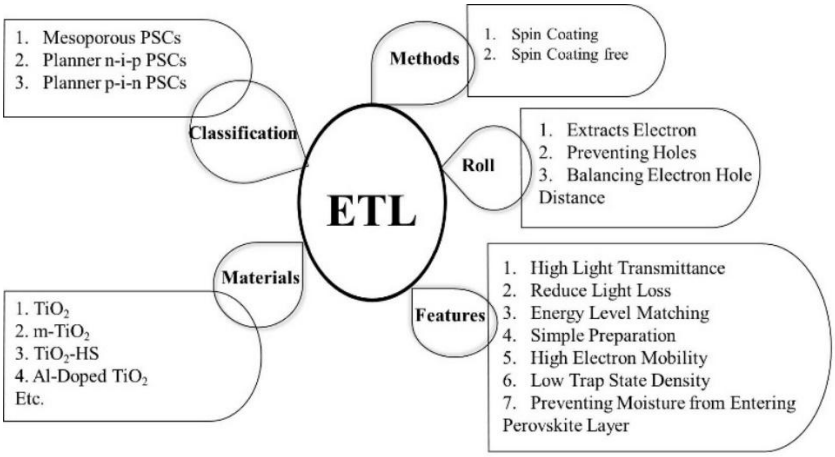

Figure 7. The operation of the ETL in PSCs is schematically shown.

For an ETL to be considered appropriate, it must possess an energy band position that corresponds to the perovskite material. To allow electron injection, the position of the conduction band should be slightly below the conduction band minimum of the perovskite layer. On the other hand, the valence band should be positioned at a deeper level to block holes and have high electron conductivity to ensure electron transit and collection [132]. A wide band gap and low absorbance at visible wavelengths are desirable properties of the ETL in an n-i-p structure, which minimize optical energy losses. To prevent light from scattering and being reflected, the ETL should also be anti-reflective. Furthermore, to avoid charge current leakage, the compact ETL must not contain any pinholes. To facilitate the infiltration of perovskite material into the mesoporous structure, the ETL's porosity should be sufficiently high. To avoid low shunt resistance caused by direct contact with the HTL, it is critical to fill the perovskite material. Furthermore, the presence of air within the voids of the mesoporous ETL could compromise the stability of the PSC by accelerating the degradation of the perovskite

material [133, 134]. Taking all of these into consideration, the perfect ETL would guarantee perovskite morphology of high quality, reduce recombination tendencies and charge accumulation, and improve device stability while indirectly lowering the hysteresis effect. In dye-sensitized solar cells, TiO_2 ETLs are found to be in extensive use. Not only does TiO_2 have an efficient ability to block holes at the perovskite interface, but its conduction band maximum (CBM) is −4.4 eV, and its valence band maximum (VBM is −7.63 eV [135]. Typically, a high-temperature procedure is needed to fabricate a TiO_2 film. However, a colloid-spray coating method has recently been disclosed that enables the creation of a TiO_2 layer at 100 °C [136]. 0.1 to 4.0 $cm^2\ V^{-1}\ s^{-1}$ is the electron mobility observed in TiO_2 material, which is below average [137]. Three methods are frequently employed to circumvent the TiO_2 ETL's limited mobility. A new electron transport material with better intrinsic optoelectronics characteristics could be used as a first Step. For example, SnO_2 and ZnO exhibit 240 and 205-300 $cm^2\ V^{-1}\ s^{-1}$, respectively, in terms of mobility [138]. Altering the ETL using dopants is the second strategy. The mobility of SnO_2 and EDTA-doped SnO_2 films was found to be 9.92×10^{-4} and 2.27×10^{-3} $cm^2\,V^{-1}\,s^{-1}$, respectively, according to Yang et al.[139] Finally, enhancing the surface area of ETLs is possible by sandwiching a thin interlayer between the ETL and perovskite interfaces [140].

2.3.5. Hole Transport Layer

Collecting and transporting holes from the perovskite light-absorbing layer is the primary purpose of the HTL. This, in turn, helps the ETL separate the electron-hole pairs in the perovskite materials. To speak more generally, HTL performs several specific functions, including the following: it extracts and transports the holes in the active layer to the electrode; it acts as an energy barrier to prevent the transfer of electrons to the anode; it separates the perovskite layer from the anode and isolates the moisture in the air; it improves the stability of the device by reducing the possibility of degradation and corrosion; and it can assist in improving the open circuit voltage (V_{oc}) when its HOMO energy level is well matched [141]. Based on the HOMO energy levels corresponding to the valence band of the preferred perovskite material, appropriate HTLs can be selected when needed. Remember to consider the following aspects when selecting a suitable HTL. It should also be made of materials that are readily available and inexpensive, fabricated using procedures that are solution-processable, exhibit high hole mobility, and possess good thermal, moisture, and UV

stability [142]. To aid effective carrier transport, out-of-plane oriented crystals can be formed with the help of an appropriate HTL. Common performance losses, however, include carrier recombination and carrier extraction, which exhibit a specific negative correlation, as well as the collection of hole carriers by processes occurring in the perovskite layer and HTL. The main factors contributing to the excellent performance of perovskite devices are the low defect density and high carrier transport rate. Transporting materials for carriers is crucial. It is crucial to match the bandgap to separate the charges and prevent them from recombining [143, 144]. It is the characteristics of HTL, including a large bandgap, high conductivity, high transparency, and an appropriate energy level, that determine the efficiency of carrier transmission. As demonstrated in **Figure 8**, the energy levels of some transport materials (TMs) and other materials widely utilized in PSCs are displayed [143].

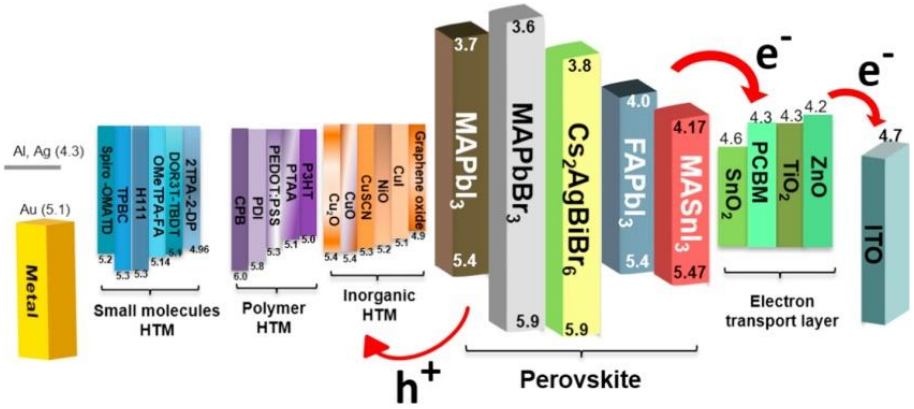

Figure 8. Schematic depicting the energy levels of TMs that are frequently adopted.

The thickness of the HTL determines both the performance and the stability of the devices, which is another crucial issue to consider. However, at the same time, it may reduce the uniformity of coverage, particularly when the perovskite surface is composed of large crystallites. This is because thinning the HTL should not only reduce the distance traveled by holes to reach the counter electrode but also reduce the probability that they will undergo recombination. Furthermore, it is a well-known fact that the counter electrode engages in a reaction with the iodide ions present in the perovskite, resulting in the rapid degradation of the devices. Because of this, it is essential to make use of an HTL that is suitably thick to safeguard against direct contact between the perovskite and the counter electrode [145,

146]. When compared to perovskite, a thicker HTL would homogeneously cover the rough perovskite surface; nevertheless, this would result in high series resistance because of the significantly poorer hole mobility experienced by HTL. It is of the utmost importance to exercise careful control over the thickness of the HTL to achieve complete coverage of the rougher perovskite layer without increasing the series resistance of the devices. As a result, this would lead to devices with high levels of performance, stability, and reproducibility.

Having an intrinsically high hole mobility, acceptable energy levels corresponding to the perovskite layer, long-term stability in air, and good photochemical and thermal stability are all characteristics that an ideal candidate for HTM should possess. Additionally, it must be subjected to solution processing to manufacture HTL, particularly when it is used in typical (n-i-p) devices [147, 148]. It is essential to underline the fact that organic HTMs have several benefits over their inorganic counterparts. These advantages include the ability to modify molecular structures, the ability to vary energy levels, compatibility with the perovskite layer, and the capability to be processed in a solution at low temperatures. Small molecular organic HTMs and polymer HTMs are the two categories that describe the available organic HTMs. Small-molecular organic HTMs have structures that are characterized, which makes purification and characterization of these compounds much simpler. Furthermore, small molecular organic HTMs can produce compact and homogeneous films on the perovskite layer, thereby enhancing the efficiency of charge transfer and extraction. Small molecular organic HTMs consist of Spiro-OMeTAD, Poly[bis(4-phenyl)(2,4,6-trimethylphenyl)amine] (PTAA), and certain derivatives of these compounds [149]. To provide more functionalization and modification, polymer HTM structures are larger and more complex than their counterparts. By forming interpenetrating networks with the perovskite layer, polymer HTMs can also enhance the mechanical stability of the material and reduce the number of defects that occur at the interface. Poly(3-hexylthiophene) (P3HT), Poly(3,4-ethylenedioxythiophene), poly(styrene sulfonate) (PEDOT: PSS), and their derivatives are examples of polymer HTMs. The electrical and optical properties of organic HTMs, as well as their interactions with the perovskite layer and the anode, are all determined by the molecular structure of these materials [150]. It is generally recommended that organic HTMs have a structure that is both planar and rigid. This structure should enable stacking and orbital overlap, thereby enhancing the efficiency of hole transport and extraction. HTMs were

initially implemented in all solid-state PSCs in 2012, coinciding with the introduction of organic spiro-OMeTAD. While spiro-OMeTAD continues to be the most widely used HTM for high-performance PSCs, it is only effective when used in conjunction with certain additives. The size of crystallites, surface uniformity, and film morphology may all be controlled with the use of additives [151]. For instance, 4-tert-butylpyridine (tBP) and bis (trifluoromethane) sulfonimide lithium salt (Li-TFSI) are two examples of additives that need the presence of spiro-OMeTAD [152]. When compared to organic HTM, inorganic p-type semiconductor materials have the potential to replace organic HTM. This is owing to the advantages that these materials possess, which include high hole mobility, a wide band gap, and a straightforward solvent treatment method. There have been numerous reports of inorganic materials that are capable of transporting holes, including CuI, NiO, $CsSnI_3$, and CuSCN. CuI has a conductivity that is superior to that of Spiro-OMeTAD; hence, CuI is a formidable rival to Spiro-OMeTAD because it efficiently enhances the filling factor of the device and is consequently a potent competitor [153]. The electrical and optical properties of inorganic HTMs, as well as their interactions with the anode and perovskite layer, are influenced by the procedures of synthesis and preparation that are used to create these materials.

Additionally, the crystallinity, purity, and stoichiometry of these materials are all influenced by these component combinations. For the most part, the synthesis of inorganic HTMs can be accomplished using a variety of techniques, including, but not limited to, sol-gel, hydrothermal, spin coating, spray coating, sputtering, evaporation, chemical vapor deposition, and atomic layer deposition methodologies. The methodologies for synthesis and preparation are determined by the properties that are desired, as well as the compatibility of the inorganic HTM with the perovskite layer and the anode [154]. The efficiency of inorganic HTMs in extracting and transporting holes from the perovskite layer to the anode, as well as their susceptibility to recombination and energy loss, are all regulated by their energy levels. To minimize energy loss and recombination rate, inorganic HTMs should typically have a high-lying VBM level that matches the VB of the perovskite layer and the anode's work function. This is in addition to having a high ionization potential. Inorganic HTMs should also have a wide band gap to avoid parasitic absorption and interference from the perovskite light-harvesting layer [155].

2.4. Development from Single-cation to Triple-cation Perovskites

In modern PVs, lead halide perovskite materials constitute a significant breakthrough. It is possible to define the archetypical organic-inorganic (hybrid) perovskite by using the structure ABX_3, where A represents a monovalent organic or inorganic cation, such as MA, FA, or Cs^+, B represents a divalent metal cation (Pb_2^+ or Sn_2^+), and X represents a halide (Cl^-, Br^-, I^-) [156]. A significant number of studies have been conducted worldwide to stabilize devices and enhance their operational effectiveness. Within the perovskite film, the ideal Goldschmidt tolerance factor and octahedral factor are required to improve the film's internal stability [157]. The tolerance factor can be increased by employing a greater size cation at site A. The use of a larger cation at the B site reduces the tolerance factor while simultaneously increasing the octahedral factor. Altering the perovskite composition is one strategy that can be employed to achieve a more durable and efficient PSC [158]. The Bandgap and absorbance of the device remain unchanged whether the A-site cation ratio is changed or new A-site cations are introduced. On the other hand, it can improve performance by adding or removing surface imperfections and making surfaces smoother with larger grains. A change in any ratio also changes the octahedral factor and the Goldschmidt tolerance factor [159]. Consequently, cations (and anions) in the perovskite formula can alter the intrinsic stability. Various ratios of FA and methyl ammonium (MA) have traditionally been employed for perovskite film production. To achieve devices with a higher PCE, tiny amounts of rubidium (Rb) and Cs have been utilized recently [160]. Compared to $MAPbI_3$, $FAPbI_3$ is more cubic due to the FA cation's slightly greater ionic radius of approximately 2.79 Å, resulting in a t-value of around 0.987 [161]. There are two distinct phases of the $FAPbI_3$ perovskite: the cubic photoactive phase (α-$FAPbI_3$) and the hexagonal non-photoactive phase (δ-$FAPbI_3$). The $FAPbI_3$ perovskite has a significant problem with phase instability due to the larger and more uneven FA groups. This causes it to transition from the α-$FAPbI_3$ phase to the δ-$FAPbI_3$ phase at room temperature, and it is further affected by solvents and humidity [162, 163]. At room temperature, $CsPbI_3$ crystallizes into a non-photoactive orthorhombic δ-phase ("yellow" phase), but the cubic photoactive α-phase ("black" phase) is only stable at temperatures exceeding 300 °C. On the other hand, the purely inorganic $CsPbI_3$ perovskite displays remarkable thermal stability with an appropriate band gap of approximately 1.73 eV [164].

2.4.1. The Single Cation

A methylammonium cation (MA; $CH_3NH_3^+$) is located at the A site, lead (Pb_2^+) at the B site, and halides (Cl^-, Br^-, I^-) at the X site in the most popular 3D hybrid perovskite. When used at the A site, organic formamidinium (FA; $H_2NCHNH_2^+$) or Cs^+ cations are two more typical methods for obtaining perovskites [165]. $MAPbI_3$ is arranged in a cubic lattice with the highest degree of symmetry in its crystal structure. As the temperature drops, it transitions, becoming a tetragonal phase at 42–57°C and an orthorhombic phase at -113°C. Materials used in optoelectronic devices may experience changes in performance due to alterations in their electronic band structure resulting from these transitions [166]. At room temperature, the MA cations reposition themselves inside the octahedral cage at approximately 14 ps. It is believed that the dynamic reorientation of MA might stabilize the energetic charge carriers by creating a large polaron, which would then increase the lifespan of both hot and band-edge carriers [167, 168]. The breakdown of $MAPbI_3$ under lighting or high temperatures, possibly related to the volatilization of the MA cations, is caused by the unstable nature of the weak bonds underlying the hybrid organic-inorganic perovskite, as highlighted by this dynamic disorder. An alternative to the volatile organic cations MA and FA is a fully inorganic $CsPbI_3$ perovskite [169].The commencement of the thermal degradation ($650 \pm 90\ kJ\ mol^{-1}$) of $CsPbI_3$ requires a very high activation energy, as the Cs cation forms a strong chemical bond with the octahedral lattice, in contrast to the weak hydrogen bonding of organic cations [166]. However, when exposed to ambient temperature, a nonperovskite orthorhombic phase forms because of the Cs cation's modest ionic radius (Goldschmidt tolerance factor of 0.81). The cubic phase of $CsPbI_3$ perovskite crystals develops at temperatures greater than 300 °C; however, when exposed to room temperature, these crystals are thermodynamically unstable and quickly return to their orthorhombic forms. Increasingly, scientists are focusing on perovskite TSCs to gain a deeper understanding of them, as the initial report was based on a single-cation $MAPbI_3$ [170]. Nevertheless, $MAPbI_3$-based perovskite TSCs typically perform below optimally due to the material's bandgap not satisfying the criteria of the ideal top cell [171]. Many people are interested in using inorganic perovskites with better bandgaps in perovskite TSCs since they are more stable and have a longer lifetime than $MAPbI_3$. One example is $CsPbI_3$, which has a bandgap of 1.72 eV [172]. By passivating the halogen vacancies on the surface of the perovskite thin film and suppressing non-

radiative recombination, Zhang et al. significantly improved the V_{OC} and PCE of inorganic perovskite $CsPbI_xBr_{3-x}$. This work aimed to achieve the first inorganic PSCs/Si TSCs with an impressive PCE of 22.95% and a high VOC of 2.04 V. Plus, after 300 hours of continuous illumination under maximum power point tracking (MPPT) in a nitrogen atmosphere, the devices maintained 95.7% of their initial efficiency, demonstrating excellent stability [173]. Due to their exceptional optoelectronic characteristics, hybrid perovskites function excellently in solar cells. These semiconductors have a direct bandgap, and the halides primarily determine their electrical structure. The optical transition is strongly impacted by the halide p orbitals. The band energy can be marginally affected by variations in the B cation as well. Because hydrogen's 1s orbital and carbon and nitrogen's 2p orbitals do not substantially add to the density of states close to the Fermi level, bandgaps are only faintly affected by A organic cations. However, hydrogen bonding and van der Waals interactions allow the A ammonium cations to deform the $(BX_6)^{2-}$ framework, which in turn affects the bandgap.

2.4.2. The Double Cations

To stabilize the black α-phase of $FAPbI_3$ in perovskite polycrystalline films, it was common practice to partially replace FA with smaller cations such as MA, Rb, or Cs, and I with Br. This led to a multitude of mixed cation and halide compositions. Consequently, the black α-phase of FA-based perovskites was mainly stabilized by adding cations or halogens to single-crystal perovskites [174, 175]. The incorporation of smaller MA^+ compared to the FA^+ results in a contraction of the unit cell volume, which adjusts the effective Goldschmidt tolerance factor to approaching 1, indicative of a perfect cubic perovskite structure. Additionally, the strong dipole and rapid rotation of MA^+ were discovered to produce a greater degree of cation disorder, which could potentially increase the effect of entropy and stabilize the α-phase thermodynamically. It was determined that the Br^- incorporation induces anticipated nucleation from a kinetic perspective, as evidenced by the rapid perovskite growth as the bromine content increases. The black phase of mixed cation/halide SC with high crystallinity and low defects may be favored by Br inclusion due to the cubic structure and lower surface energy of $MAPbBr_3$ [176]. The optimal range for preventing $MAPbBr_3/FAPbI_3$ phase separation was also determined to be between x = 0.10 and 0.15. The growth was ultimately achieved on a centimeter scale with a long carrier lifetime of 11.0 μs, composed of $(FAPbI_3)_{1-x}(MAPbBr_3)_x$ SC. Because perovskites with double-cation

components exhibit superior optical and thermal stability compared to those with single cations, they are among the most frequently investigated systems by research groups interested in perovskite TSCs. For instance, Bush et al. swapped some I^+ and FA^+ for Cs^+ and Br to develop a stable perovskite absorber layer. Their perovskite TSCs survived a 1000-hour damp heat test at 85°C and 85% RH thanks to the combination of PSCs and a Si heterojunction (SHJ), resulting in a PCE of 23.6% [177].

2.4.3. The Triple Cations

Single crystals of triple-cation mixed-halide perovskites were recently created using the ITC method. Initially, by substituting a portion of the $MAPbBr_3$ precursor with $CsPbBr_3$, a sequence of mixed-cation/halide perovskites containing Cs single crystals with varying compositions, denoted as $(FAPbI_3)_{1-x-y}(MAPbBr_3)_y$ $(CsPbBr_3)_x$, had been produced [178]. The authors discovered that the stability of perovskite SCs is affected by the Br and Cs concentrations, so it's essential to set these values correctly. The ideal formula was determined to be $(FAPbI_3)_{0.9}(MAPbBr_3)_{0.05}$ $(CsPbBr_3)_{0.05}$, which exhibited outstanding stability under environmental conditions, including light and heat stressors, and a lengthy carrier lifetime of 16 μs. Most perovskite layers used in high-efficiency perovskite TSCs are composed of triple-cation perovskites. These films exhibit greater optical and thermal stability, are typically smaller in size, and do not contain any pinholes.[8] Using a perovskite composition of $Cs_{0.05}(FA_{0.77}MA_{0.23})_{0.95}$ $Pb(I_{0.77}Br_{0.23})_3$, Albrecht et al. found a PCE of 29.15% for perovskite TSCs [179]. The perovskite TSCs achieved an open-circuit voltage of 1.92 V due to their fast hole extraction rate and suppressed non-radiative recombination at the hole-selecting interface. They showed excellent stability, keeping their initial efficiency at 95% after 300 hours of operation without encapsulation. Additionally, our team disclosed that an effective solar cell was created by combining a semi-transparent perovskite top layer with an industrial n-type bifacial monocrystalline PERT Si bottom cell [180]. The cell is referred to as a triple-cation perovskite/Si TSC. The final design set a new benchmark for PCE among four-terminal architectures, reaching 26.6%. The Si bottom cell contributed 7.2% to the total PCE, whereas the top cell perovskite alone achieved 19.4%.

2.5. Charge Transport, Recombination Mechanisms, and Carrier Dynamics

2.5.1. Charge Transport

When subjected to an electric field, the number of holes and electrons, as well as the directionality of their flow, determine a semiconductor's electrical conductivity. An event called a scattering time or characteristic mean time between scattering events, abbreviated as τ, limits the flow of carriers because carriers with a high instantaneous velocity often scatter off-lattice vibrations (phonons), defects, and impurities. Compared to their instantaneous velocity, the net flow velocity, also called drift velocity, of a stream of carriers is significantly lower. When an electric field is applied to a charged particle, the result is drift. Evenly doped semiconductor bands will be inclined upwards when an electric field passes through them. Electrons in the conduction band move counter to the applied field because of their negative charge, while holes in the valence band move parallel to the applied field because of their positive charge. Theoretically, this is a valuable tool for studying the movement of electrons and holes through semiconductors. Here we have Ohm's law, which summarizes the experimental data or

$$J = \sigma \mathcal{E} \qquad (10)$$

This is an equation for the current flow in response to an applied electric field $\mathcal{E}$, which is collision-limited. This can be better understood by examining Figure 9, which illustrates the x-direction carrier flow in a solid cylinder with a cross-sectional area A.

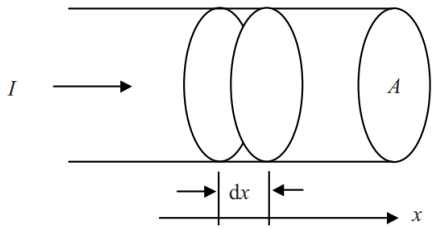

Figure 9. Current flows along a solid semiconductor rod of cross-sectional area A.

The electrons and holes would continue to speed up freely if there were nothing to slow them down. However, there are many things in the semiconductor crystal that the carriers can't avoid, so they end up scattered. Crystal atoms, dopant ions, crystal flaws, and other defects, such as electrons and holes, are all examples of such objects. Carriers move on a tiny level, like a pinball machine ball; they continually bounce off crystal objects,

although they mostly follow the direction of the applied electric field. The amount of charge *dQ* passing across a specific plane in the cylinder in time dt is $dQ = nqAdx$ if the carrier concentration is n and each carrier carries a charge q that moves a distance dx in time dt. Carrier drift velocity is represented by $v = \frac{dx}{dt}$, and it is evident that the current is

$$I = \frac{dQ}{dt} = \frac{nqAdx}{dt} = nqAv \qquad (11)$$

Additionally, we define the current density as $J = I/A$, which leads to the formulation of Ohm's law. This phenomenon, referred to as the drift current, necessitates the presence of an electric field.

$$J = nqv = \sigma\mathcal{E} \qquad (12)$$

Charge carriers in inorganic semiconductors, such as Si and Ge, move as highly delocalized plane waves, and their mobilities are frequently significantly greater than 1 cm^2/Vs. Covalent bonds with high bonding energy characterize these semiconductors. Carrier scattering causes the mobilities of these systems to decrease as the temperature increases. In contrast, organic semiconductors are primarily held together by weak van der Waals forces, which have bonding energies comparable to the vibrational energies of molecules at normal temperatures, and they are composed of π-conjugated units. Also, molecular orbitals overlap because molecules are spaced far enough apart. So, hopping is how charges are transported in organic semiconductors. In contrast to inorganic semiconductors, organic semiconductors exhibit enhanced charge carrier mobilities at high temperatures. In the case of organic semiconductors, it is crucial to understand the fundamental charge transport mechanisms at both the molecular and device levels.

2.5.2. Recombination Mechanisms

Electrodes would capture electrons and holes successfully converted from each incident photon. However, the overall PCE of organic PV devices is restricted by the potential loss mechanisms present in each stage of the aforementioned PV process, from absorption to collection. After an absorbed photon, the exciton has only a few nanoseconds to reach a donor-acceptor interface before it relaxes to the ground state. The electron-hole pair is more likely to recombine than separate if the domain sizes exceed the exciton diffusion length. The concentrations of electrons (n) and holes (p) in a semiconductor tend to relax back toward their equilibrium values when the material is taken out of thermal equilibrium, for example, by illumination and/or current injection. This relaxation is caused by recombination, in

which an electron falls from the conduction band to the valence band, eliminating a valence-band hole. Geminate recombination is the term used to describe these recombination processes, which involve an electron-hole pair resulting from a single photon event. In this context, the electron-hole pair is like twins born from the absorption of a single photon; the term geminate originates from the Latin word gemini, meaning twins. Research into the factors that cause geminate pairs to recombine or dissociate into free carriers is ongoing. Electrons and holes must reach their respective electrodes after geminate pairs have been successfully separated into free carriers. They must avoid recombining with another free carrier that has an opposing charge. A process known as nongeminate recombination occurs when free electrons and holes combine. In bimolecular recombination, two molecules' charge carriers recombine in different charge-transfer states. Alternatively, in geminate (monomolecular) recombination, charge carriers originate from the same exciton recombination. For this kind of recombination, two options exist. In the charge transfer state, the two charges are Coulombically coupled, opening the door to geminate recombination. The second condition for recombination to be a geminate process involving only one molecular bond is that, even after the charges have escaped the Coulombic pull, they remain structurally limited to their respective domains, allowing only the original hole to participate in recombination.

Recombination in crystalline inorganic semiconductors (GaAs, Si, etc.) falls into one of three categories: band-to-band, via defect levels, and Auger. The semiconductor's electronic structure is a significant factor in the types of recombination. As a result of band-to-band recombination, radiative processes, including luminescence, are generated in direct bandgap semiconductors. The density of accessible electrons and holes is directly proportional to this recombination. A single transition from a conduction band state to an empty valence band state is all it takes for an electron to undergo band-to-band recombination. This process is called radiative recombination because most of the excited carrier's energy is dissipated through photon emission.

In indirect bandgap semiconductors, the band-to-band recombination is negligible; however, the dominant recombination mechanism is Shockley–Read–Hall recombination, which is facilitated by the interchange of thermal energy with a phonon on defect levels. The process of surface recombination is highly comparable. As a result of contaminants and abrupt terminations (the existence of electrically active dangling bonds), surfaces and interfaces frequently serve as trap sites. Another significant consequence in inorganic

semiconductors that are extensively doped is Auger recombination, which involves the transfer of energy from one electron or hole to another through band-to-band recombination. Since the recombination rate is affected by the presence of a third particle, Auger recombination differs from band-to-band recombination in how it should be managed. Auger recombination processes engage three carriers, where the energy released during the recombination of an electron-hole pair elevates a third carrier to a high-energy state. The relaxation of the carrier to the band edge energy typically eliminates the resulting gain of the kinetic energy of the third particle, the electron [181]. So, it's a nonradiative three-carrier process, generally described as

$$R_{Auger=}(C_n n + C_p p)(np - n_i^2) \qquad (13)$$

Where C_n and C_p denote the Auger coefficients, numerical values for the C_n and C_p coefficients are calculated from first principles.[181-183]

2.5.3. Carrier Dynamics

If accurate doping control had not been implemented, it would have been impossible to create diodes, transistors, semiconductor lasers, and other materials. Halide perovskite materials and devices are likely to have flaws of the same paramount significance. Halide perovskite can exist in a variety of deep and shallow defect states. Because of their solution chemistry, halide perovskites are attractive for use in affordable PVs. Additionally, the components, such as iodide, are highly reactive, which presents opportunities for both intentional doping and unintentional defect development [184]. Flaws can have several impacts, including quenching of luminescence and charge trapping. Another result is the luminescence at longer wavelengths, which is reported at low temperatures. Because shallow faults cause charge to be trapped and then released, the mechanism that transports charges is slowed down [185]. Given these facts, it is clear that phonon-assisted absorption and recombination happen quite frequently. The indirect nature of the transitions may be the reason for the substantial carrier-phonon coupling and the poor PL quantum efficiency (PLQE), both of which are not ideal for applications in the field of optoelectronics. In all of the lead-free perovskite nanocrystals that were examined, notably $Cs_3Bi_2X_9$, Cs_2AgBiX_6, and $Cs_2AgSb_{1-y}BiyX_6$ (where y is a value between 0 and 1), it was observed that there were indirect band gaps. $Cs_2AgBiCl_6$, a semiconductor with an indirect band gap, exhibits a low PLQE, which is less than 0.1% for NCs that do not contain any ligands [186, 187]. $Cs_2AgInCl_6$ was found to have a direct band gap, according to the findings. On the other

hand, the parity-forbidden direct transition is responsible for the poor optical absorption coefficients that are observed at the band gap [188, 189]. HC in perovskites has been receiving a lot of attention, in addition to the dynamics of charge carriers at lower excited states near the band edge. This is because the cooling process has slowed down, making the matter more complicated. It is possible that, due to this, harvesting hot charges will be feasible in an effective manner, which will enable solar cells to surpass the standard thermodynamic Shockley-Queisser limit of 33%. It was previously established in early transient absorption (TA) studies that the hot-phonon bottleneck occurs when the rate of cooling of hot charges in $MAPbI_3$ perovskites slows down at large carrier densities. This phenomenon is also known as the hot-phonon bottleneck. Optical phonons are responsible for this phenomenon due to their significant carrier re-absorption [190, 191]. Even though TA investigations offer a plethora of information and may be accessible with a high degree of temporal resolution, it is essential to point out that the spectra of these materials are incredibly intricate. To conduct an accurate analysis, it is crucial to consider effects such as ground-state bleaching, band-gap renormalization, state filling, and changes in refractive index. For short time scales of less than 0.5 ps, it was claimed that carrier thermalization occurred within 100 fs. The values for 10^{18} and $10^{19}cm^{-3}$ varied from 10 to 85 fs, determined by the excitation density [192]. Recent studies conducted in single-crystal $MAPbBr_3$ and $FAPbBr_3$ microplates have shown that the slow hot charge cooling phenomenon remains true even in the low carrier density region ($<10^{17}$ cm^{-3}), which is far below the hot-phonon bottleneck domain. Although perovskites are transparent to ultrafast TA microscopy, they can transfer high-energy charges over a substantial distance, approximately 230 nm [193]. According to the increasing level of research conducted in this area, it appears that heated carriers in Pb-based halide perovskites undergo at least two distinct cooling processes. Firstly, the duration can range from subpicoseconds to 2 ps, depending on the sample and the examination method. Given the multiple cooling steps, it is highly likely that several factors are contributing to the outcome. This is because the existing hypotheses for the extended heat carrier lifetimes in perovskites are different. The following processes must occur to dissipate the excess energy: optical phonon decay and acoustic phonon conduction of heat out of the system [194].

2.6. Hot carrier phenomena in solar cells

When a semiconductor absorbs a photon, it forms a pair of electrons and holes. The excited state transition from the valence band to the conduction band involves an electron. Many relaxation and recombination processes influence the distribution of photogenerated carriers. For example, absorbing photons whose energies are far higher than the bandgap is possible. The electrons are referred to as HC due to their significantly greater energy than the lowest states of the conduction band. Simply put, HC is charged particles, such as electrons or holes, propelled to extremely high kinetic energies in areas with a strong electric field. Hot electrons, with their high kinetic energy, tend to become trapped and accumulate in areas where they shouldn't be, creating space charge regions that can render the device unstable or degrade it.[195] Upon deexcitation, HC transforms its surplus energy into heat. The following equations characterize the distribution of the extra energy among the HC:[196]

$$\Delta E_e = (h\nu - E_g)\left[1 + \frac{m_e^*}{m_h^*}\right]^{-1} \quad (14)$$

$$\Delta E_h = \left(h\nu - E_g\right) - \Delta E_e \quad (15)$$

Where the effective masses of the electron and the hole are denoted by m^*_e and m^*_h, respectively, the difference in energy (ΔE_e) between the conduction band and the starting energy of photogenerated electrons and the valence band and photogenerated holes (ΔE_h) [196].

Photoexcited HC undergoes thermal cooling because of energy losses caused by carrier-carrier collision, HC scattering from lattice phonons, and other processes. The scattering process continues until the HC energy is lower than the phonon energy of the longitudinal optical (LO). Within one hundred picoseconds, the LO phonons released by the electron-LO scattering break down into shorter-lived acoustic or transverse optical phonons. After cooling, HC can be lost through recombination or moved to the charge transport layers (either the hole-transport layer or the electron-transport layer). Two steps comprise the HC relaxation process. Collisions between HC (electro-electron and hole-hole collisions) or, if their concentration is large ($>10^{18}$ cm^{-3}), and Auger recombination, begin in the first stage when the HC is far from equilibrium. This "carrier-cooling" process happens on the picosecond timescale. When the system is fully relaxed, the equilibration is complete. Now that the electrons and holes are in their respective energy

bands, they can undergo recombination through radiative or nonradiative processes or be transferred to the charge transport layers (in PV devices).

2.6.1. The Concept of Relaxation

Perovskite sensitizers are used in PV applications because they can absorb sunlight and create electron-hole pairs with energies that are significantly higher than the band edge. The excited charge-carrier distribution from an initially out-of-equilibrium state begins to relax as it approaches the band edge due to several reasons that contribute to this relaxation; for typical inorganic semiconductors such as GaAs, the processes responsible for this initial charge-carrier relaxation have been systematically and extensively examined. High charge-carrier mobilities and low exciton binding energies are two of the properties that hybrid lead halide perovskites have demonstrated. These characteristics are typical of traditional direct organic-inorganic semiconductors [146, 197]. Increasing the relaxation period of the HC will, in theory, make it possible to surpass the Shockley-Queisser (SQ) limit. Furthermore, according to a theoretical calculation, the efficiency of a solar cell based on a single junction of HCs and exposed to one sun irradiation can be increased to 66% [198]. There are two steps to the HC relaxing procedure. When the HC is not yet in equilibrium, the first Step begins with collisions between them, either through electron-hole collisions or, if their concentration is large ($>10^{18}$ cm^{-3}), through impact ionization and Auger recombination. "Carrier thermalization" is the process leading to redistribution excess energy and reaching electronic thermal equilibrium. HC reached the electronic equilibrium in less than 100 fs [196, 199]. As soon as the HC reaches the state of thermal equilibrium, the second phase of the HC relaxation process starts. Through the process of carrier-phonon inelastic scattering, equilibrium is attained between the lattice and the HC crystal structure. The phenomenon referred to as "carrier-cooling" begins to occur at the picosecond scale [200]. The electrons and holes are now in their respective energy bands, which means that they can be employed for recombination through radiative or nonradiative processes, or they can be moved to the charge transport layers (in PV devices). Temperature and the duration of the hot carrier are estimated to be the most significant limiting parameters, according to theoretical studies that consider the thermodynamic equilibrium of hot carrier relaxation, equilibration, and extraction rates [201]. Extensive research has been conducted on organic-inorganic lead halide perovskite materials to manipulate HC dynamics through doping and various chemical modifications, including alterations to cation (A^+) and

halogen (X^-) groups. At a low photoexcitation level (10^{17} cm^{-3}), Xing et al. studied the effects of HC cooling dynamics and extractions on Zn-doped $CsPbI_2Br$ [202, 203]. The Zn-doped perovskite showed an HC cooling rate that was three times lower than the undoped perovskite due to its improved film structure and lower defect density. In addition, the formation of relaxation channels due to Zn and the nonadiabatic coupling between conduction bands are the leading causes of delayed carrier cooling and efficient extraction at the interface. Modifying the cations of lead halide perovskite materials is a straightforward method that can be employed to enhance the HC lifetime of these materials. As a consequence of charge-state localization around the Cl atom, nonadiabatic electronic coupling occurs. Moreover, a similar experiment discovered that slower HC relaxation dynamics are observed when the concentration of chlorine (Cl) increases [204]. The function of the A-site cation was investigated by Yang et al. using ab initio calculations and ultrafast spectroscopic techniques. Among the three pure $APbI_3$ compositions (A being MA, FA, or Cs), the two-hybrid organic-inorganic materials exhibited a relaxation period that was longer than that of the Cs-based all-inorganic variation [205]. Zhu et al. investigated transient PL spectra, and their findings indicated that $CsPbBr_3$ did not exhibit such an impact. After doing their research, they discovered that $MAPbBr_3$ and $FAPbBr_3$ each have their own distinct carrier cooling phase. Having started at 0.5 ns, the temperature decline had slowed down to 680 K by the time 10 ns had passed. This was after it had begun [168].

2.6.2. Auger Heating Effect

The Auger heating effect in PVs refers to Auger recombination, a primary non-radiative process that occurs in semiconductors. In Auger recombination, the energy from an electron and a hole recombining is transferred to another carrier, which may be either an electron or a hole. Although this third carrier has more energy, it does not retain it for an extended period. Because of this interaction, the energy quickly dissipates into the surrounding crystals as heat rather than being converted into other proper forms, such as light or electricity [206]. The Auger heating effect is when electronic energy is converted into heat. Auger recombination is more noticeable in PVs when carriers are present in high concentrations, typically due to intense sunlight or bright illumination. Therefore, a significant portion of the solar energy used is converted into heat within the material, rather than being utilized to generate electricity. As a result, the efficiency of the solar cell decreases, and the device may overheat, which worsens its

performance by reducing the open-circuit voltage and accelerating the deterioration of its materials [207]. This heating effect is significant in today's PV materials, such as metal halide perovskites, and in multijunction solar cells, where energy production is particularly high. Therefore, controlling and minimizing Auger heating helps make new solar cells more efficient and longer-lasting [208]. As stated by Fu et al., the Auger heating effect was initially described in films composed of $MAPbI_3$. According to the findings of their investigation, the Auger heating effect has the potential to further prolong the lifespan of HC to tens of picoseconds [199]. As a result of both carriers using the excess energy for preexcitation, the relaxation rate of the carriers is increased. Even though the total energy of the electron-hole (e-h) pair does not change after e-h recombination, the heating of the electronic system can nonetheless make it more difficult to return to its original state. The bandgap is denoted by the equation E_g, and the quantity of energy that is provided to the electronic system by recombination is exactly proportional to the sum of E_g+E [209]. The following is an expression that can be used to describe the dynamics of carrier cooling, which includes the Auger heating effect.

$$\langle\frac{dE}{dt}\rangle_{tot} = \langle\frac{dE}{dt}\rangle_{e-ph} + k_3 n^2\left(E_g + E\right) \quad (16)$$

$$\frac{dn}{dt} = -k_{1n} - k_2 n^2 - k_3 n^3 \quad (17)$$

The letter n denotes the initial carrier density, the letter k_1 denotes the monomolecular recombination coefficient, the free carrier bimolecular recombination coefficient is denoted by the letter k_2, and the Auger recombination coefficient is denoted by the letter k_3. The latter two values are larger when the bandgaps are smaller and the carrier temperatures are increased [210]. According to the equation provided below, the energy loss rate caused by the interaction between electrons and phonons is represented by the first term, and the second term represents the Auger-heating contribution [199, 211].

2.6.3. Photocurrent of Hot Carriers Across a p-n Junction

HCs produced beyond the semiconductor band edge dissipate rapidly through interactions with phonons, resulting in significant energy losses [117, 212]. The Shockley-Queisser limit can be surpassed and power conversion efficiencies improved by making efficient use of hot carriers in photon-to-current conversion [198, 213-215]. A range of device architectures and materials has been investigated to harness hot carriers for the generation of photocurrent and photovoltage [216-218]. Steponas

Asmontas observed in 2001 that both theoretical and experimental investigations into the photoelectric characteristics of nonuniform semiconductors exposed to infrared laser light have been conducted. When the energy of the laser photon is less than the energy gap in the semiconductor, the photovoltage production in p-n and 1-h junctions is mainly caused by the heating of the crystal lattice and the photoemission of hot carriers across the potential barrier [219]. Free carrier heating causes an increase in forward current when a p-n junction is exposed to CO_2 laser light. Demonstrated in **Figure 10** is the relationship between the bias voltage supplied to the GaAs p-n junction and the photocurrent I_{ph}. It is observed that the photocurrent increases suddenly as the bias voltage "opens" the junction. The photocurrent's magnitude changes very little in response to changes in external voltage in the reverse bias region. An exponential rise of I_{ph} with U_0 is noted when the current injected into the hot carrier exceeds the capacitive current. When U_o gets higher, the photocurrent rises and then starts to drop. The photoresponse that results from free-carrier heating is known to be energy-band discontinuous in heterojunctions. Compared to GaAs homojunction, $GaAs/Al_xGa_{1-x}$ as a heterojunction with $x \leq 0.2$ is more appropriate for infrared detection. When the photon energy is below the Schottky barrier height, the metal-semiconductor Schottky contact photoresponse shows a highly nonlinear dependency on the excitation intensity.

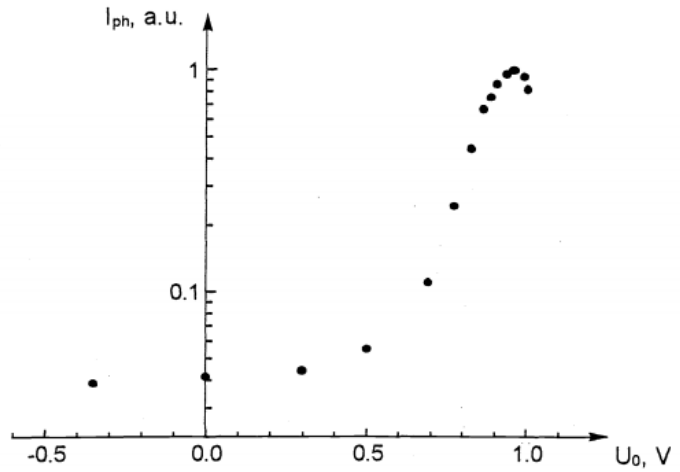

Figure 10. Photocurrent in GaAs p-n junction versus bias voltage. T0=300 K

While studying photovoltage formation across GaAs p-n junctions under intense laser illumination, the same group found that when the junction is illuminated with Nd: YAG laser radiation, the photovoltage is two-component,[211]

$$U = U_f + U_{ph}. \quad (18)$$

The photovoltage due to electron-hole pair generation (U_{ph}) and the thermoelectromotive force of the hot carrier (U_f) are defined. As shown in **Figure 11a**, the creation of electron-hole pairs leads to the generation of the thermoelectromotive force of HC and classical photovoltage [220, 221].

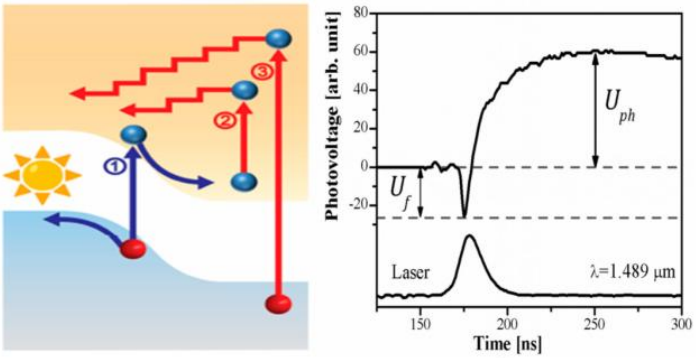

Figure 11. (a) A schematic depicting the process by which the thermoelectromotive force of HC and classical photovoltage are formed by the production of electron-hole pairs across the p-n junction: 1—the creation of an electron-hole pair by means of a photon with a wavelength equal to the bandgap; 2—the heating of free electrons; and 3—the creation of a hot hot electron and hole pair [220]. (b) Two-component photovoltage and the oscilloscope trace of a laser pulse [221].

The HC photocurrent has the opposite polarity to the generating photocurrent, as can be observed. By illuminating the p-n junction with a short laser pulse, HC photocurrent and generating photocurrent could be seen [222]. **Figure 11b** demonstrates the time-varying photovoltage curve across the Si p-n junction caused by 1.489 μm laser radiation [221]. The HC photovoltage U_f pulse's leading front follows the laser pulse's because the HC energy relaxation time is significantly shorter. When the current-voltage characteristic of a p-n junction is calculated using the electron temperature approximation, the total current flowing across the junction is expressed as [211]

$$j = \frac{eD_n n_p}{L_n}\left\{exp\left[\frac{eU}{kT_n} + \frac{eV_k}{kT_o}\left(1 - \frac{T_o}{T_n}\right)\right] - 1\right\} + \frac{eD_p P_n}{L_p}\left\{exp\left[\frac{eU}{kT_n} + \frac{eV_k}{kT_o}\left(1 - \frac{T_o}{T_n}\right)\right] - 1\right\} \quad (19)$$

Where e is the elementary electron charge, $D_{n,p}$ and $L_{n,p}$ is the diffusion coefficient and diffusion length for electrons and holes, respectively, n_p and p_n are the electron and hole densities in p- and n-regions, respectively, U is bias voltage, k is the Boltzmann constant, T_e and T_p are the temperatures of electron and hole, respectively, eVk is the potential barrier height of p-n junction, T is the lattice temperature. Open circuit cases when $j=0$, and with the equality, $T_e=T_p$ term electromotive force of HC is equal to

$$U_f = Vk\ (T_e/T - 1) \quad (20)$$

The term electromotive force of an HC is directly proportional to carrier heating and the potential barrier height of the p-n junction.

In an additional scenario, the photon energy approaches the forbidden energy gap. In **Figure 12,** we can see the time-varying photovoltage U across the GaAs p-n junction caused by pulses of the Nd: YAG laser. U has a single component, Uf, at low excitation levels, as illustrated. There is a correspondence between the polarity of U_f and the polarity of the thermoelectromotive force of hot carriers. As laser power increases, the photovoltaic form changes. The fast component U_f is linearly related to the laser's intensity at low excitation levels. However, U_{ph} takes center stage at higher laser radiation intensity (**Figure 12**).

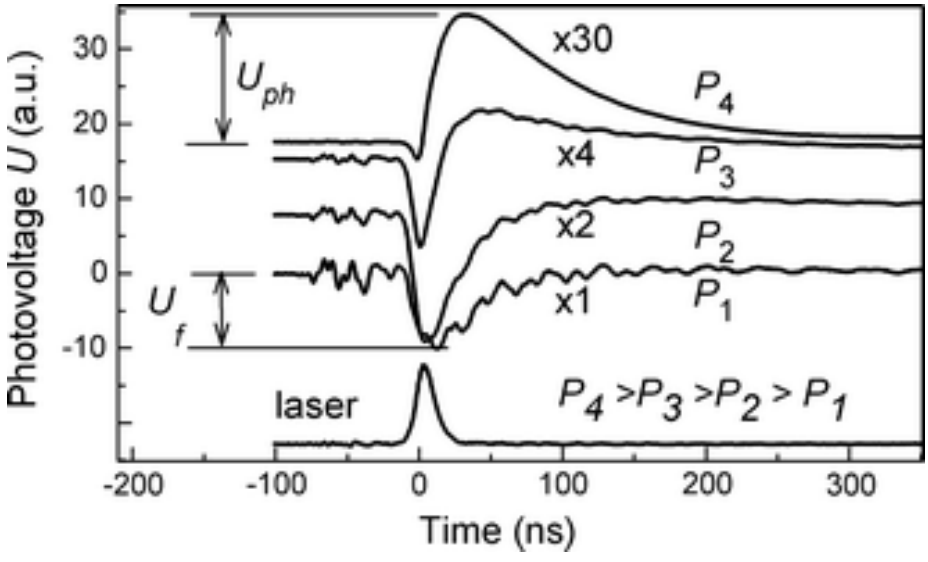

Figure 12. Photovoltage traces in p–n GaAs junction for different laser power P at λ = 1.064 μm

To evaluate the magnitudes of Uf and Uph independently, a time series analysis was performed on the photovoltage data. An approximation of the time dependence of the intensity of Nd: YAG laser pulses can be made as

$$I(t) = I_m(\frac{t}{\tau})^4 exp\left[4\left(1-\frac{t}{\tau}\right)\right] \quad (21)$$

I_m represents the peak intensity at time $t = \tau$, $I_m=I(\tau)$, and τ is the rise-time of the laser. The relaxation time of the heated carrier energy is shorter than τ.

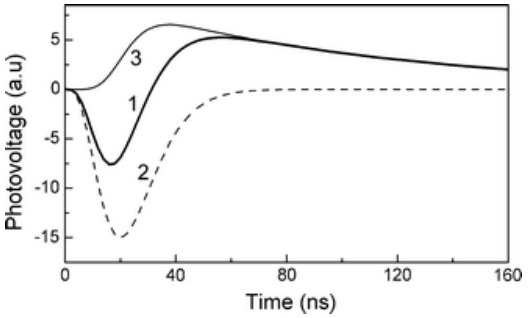

Figure 13. Experimental trace of photovoltage (curve 1) and calculated fast component U_f (2) and slow component U_{ph} (3).

Where

$$U_f = K_f.I(t) \quad (22)$$

The slow component of the photovoltage $U_{ph}(t)$, is found from

$$\frac{dU_{ph}(t)}{dt} = \frac{\bar{U}_{ph}-U_{ph}(t)}{\tau_{ph}} \quad (23)$$

Where $\bar{U}_{ph} = K_{ph}.I^2(t)$ and τ_{ph} is the characteristic decay time of $U_{ph.}$ The solution of the above equation gives

$$U_{ph}(t) = \frac{8!e^8 K_{ph} I_m^2 \tau}{a^9 \tau_{ph}}\left\{\exp\left(-\frac{t}{\tau_{ph}}\right) - \left[1+\sum_{n=1}^{8}\frac{(bt)^n}{n!}\right]\exp(-\frac{8t}{\tau})\right\} \quad (24)$$

Where $a = (8\tau_{ph}-\tau)/\tau_{ph}$ and $b = \frac{a}{\tau}$. The values of coefficient K_f and K_{ph} can be found from experimental magnitude of the photovoltage at $t = \tau$ and $t = \tau_m$ respectively. The t_m is defined by $\frac{dU_{ph}}{dt} = 0$ at the moment when $t=t_m$.

The computed curves can be shown in **Figure 13**. Both are in accordance with the experimental time trace. The components of the photovoltage produced across the p-n junction that are dependent on the hot

carrier effect and the electron-hole pair formation were thus separated and determined by the aforementioned approximation.

2.7. Significance of TSC Structures

The commercial PV market is dominated by crystalline Si-based solar cell technology. This is because crystalline Silicon is robust in terms of manufacturing technology, product reliability, and low manufacturing costs. Manufacturing costs have decreased significantly over the last decade, contributing to the exponential growth in global installations. Due to variations in bandgap values, the efficiency of various semiconductor materials will vary. Because TSCs are composed of stacked layers, it is pretty easy to comprehend them. These layers include bandgaps that can be adjusted, and their arrangement is designed to minimize the losses associated with single-junction cells. Additionally, increasing the number of connections in the device may result in a reduction in absorption loss while simultaneously improving the device's overall spectral ability. It is also possible for the thickness of these layers to significantly impact the performance of the TSC. Additionally, each sub-cell must have a current match. TSCs' efficiency is higher than that of individual cells because they utilize semiconductors with varying band gaps. This is because a particular perovskite compound can effectively use the visible component of sunlight, creating this potent combination, and the Tandem cell uses the solar spectrum more efficiently overall. In contrast, traditional Si solar cells mainly convert the infrared component of light into electrical energy [223]. To achieve significantly larger PCEs by effectively exploiting the solar spectrum in individual cells, TSCs were proposed as early as 1955 [224]. A TSC is constructed from several materials, including Si (monocrystalline, polycrystalline, and amorphous), perovskite, polymer, dye-sensitized solar cells, and quantum dot solar cells. Using TSCs as two-terminal, three-terminal, or even four-terminal systems is possible. Circuits in series or parallel are used to connect the electrical components of the TSC [225-227]. Because of their large theoretical PCEs, TSCs have been the subject of extensive research ever since. In 1979, using an epitaxy process in conjunction with the epitaxial tunnel junction (ETJ), a regularly utilized methodology, Bedair et al. created the first monolithically integrated AlGaAs/GaAs 2J TSC [228, 229]. Narrow-bandgap (~1.2 eV) and wide-bandgap (~1.7−1.9 eV) layers are the components that make up the tandem device architecture. These layers can surpass the single junction device's SQ (Shockley-Queisser) limit. Additionally, they can reduce losses, such as

thermalization loss, and ensure that the solar spectrum is utilized appropriately. The formation of effective TSCs, which offers the prospect of surpassing the fundamental Shockley-Queisser limit on the efficiency of a single junction solar cell, is typically crucial [230]. In addition to being referred to as third-generation PVs, perovskite is sometimes considered an artificial material. It is also one of the most promising emerging thin-film PV technologies. When it comes to tandem devices based on perovskites, those with compositionally maintained bandgaps are widely used. Each of these perovskites possesses a narrow bandgap of less than 1.35 eV and a wide bandgap greater than 1.55 eV. The characteristics of hybrid perovskites include a direct bandgap, high optical absorption, high tolerance for defects, extended carrier lifetimes and diffusion lengths, low exciton binding energies, and harmless grain boundaries. Hybrid perovskites also have a high degree of tolerance for defects [231, 232]. Materials made of perovskite have outstanding optoelectronic capabilities because of their unique electronic structure. This structure is also responsible for the excessive V_{oc} and efficiency of PSCs. The bandgap of the perovskite absorber could be accurately controlled to a certain level by using combinations of A-site cations (such as MA, FA, Cs, and rubidium), B-site cations (such as lead and tin), and X-site anions (such as iodide, bromine, and chloride). B-site cations include lead and tin. Using this bandgap-engineering method, it is possible to fabricate subcells that fill the bandgap [163, 233]. All perovskite TSCs have recently attracted attention due to their quickly improving performances.

When it comes to tandem devices based on perovskites, those with compositionally maintained bandgaps are widely used. Each of these perovskites possesses a narrow bandgap of less than 1.35 eV and a wide bandgap of greater than 1.55 eV. All of the characteristics of hybrid perovskites are as follows: they have a direct bandgap, they have a high degree of optical absorption, they have a balanced and small active area for both electrons and holes, they have a high degree of tolerance for defects, they have extended carrier lifetimes and diffusion lengths, they have low exciton binding energies, and they have completely harmless grain boundaries [231, 232]. The remarkable optoelectronic characteristics of materials made of perovskite are due to the unique electronic structure of these materials, which also contributes to the high Voc and efficiency of PSCs. The Bandgap of the perovskite absorber may be accurately controlled to a specific level by using combinations of A-site cations (such as MA, FA, cesium, and rubidium), B-site cations (such as lead and tin), and X-site anions (such as iodide, bromine, and chloride). B-site cations include lead

and tin. Through the use of this bandgap-engineering technique, it is possible to construct subcells that fill up the bandgap [233, 234].

2.7.1. Wide-band gap for Perovskite Top Cells

The crystal structure of metal halide perovskite (MHP) is represented by the notation ABX_3, which is the standard symbol. The capacity of A-site cations to generate lattice distortion in MHP is responsible for their impact on the bandgap. This distortion affects the bond length and angle of the B–X sites, ultimately influencing the bandgap frequency. Because B-site cations connect angles within the BX_6 octahedron, the bandgap reduces as the angle increases. The ionic radius of the X-site halogen anions was increased, and the valence level of the B–X bonds was decreased, which resulted in a reduction of the band gap. The bandgap in ABX_3 can be fine-tuned through the use of compositional engineering, which involves the incorporation of MA, FA, cesium (Cs), and rubidium (Rb) as A-site cations, lead (Pb), tin (Sn), and germanium (Ge) as B site cations, and iodine (I), bromine (Br), and chlorine (Cl) as the X site anion [119]. It is possible to change the bandgap of MHPs from the infrared region (i.e., 1.1 eV) to the UV region (close to 3.0 eV). This is demonstrated by the fact that MHPs can provide considerable flexibility when combined with NB cells. Due to the processing temperature, which is lower than 150°C, MHPs enable the construction of monolithic structures without damaging the bottom cell. Additional benefits include shallow trap sites, considerable carrier diffusion lengths, high dielectric constants, low exciton binding energies, and high absorption coefficients. Further advantages include these characteristics [235]. The use of $MAPbI_3$ perovskite may have influenced the development of TSCs based on perovskites. This is indeed a possibility. The $MAPbI_3$ molecule, on the other hand, undergoes a chain reaction that involves chemical reactions, phase transitions, phase segregation, and other forms of degradation when exposed to atmospheric variables such as oxygen, heat, light, and moisture. Bandgap in $MAPbBr_{3-x}I_x$ could be regulated chemically within the range of 1.55 to 2.3 eV, with x moving from iodide to bromide. This was possible because of the presence of chlorine. Using a tandem arrangement, top subcells can obtain bandgaps ranging from 1.70 to 1.85 eV. However, it has been demonstrated that when the bromide concentration is very high, light instability leads to photo-induced halide segregation in $MAPbBr_{3-x}I_x$. This, in turn, decreases the voltage that can be achieved, as well as the functionality and dependability of mixed-halide perovskite devices [119, 236].

2.7.2. Narrow-band gap for Perovskite Bottom Cells

All-perovskite tandems offer the advantages of low-temperature production, low-cost manufacturing, and the possibility of both subcells in the structure having light and flexible form factors. This allows for high efficiency to be attained while maintaining the advantages. The perovskite bandgap can be reduced through a feasible method that involves substituting tin for lead. Perovskites based on tin have a shorter optical bandgap compared to perovskites based on lead, but the isoelectronic arrangement of the two types of perovskites is the same [237]. It has been discovered that SnPb-alloyed perovskites are the only approach that is capable of achieving an Eg as low as 1.2 eV. This enables the utilization of the solar spectrum to be maximized in conjunction with wide-bandgap perovskite, ultimately resulting in all-perovskite tandem cells that are exceptionally efficient. Perovskite materials have the narrowest bandgap due to the bowing effect of the bandgap, which occurs when the ratio of Sn to perovskite is 60% [238]. Perovskites that include Sn, on the other hand, have properties that are characteristic of semiconductors. These characteristics include a substantial intrinsic carrier density resulting from the spontaneous oxidation of Sn_2^+ ions and a short carrier lifetime induced by a significant trap density [239]. Modifying the radius of the A-site ion is another method that can be utilized to affect the bandgap of the perovskite. This can be achieved by adjusting the lattice structure. In addition, the substitution of MA^+ affects the bandgap formed by FA^+ and Cs^+ at the A-site. The introduction of FA^+ at the A-site can result in the production of NB perovskite. This is likely because FA^+ possesses a slightly larger ionic radius than MA^+ [101, 240].

2.7.3. TSC Integration

A promising concept that has garnered significant attention from the PV community is the combination of a wide-bandgap perovskite with established low-bandgap materials, such as Si and CIGS, to construct TSCs [241-243]. However, the incorporation of perovskite and Si materials into TSCs has the potential to provide an additional boost in PV efficiency with a minimal increase in cost. This is even though the success of this material is primarily due to its extremely high absorption coefficient, which makes it suitable for a single-absorber configuration. It has previously been proven that the tandem design is capable of exceeding the theoretical efficiency limit of Si solar cell technology. This tandem configuration leverages the broad absorption spectrum of Si, which can be combined with the

customizable absorption spectrum of the PSC [244, 245]. One notable characteristic is the high absorption coefficient, which is approximately 5.7×10^4 cm^{-1} at a wavelength of 600 nm. For several reasons, the high absorption coefficient of perovskite materials indicates that they can absorb a significant amount of sunlight in a highly effective manner, even when in the form of thin films. The first benefit is that it helps PSCs achieve a high level of efficiency. To increase the total PCE of the cell, it is necessary to have the capability of absorbing a substantial amount of light with a relatively thin layer of material. This allows for a greater number of photons to be converted into electrical energy. Second, the manufacturing of solar cells that are both lightweight and flexible is made possible by the high absorption coefficient [246]. Considering this aspect, new opportunities for incorporating solar cells become available. Their transformative potential in the field of renewable energy is demonstrated by the breakthroughs made in perovskite TSCs. These advancements have not only led to record efficiencies but have also paved the way for future applications, such as water splitting. Incorporating perovskites with other materials, such as Si, significantly enhances the potential of these cells to achieve even better efficiencies and a wider range of applications through their integration. It has also been established that the inorganic large-bandgap $CsPbI_2Br$ perovskite is an ideal option for integration with organic subcells. This is because it possesses exceptional UV and high thermal stability [247].

2.7.4. Stability Issues and Solutions for Perovskite Tandem Structures

The standard test prescribed by the International Electrotechnical Commission (IEC) stipulates that a PV module must be able to function continuously for 25 years in outdoor circumstances while retaining more than 80% of its initial η. Perovskite–Si TSC is governed by IEC standards, which are the industry's bare minimum standard [248]. Perovskite-based TSCs face a significant challenge in terms of their commercial applicability due to their inherent instability. Due to the high sensitivity of these materials to heat, light, and humidity, the stability is primarily restricted by the perovskite sub-cells. These sub-cells have stabilization problems that are mainly associated with the perovskite absorber layer, the Recombination layer, charge extraction layers (ETL/HTL), and contact electrodes [249]. Additionally, the compatibility of perovskite with ETL/HTL and contact electrodes is a factor that influences the stability of the device. Several techniques, including device encapsulation, have been implemented to mitigate the impact of degrading factors and enhance the operational

stability of perovskite-based TSCs. The power output that is achieved can undergo both reversible and irreversible alterations as a consequence of ion migration that occurs within the perovskite. Within the context of the International Summit on Organic Stability (ISOS), a scenario that is comparable to this one was discovered regarding the stability of organic PVs. This unique behavior presents difficulties for evaluation using traditional IEC standards. A declaration of the introduction of one-of-a-kind tests that are pertinent to perovskite–Si TSC is included in the consensus statement of ISOS. To determine whether or not perovskite–Si tandem combinations are viable for commercial use, the new IEC standards anticipate the introduction of ISOS test techniques. It is the volatile organic cations MA^+ that cause perovskite to be unstable. To enhance the phase stability of $MAPbI_3$, partial substitution of FA^+ and Cs^+ at the A site was performed, and the device was encapsulated in cost-effective polymers to prevent oxygen and moisture ingress [250, 251]. As a result of prolonged lifetimes of the photoexcited species and robust contacts between MA^+ and the inorganic cage, mixed-cation perovskite ($MA_xFA_{1-x}PbI_3$) exhibits higher thermal stability and improved device performance when compared to single-cation perovskite-based devices. The thermal, structural, and photostability of the device were all improved as a result of incorporating Cs^+ ions into MA^+ and FA^+-based perovskite [252, 253]. Both halide phase segregation and tunneling of photocarriers into I-rich regions, which act as traps and reduce the V_{oc} of the cell, are problems that occur in mixed-halide perovskite compounds when they are exposed to light [254, 255]. Mixed perovskite also suffers from photo-instability and halide segregation, both of which are results of ionic migration. As an alternative to introducing an interlayer between the perovskite and ETL/HTL, the flaws can be passivated by combining additive chemicals in the perovskite precursor solutions or using an anti-solvent [256].

The study on enhancing the stability of perovskite-based tandems is still in its early stages, despite stability tests for perovskite-based tandems being routinely undertaken in the majority of works that focus on improving efficiency. Additionally, the progress made regarding the stability of perovskite-based tandems is not as far along as that of perovskite single-junction batteries. To determine whether PSCs are stable over an extended period, specific stability tests can be utilized. Very few stability assessments have been conducted for tandem-configuration solar cells, which are governed by the IEC or regimes that are similar to the IEC. The rationale related to this situation is that stability tests are representative of the

properties of the single-joint solar cell. There is a significant difference between the subcells paired in tandem design and single-junction solar cells, as their transient behavior and stability, which are peculiar to the tandem configuration, have not been fully captured. In 2018, the concept of light soaking for tandem stability was introduced for a 2T perovskite/Si TSC that was placed on top of a fully textured Si heterojunction (HJT) solar bottom cell that had a p–i–n grid layout. On the other hand, the 24% PCE unencapsulated perovskite/Si TSC maintained 90% of its pristine performance after being exposed to 0.7 suns at maximum power point (MPP) for 61 hours in an ambient atmosphere [257]. Similarly, this highly efficient solar cell was characterized by the integration of a self-assembled monolayer with a methyl group substitution (Me-4PACz) as the hole-transporting layer (HTL). The TSC, with a PCE of 29%, emerged as the most notable aspect of this solar cell. After 300 hours of exposure to one sun at 25°C and temperatures ranging from 30% to 40% relative humidity, the created device demonstrated improved light-soaking stability, while its counterpart, which was not encased, maintained its 95% performance [179]. To evaluate the performance of single-junction solar cells with p–i–n and n–i–p designs, damp-heat experiments were conducted [258]. On the other hand, claims of a comparable nature for the tandem solar setup are uncommon. A perovskite/Si TSC with 28.2% efficiency maintained its performance for up to 87% after being subjected to a 500-hour damp-heat assessment. The incorporation of carbazole molecules as a perovskite additive, the enhancement of the perovskite bulk quality, and the passivation of deep charge traps were the rationales behind this excellent performance [259]. After being exposed to moist heat for a period of 1,000 hours, the incorporation of a magnesium fluoride (MgF_x) layer with a thickness of 1 nanometer between the perovskite and the ETL can result in a 2T perovskite/Si TSC that is 29.3% efficient and maintains a PCE of 95% [260]. In addition to posing difficulties for the encapsulation method, a damp-heat test has the potential to reduce the intrinsic cell stability.

2.7.5. Power Losses in Perovskite TSCs

When it comes to designing and manufacturing tandem devices, power loss is a crucial factor to consider. It is essential to have a comprehensive understanding of the factors that influence power loss to construct incredibly efficient devices. In addition to the losses caused by electrical current, a significant portion of the overall power losses is attributed to reflection, parasitic absorption, and other optical loss mechanisms. The phenomenon of

parasitic absorption losses occurs in tandem device configurations when photons are absorbed in layers that do not create photocurrent. During operation, monolithic TSCs experience substantial electrical or resistive losses, resulting in current mismatch and a decrease in efficiency. For numerous reasons, the utilization of transparent electrodes was advantageous to both the 2T and 4T c–Si/perovskite tandems. To facilitate the transmission of a substantial amount of light across a broad spectrum (UV-vis and NIR spectral ranges), the T transparent electrodes used in the top PSC and bottom Si subcells must possess low sheet resistance and a high level of transparency. A parasitic absorption loss was produced as a result of the optical absorption that occurred at the TCO electrode, charge transport, and recombination layers. Photons that are absorbed within these layers do not contribute in any way to the photocurrent that is flowing through the system. As a consequence, there is a decrease in absorption when parasitic components are present. Due to this, the requirement for three transparent electrodes presents a considerable obstacle to the development of four-terminal tandem architectures. It is believed that the free-carrier absorption of the transparent electrodes is responsible for the observable rise in parasitic absorption losses in the wavelength range of 850–1200 nm. Layers with a thickness of more than 100 nanometers are especially susceptible to the effects of this phenomenon [261].

In both the 2T and 4T c–Si/per tandem arrangements, it is a provable fact that light must travel through the upper perovskite subcell before it can reach the lower Si subcell. This is the case in both configurations. As a consequence of this, it is desirable to enhance the intensity of the near-infrared light that is transferred without any loss from the top perovskite cell to the bottom Si cell. Through reflection loss brought on by a mismatch in the refractive index (n) between the several layers, TSCs experience a significant decrease in the amount of power that they can produce. This holds especially true for light that has a wavelength that is quite long. It is also important to note that the phenomenon of reflection losses can be attributed to changes in the refractive index at the interface of the front surface (which includes the front electrode and free air) as well as the interfaces between the upper and lower subcell layer stacks. This is something that should be taken into consideration. A significant portion of the reflection loss can be attributed to the mismatch in refractive index that exists between the transparent electrode, the air (n = 1), and the glass (n = 1.52) compared to the transparent electrode. Because a portion of the light is reflected away from the layers with a higher refractive index, significant

losses occur at the front electrode, ultimately resulting in no contribution to the photocurrent [262, 263]. By modifying the refractive index of the TCO layers, it is feasible to reduce the number of reflection losses that occur; it has been reported that the nc–SiOx: H layers that are present in thin-film Si TSCs were replaced with TCOs that had n values in the range of 1.8 to 2 [264]. Concerning the red and infrared spectral bands, the findings indicate a decrease in the amount of parasitic absorption and reflection losses. Through the utilization of the nc–SiO: H layer as an interference/recombination junction between perovskite/Si monolithic TSCs, the photogenerated current of the Si bottom cell was also enhanced [257]. Additionally, there is the possibility of reducing the impact of the refractive index mismatch that exists within the TSCs. Consider, for example, the use of a multilayer stack in a tandem design that exhibits spectrally selective transmission and reflection behavior. This allowed for the J_{SC} to be boosted by 0.82 mA cm^{-2}, which is a substantial amount [265]. To minimize reflection losses, it is highly recommended to use anti-reflective coatings. When it comes to anti-reflective coatings, lithium fluoride (LiF) and magnesium fluoride (MgF_2) are both widely used due to their high transparency and low refractive index. Albrecht and colleagues were able to reduce reflection losses at the air/ITO contact by thermal evaporating a layer of LiF onto a monolithic c-Si/per thin-film solar cell [266]. The photo-generated current, as measured in the bottom Si subcell, increased by 1.5 mA/cm^2 when a LiF layer was added as an anti-reflective coating. Additionally, anti-reflective coatings facilitated the display of closely matched currents in the two subcells. The current values for the bottom Si subcell and top perovskite were 14.0 and 14.7 mA/cm^2, respectively, under AM 1.5G spectra. The specialized development of wide-band antireflection coatings for thin-film technologies is expected to be the subject of extensive research in the near future, much like the case of amorphous Si [267].

2.7.6. Hot Carriers in Perovskite TSCs

Of fundamental physical interest, as well as of practical device-engineering relevance, in the context of perovskite TSCs, are hot carriers: charge carriers with excessive kinetic energy directly after photoexcitation, which therefore act as a source of potential loss, but also enable one to overcome conventional efficiency limits. In traditional PV materials, such as Si, high-energy photons (whose energy greatly exceeds the bandgap) create hot electrons and holes, which, however, very rapidly (on timescales of sub-picoseconds) lose their excess energy to carrier-phonon interactions before

their energy can be helpful to, resulting in significant thermalization losses that directly limit the PCE by the ShockleyQueisser (SQ) detailed balance limit [117, 268]. In perovskite materials, by contrast, hot carrier cooling is remarkably slow (tens to hundreds of picoseconds) owing to a combination of effects including strong electron-phonon coupling, large polaron formation, the hot phonon bottleneck, and the relatively soft lattice, so that following photon absorption, HC dwell at high energies longer than in most other semiconductors [190, 269]. In the perovskite-based TSC architecture, where at least two absorber layers of different bandgaps are stacked, the control of HC is even more decisive: the top cell, made of wide-bandgap perovskite, absorbs photons of higher energy and, therefore, a significant amount of HC are generated in this layer, whereas the bottom cell (which may be Si or CIGS or a low-bandgap perovskite) only absorbs lower-energy photons and, therefore, a lesser amount of HC [268, 270]. A conventional two-terminal perovskite TSC will have a wide bandgap (~1.7-1.8 eV) top sub-cell and a narrow bandgap (~1.1-1.3 eV perovskite or ~1.12 eV Si) bottom sub-cell [271, 272]. In this configuration, it is possible to perform spectral splitting in which the high-energy photons are absorbed in the top cell, and the lower-energy photons that are transmitted are absorbed in the bottom cell, converting as much energy as possible and minimizing the loss due to thermalization [266].

The absorption of photons in the upper cells of perovskite TSCs is a fundamentally important process that enables the architecture to exceed the single-junction efficiency limits, opening the path to next-generation solar energy conversion technologies. In a conventional perovskite tandem cell, a wide-bandgap perovskite material is used to make the top cell. The absorption of photons and hot carrier behavior in the top cells of perovskite TSCs is key to the previously unachieved performance of the next-generation PVs, owing to the combination of the extraordinary optical quality of perovskite materials and the unusual hot carrier physics. In principle, the tandem geometry can be used to split the spectrum, allowing each sub-cell to be operated near its bandgap and minimizing losses due to thermalization. HC created by photons near the band gap of the bottom cell is less energetic, however, and their effects are, therefore, more subtle than in the top cell. The perovskite top cell acts as a spectral filter to the bottom cell, where photons with energies above the bandgap are absorbed in the top cell, whereas the sub-bandgap photons can pass through the top cell and reach the bottom cell. This filtering has an effect on the carrier population in the bottom cell, both in terms of flux and energetically. In complete

absorption or non-radiative recombination in the top cell, there is no possibility of creating so-called HCs with excess energy in the bottom cell.

3. MATERIALS AND METHODS

When considering the development of new materials for PSCs and the recent advancements in understanding the working principles of perovskite devices, it is noteworthy that these developments are occurring concurrently. Both the architecture of the PSC as a whole and the selection of materials utilized have a significant impact on the electrical and optical properties of the device produced as a result. It is also possible to optimize the characteristics of perovskites by modifying their elemental composition. In terms of optical absorption, bandgap, stability, and defect tolerance, the precise selection and combination of materials are crucial. As an example, perovskites can have their thermal and moisture stability greatly enhanced by using mixed cations and halides. This also allows for the bandgap to be fine-tuned for maximum sunlight absorption. There are five main types of materials used in PSCs: the metal contact material, the light-harvesting perovskite material, the ETL, the HTL, and the TCO layer.

3.1. Material Selection

The precursor solution has been utilized to produce highly efficient PSCs. As indicated before, the device architecture and the type of electron and HTM also have a significant impact on the PCEs of PSCs. This implies that the surface morphology, crystallinity, defect concentration, grain growth, and other properties of the perovskite layer are significantly impacted by the conditions at which it is solidified from the precursor solution. This is likely because the physical properties of the final perovskite film are predicted to be influenced by the rapid development of the crystalline perovskite film upon solvent removal from the precursor solution. The active layer of these devices is a perovskite-structured absorber, most often a hybrid organic-inorganic metal halide, methylammonium lead iodide ($MAPbI_3$), formamidinium lead iodide ($FAPbI_3$), or a mixed-halide and mixed-cation version thereof. The perovskite composition directly determines the values of critical parameters such as the bandgap, crystallinity, and stability.

An example is the introduction of various cations, such as cesium (Cs^+) or rubidium (Rb^+), into the perovskite structure, which improves thermal stability and resistance to moisture, thereby increasing the device's operating

life. On a chemical level, the perovskite absorber is susceptible to environmental conditions, including moisture, oxygen, UV radiation, and high temperatures. The ultimate solution is to select suitable charge transport materials and encapsulation methods as well. The ETLs, often made of inorganic semiconductors such as titanium dioxide (TiO_2) or tin oxide (SnO_2), are chosen due to their high electron mobility, chemical inertness, and favorable energetic offset with the perovskite absorber. Chemical reactions at interfaces, however, need to be controlled because some ETL materials can catalyze degradation reactions when illuminated for prolonged periods or exposed to ambient air. HTLs are made of organic semiconductors, such as spiro-OMeTAD, PTAA, and PEDOT: PSS, due to their favorable band alignments, ease of manufacturing, and high electrical conductivity. Such materials must be chemically doped or added to become conductive, and this must be controlled precisely to prevent instability and degradation over time. Electrode materials must be chemically compatible with the layers beneath them, resistant to corrosion, and impervious to environmental barriers. Gold, silver, and carbon electrodes are commonly used due to their high conductivity, chemical stability, and relatively low price. Conclusively, a detailed interaction between meticulously tailored materials, their inherent chemical properties, and processing parameters has a profound influence on the performance, stability, and commercial applicability of PSCs. When exposed to intense light sources, such as laser pulses, perovskite solar cells can experience a decrease in performance due to the photobleaching phenomenon. Reduced light absorption, charge separation, and overall power conversion efficiency can result from photobleaching, the loss of a material's light-absorbing capabilities due to prolonged or intense exposure to light. The perovskite material can undergo structural changes during photobleaching, which can make the device less stable and more prone to degradation [273-275].

Within the frame of this project, we have opted to select Cs-based triple-cation perovskite compositions. The careful design of two exemplary Cs-based triple-cation perovskite compositions of $Cs_x(FA_{0.83}MA_{0.17})_{(1-x)}Pb(I_{0.83}\ Br_{0.17})_3$ and its Sn-modified counterpart $Cs_x(FA_{0.83}\ MA_{0.17})_{(1-x)}Pb_{0.8}Sn_{0.2}(I_{0.83}\ Br_{0.17}\ )_3$ The first Pb-based composition $Cs_x(FA_{0.83}\ MA_{0.17})_{(1-x)}Pb(I_{0.83}\ Br_{0.17})_3$ is tactically selected because it exhibits better stability, optimized PV behavior and optimal balance of charge-carrier mobility and recombination dynamics. The Cs^+ ions are incorporated into this formulation to enhance phase stability, which helps prevent undesired phase transitions that are prevalent in purely organic perovskite analogues,

including pure $FAPbI_3$ and $MAPbI_3$. The addition of Cs^+ alleviates the problem of thermal and moisture sensitivity, leading to constant and uniform crystallization and a significant decrease in defect densities at the grain boundaries. What makes its novelty even greater is the addition of Sn into the second composition, $Cs_x(FA_{0.83}MA_{0.17})_{(1-x)}Pb_{0.8}Sn_{0.2}(I_{0.83}\ Br_{0.17}\ )_3$. This highly monitored partial replacement Sn offers a sophisticated approach to engineering the inherent material properties, particularly the optical bandgap and electronic transport properties. Due to the selective incorporation of tin, the bandgap decreases, allowing photons to be absorbed within a specific range. In turn, this can lead to higher short-circuit current densities (J_{SC}) and higher total PCE [238]. Moreover, a tin substitution leads to an extraordinary enhancement in charge-carrier mobilities. The latter is explained by the fact that the intrinsic conductivity of the material is enhanced, as well as the carrier diffusion lengths are extended due to the changed lattice structures and decreased effective mass of the charge carriers [276]. The direct comparative analysis of Pb-only and Pb-Sn hybrid perovskite films, each including Cs^+, $FA^{+,}$ and MA^+, is critically important as it provides a powerful experimental platform to determine and isolate the effect of Sn doping unambiguously. The comparison elucidates specific structural, optical, and electronic modifications, including changes in lattice parameters, stress relaxations, and defect energetics, resulting from the partial replacement of Sn_2^+ ions in Pb_2^+ lattice sites. These extensive and detailed insights are invaluable in guiding focused efforts to improve the optoelectronic properties of perovskites, the nature of defect passivation processes, and in optimizing device performance [277, 278]. Overall, these carefully chosen perovskite compositions provide considerable scientific novelty in methodically investigating how a controlled Sn addition in triple-cation perovskites influences the PV activity, stability, and sustainability, which is of significant effect. This comparative analysis will form a crucial basis for the fundamental interpretation and practical optimization of mixed Pb-Sn perovskite materials, which lay the foundation for future developments aimed at reducing lead content, improving environmental sustainability, and enhancing the technological maturity of PSCs for commercial and industrial use.

3.2. Description of Fabrication Techniques and Equipment Utilized in the Project

3.2.1. Spray Pyrolysis for tio$_2$ Layers

In the 1980s, a significant approach for synthesizing thin film materials from precursor solutions was spray pyrolysis [279]. This technology has proven to be an effective way to deposit functional nanostructures and homogenous composites on a large scale. After nearly four decades of research and development, spray pyrolysis is now widely used to make electrode materials, multicomponent ceramics, and semiconductor thin films. The development of a thin film is a process that begins with the atomization of a precursor solution and continues with the deposition of the solution onto a heated substrate. This technology can provide precise control over film thickness and shape in the case of metal oxide ETLs for PSCs. These are two parameters that are crucial for the device's performance. Spray pyrolysis has been utilized for PSCs; however, its application has been limited to this point. This is because it requires high substrate temperatures (450°C), which are necessary to create dense layers of titanium dioxide. There is still a significant obstacle to overcome, which is lowering the temperature at which the deposition takes place. This involves identifying a precursor that produces a dense and effective ETM layer at temperatures below 450°C and determining whether it is possible to deposit TiO_2 on flexible substrates. Spray pyrolysis offers several advantages despite being a relatively straightforward process. Simply adding the material to the aqueous spray precursor solution is all that is required to dope films with any material in any quantity. This makes it a convenient and straightforward method. **Figure 14** illustrates spray pyrolysis.

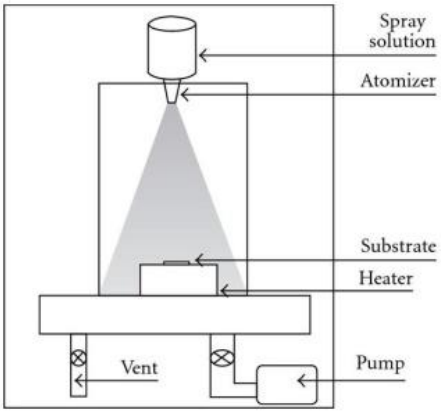

Figure 14. Schematic diagram of the spray pyrolysis system.

It is essential to note that, unlike vacuum deposition procedures, Spray Pyrolysis does not require the use of high-quality targets and substrates. This is a significant advantage that could be beneficial if the approach is scaled up for use in solar cell manufacturers. For this reason, the rate of deposition and the thickness of the thin films may be regulated within the acceptable dynamic spray limit. This eliminates the primary drawbacks of chemical methods, such as sol-gel, which restrict the thickness of the thin films. Spray pyrolysis can be performed at temperatures ranging from 200 to 500°C. When it comes to the dimensions of the substrate and its surface profile, there are no constraints. Dissolving metal salts, such as titanium (IV) isopropoxide, tin (IV) chloride, or zinc nitrate, in a suitable solvent like water or ethanol is the first Step in preparing the precursor solution for spray pyrolysis. This solution is then used to perform the spray pyrolysis reactions. Following the formation of the metal oxide coating, the solution is atomized into droplets employing an atomizer and then sprayed onto a heated substrate. This process is followed by a series of chemical reactions, including hydrolysis and pyrolysis, which are carried out. In the first Step of the process, the produced precursor solution is atomized by a nebulizer into an aerosol spray consisting of droplets. An aerosol is a mixture of air and a solution. After that, the nebulized spray droplets are introduced into the reaction chamber using a carrier gas. Each practical droplet functions as a microreaction, undergoing a series of physicochemical reactions. These reactions include solvent evaporation, precipitation, aeration, and decomposition.

3.2.2. Spin Coating Process

The spin-coating process is another relatively easy technique that, to some extent, resembles solution casting. It is likewise an easy procedure. On a substrate, a mixture of polymer and inorganic salt solution is drop-cast using this technique. This is in contrast to the traditional approach of casting the film directly onto the substrate. Spin coating is a batch process that involves applying centrifugal force to distribute a liquid film on a rotating substrate. After that, the solution is applied to the substrate in tiny increments to ensure that the entire area is covered. During the procedure, the coating solution is applied to the substrate's surface, and centrifugal force causes the solution to spread into a thin film. The solvent evaporates quickly, resulting in a uniform coating layer across the substrate. After being spun at

the optimal speed, the film is then annealed at the optimal temperature. As a result of the thickness of the perovskite thin film, the ideal temperature shifts based on the rotating velocity of the spin coater, which, in turn, changes the optimum temperature. When it comes to thin film annealing, the temperatures and timeframes required might vary anywhere from 60ºC to 200ºC. Three experimental parameters can be used to determine the thickness of the layer. These parameters are the rate at which the solvent dissipates, the velocity of the spinning substrate (spin rate), and the viscosity of the coating solution. To control the creation of the layer, it is necessary to consider factors such as the volume of the precursor, the rotating speed, the rotational time, and the concentration of the solution. Here is an easy explanation of the spin-coating process that predicts the thickness of the film based on an array of different physical parameters: [280, 281]

$$h = \frac{h_o}{(1+\frac{4\omega^2 h_0^2 t}{3\eta})^{\frac{1}{2}}} \qquad (25)$$

The initial film thickness is denoted by h_0, the spin rate is denoted by ω, and the viscosity is denoted by η. However, the varied operating circumstances do not necessarily satisfy the assumption. In principle, it is hypothesized that a precursor solution with lower viscosity for spin coating will result in a thinner, more uniform layer. A significant drawback of this approach is that it does not permit the use of highly viscous liquids. Similarly, it is not suitable for gel mixtures, as the droplet of the mixture cannot be spread into a thin film by the rotating process.

The spin-coating process can be further divided into two sections: one-step and two-step. Spin coating a perovskite precursor solution onto a pre-treated TCO substrate is the first stage in the one-step deposition procedure. Annealing is then performed to create the perovskite active layer. This is the deposition process that is most commonly employed because of its ease of use and low production cost for small, lab-based PSCs. However, it is not suited for the fabrication of large-surface-area devices. When using the one-step deposition technique, the ionic strength of the solution and post-annealing both contribute to an improvement in the production of perovskite crystals. The two-step approach involves the synthesis of two distinct precursors in separate steps, which results in the deposition of a film. N, N-Dimethylformamide (DMF) and isopropanol are the solvents used to dissolve halide organic salts and lead halide salts, respectively. After that, the lead halide solution is annealed after being spin-coated on the ETL/HTL to complete the process. Following this Step, the MAI solution is spin-coated onto a surface made of lead halide, and then it is annealed through

interdiffusion to obtain the perovskite films. When compared to the approach that requires only one Step, this method simplifies control over the process. When it comes to controlling crystallization and defining the quality of the perovskite film, the solvent used in the spin-coating process plays a significant role. At the same time, crystallization of the precursor itself or the solidification of a liquid can occur, depending on conditions such as the precursor concentration, synthesis temperature, and elapsed time. The crystallization rate is sensitive to changes in the solvent used, which significantly impacts the surface quality of the film. The spin-coating method is also sensitive to experimental conditions, including the composition of the precursor, the solution concentration, the annealing duration, and the annealing temperature. **Figure 15** depicts the spin-coating process. During the manufacturing process of perovskite solar cells, the deposited layers should be optimized to ensure high efficiencies and durability. Among the widely applied deposition methods, spin coating and spray pyrolysis techniques can be listed, along with their advantages and drawbacks. A majority of individuals also concur that spin coating is the most recommended technique for achieving superior perovskite layers, especially in laboratories and research stations. Although spray pyrolysis has the potential to be applied on a large scale in the future, spin coating is superior in terms of quality perovskite layers, particularly in terms of uniformity, crystal quality, and solar energy conversion. It then follows that the best method to use for research purposes and fabrication of high-performance perovskite solar cells is spin coating. With the evolution of manufacturing processes, additional advancements in spray pyrolysis could contribute towards filling the quality gap in terms of films; however, spin coating would still act as an ideal standard in perovskite layer deposition.

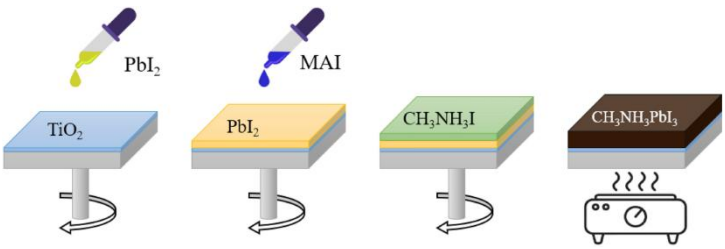

Figure 15. spin coating method for the preparation of the perovskite layer.

3.2.3. Low-pressure Oxygen Plasma Cleaning

Oxygen plasma cleaners, especially low-pressure models, are ubiquitous and essential instruments in state-of-the-art semiconductor processing and PV device fabrication. Specifically, the plasma cleaner offers the opportunity to control the cleaning conditions delicately, necessitating repeatable and dependable outcomes, which are of the utmost importance when dealing with fragile PSC applications. In this system, highly reactive oxygen particles (radicals and ions) are generated in a controlled vacuum, typically at a pressure of a few millitorr to a few hundred millitorr, allowing for controlled surface treatments. When layers of PSCs, e.g., ETLs such as TiO_2 or SnO_2, HTLs, or TCO substrates like FTO or indium tin oxide (ITO), are treated under the conditions of a plasma cleaner, the layers are treated to remove surface contaminants completely. Naturally occurring organic residues, hydrocarbons, water molecules, and other contaminants that inevitably adsorb onto surfaces during handling or storage can strongly degrade device performance, either by creating recombination centers or by preventing the uniform crystallization of the perovskite films. Such residues can be effectively oxidized and sublimed in a well-controlled, low-pressure plasma treatment process, thereby yielding ultra-clean and chemically homogeneous surfaces. It is a much-needed surface preparation protocol to improve the quality of film deposition. Additionally, the oxygen plasma produced in this apparatus causes surface activation via the formation of oxygen-rich functional groups (e.g., hydroxyl-OH and carbonyl-C=O groups) on the surfaces of substrates. The change improves hydrophilicity/wettability, which is essential in deposition techniques (such as spin-coating, blade-coating, and inkjet printing) of perovskite films. Enhanced wettability enables the homogeneous spreading of perovskite precursors, reduces pinhole formation, and facilitates homogeneous and reproducible crystallization. As a result, it can be expected that surfaces treated under plasma will produce perovskite layers of much better morphological uniformity, lower defect concentration, and improved grain boundaries. Through the deposition of surface adsorbates and the introduction of chemically stable, oxidized functional groups, plasma treatment significantly reduces moisture diffusion and the availability of reactivity sites for chemical degradation pathways, thereby hindering perovskite decomposition reactions. As a result, devices fabricated with such equipment exhibit significantly extended operating lifetimes and are more likely to retain their original performance parameters in long-stress

operational environments, as well as in the presence of environmental stresses (e.g., moisture, oxygen, and thermal) [282].

3.2.4. Ultrasonic Bath

The Elmasonic S40 H ultrasonic bath is a tool that utilizes high-frequency sound waves (typically around 37 kHz) propagating through an aqueous medium to form microscopic cavitation bubbles, which violently collapse, producing local high-pressure waves and turbulence. The cavitation process is found to be efficient in removing contaminants at the microscopic level, resulting in exceptionally clean and chemically homogeneous surfaces. This is a critical requirement for preparing quality PSCs. Substrates used in the fabrication of PSCs, such as glass substrates, TCOs (e.g., ITO, FTO), or ETL(e.g., TiO_2, SnO_2), can be thoroughly cleaned of particulate and organic contamination when treated in the Elmasonic S40 H ultrasonic bath.

Such contaminations frequently contain dust, residual organics from the fabrication procedures, and atmospheric hydrocarbons, which can deleteriously impact the subsequent coating and crystallization of perovskite films. The ultrasonic bath is an effective method for achieving acoustic cavitation, which easily breaks down weak physical forces between contaminants and substrates, thereby dislodging and dispersing them into the cleaning solution. The Elmasonic S40 H ultrasonic treatment effectively removes microscopic particulates and surface contaminants, highly benefiting the uniformity in the formation of perovskite films. The growth of perovskite crystals is highly susceptible to the cleanliness and morphology of the substrate; even slight contamination can alter the crystallization process, leading to the introduction of grain boundary defects and non-uniform grain sizes. Despite this, the well-cleaned substrates produced using this ultrasonic bath tend to yield perovskite films with more uniform grain sizes, fewer grain boundaries, and a more transparent crystal morphology. Lastly, the substrate surfaces cleaned in the Elmasonic S40 H ultrasonic bath provide an ideal surface on which other layer deposition, such as electron transport, hole transport, and perovskite absorber layers, can be performed. The enhanced cleanliness of the surfaces ensures more predictive and controlled interface interactions, which are crucial for sophisticated interface engineering schemes that minimize interfacial energy barriers.

3.2.5. Glove Box Environment Control

In this work, we have utilized an MBRAUN MB-10-G type glovebox, made by M. Inertgas-system GMBH, Germany, which is an advanced inert-gas-controlled environment glovebox specifically designed for precision handling and fabrication of sensitive materials. This glovebox is designed to maintain extremely low levels of oxygen (O_2) and moisture (H_2O), typically controlled to be below 0.5 ppm (parts per million). The oxygen and moisture sensitivity of PSC fabrication depends on the precise environmental control that this glovebox can provide when excluding oxygen and moisture is necessary during device preparation. During the fabrication process of PSCs, the MBRAUN M-10-G glovebox creates an inert environment with an accurately controlled atmosphere (usually high-purity nitrogen or argon gas). Even in trace amounts, oxygen and moisture remarkably degrade perovskite precursor solutions, negatively influencing crystallization procedures and consequently leading to poor PV performances. The glovebox reduces undesirable side reactions, including perovskite degradation, decomposition into lead iodide (PbI_2), and the formation of undesirable intermediate phases by other orbitals, thereby stabilizing precursor materials and enhancing the overall quality of perovskite crystals by maintaining ultra-low levels of moisture and oxygen. In the MBRAUN M-10-G glovebox, work with perovskite precursor solutions (e.g., $MAPbI_3$, $FAPbI_3$, and mixed-halide compositions) can be carried out more safely and reproducibly. The preparation, weighing, and mixing of the perovskite precursors are carried out under inert conditions, ensuring no contact with atmospheric contaminants. The glovebox eliminates changes in the composition of the precursors due to exposure to the environment, which directly correlates with more reliable film quality and reproducible PV properties. Fabrication procedures, i.e., spin-coating or thermal annealing, etc., are thus carried out under the same atmosphere due to the careful atmospheric control offered by the MBRAUN M-10-G glovebox. In this way, the glovebox atmosphere facilitates the fabrication of solar cells with highly reproducible and reliable PV characteristics, enabling researchers and manufacturers to optimize processing conditions and Achieve Maximum PCE systematically. The device fabrication of perovskite in the MBRAUN M-10-G glovebox has largely reduced contamination at the interface between the perovskite absorber layer and other charge-transport layers, such as ETLs like TiO_2 or SnO_2, and HTLs like Spiro-OMeTAD or PTAA. With the exclusion of oxygen and moisture, the interfacial layers are pristine, and oxide barriers,

hydroxylated defects, or unwanted organic residues are minimized. Such a perfect interface state leads to a significant increase in charge extraction efficiency and a decrease in interfacial recombination losses, which can substantially enhance both the short-term device efficiency and long-term stability. The nearly inert environment of the MBRAUN M-10-G glovebox even allows manipulation of more advanced, highly reactive elements used in state-of-the-art device structures, including hybrid perovskites with (Cs^+), rubidium (Rb^+), or mixed-halide compositions. Such high-precision formulations are particularly vulnerable to atmospheric contamination. However, the glovebox offers the ability to add such materials consistently, thereby opening the door to novel research and high-performance improvements in devices that were previously hindered by environmental factors.

3.2.6. Vacuum Thermal Evaporator

VAKSIS PVD Vapour-5s_Th is a physical vapour deposition (PVD) system specifically designed for the precise deposition of thin films on substrates under a high vacuum. The advanced vacuum control, evaporation source heating, and substrate manipulation systems built into this equipment allow for precise control of the thermal evaporation of metals, especially Au, onto substrates such as PSCs. Since the manufacture of high-quality PV devices requires contamination-free deposition, the vacuum chamber of the latter has been carefully designed to ensure its continuous existence. The main component of the VAKSIS PVD Vapour-5s_Th thermal evaporation system is the vacuum chamber, which is typically manufactured from stainless steel and carefully machined and sealed to maintain an ultra-high vacuum environment, typically ranging from 10^{-6} to 10^{-7} Torr. Such high vacuum conditions can be achieved and maintained to a great extent, thereby reducing contamination from atmospheric gases, moisture, and organic molecules. This high-purity vacuum prevents the deposition of contaminants in addition to the evaporated gold, which is crucial for achieving pure, defect-free, highly conductive metallic contacts. The system utilizes a series of vacuum pumps, primarily a rotary pump to evacuate the chamber to initial vacuum levels and a turbomolecular pump to achieve the ultra-high vacuum pressures required for high-quality thin-film deposition. First, the Rotary pump quickly decreases the pressure, starting at atmospheric pressure and dropping to about 10^{-2} Torr. The turbomolecular pump then takes over, and pressure is efficiently pumped down to the required ultra-high vacuum levels

(~10^{-6} to 10^{-7} Torr). Vacuum gauges are used continuously to measure the vacuum, giving real-time feedback and allowing the vacuum deposition conditions to be carefully controlled. In the vacuum chamber of the VAKSIS PVD vapour-5s_Th, gold deposition is supported by special thermal evaporation sources, most commonly tungsten boats or alumina-coated crucibles. These crucibles are loaded with pure gold pellets or wires (usually, pellets have a purity of more than 99.99%). The crucible is then heated incrementally in a controlled atmosphere through resistive heating elements until the gold reaches its melting point (approximately 1064°C) and a slightly higher temperature, effectively. The crucible choice, material, and location in the chamber are carefully selected to offer a constant rate of evaporation, uniformity, and purity of the material. When the gold source is heated to the required temperature under an ultra-high vacuum, the gold atoms begin to evaporate into the vacuum as the thermal energy of the atoms exceeds the atomic bonding energy. This evaporation occurs because the gold atoms are free to move inside the vacuum chamber, and they do not encounter any major collisions. This is made possible by the low-pressure atmosphere. The straight line-of-sight path and low molecular collision probability enable excellent directional control, such that the gold atoms are directed straight toward the substrate. Thermal evaporation in the VAKSIS system thus results in very homogeneous and controlled rates of thin-film deposition, which are generally followed by in situ quartz crystal thickness monitors (QCM). This real-time monitoring enables the accurate control of deposition parameters, allowing for the adjustment of evaporation power, time, and substrate position to achieve a specific film specification. Accurate control enables reproducibility, consistency, and predictable device performance between batches, which is essential to both laboratory research and industrial-scale manufacturing. Sample holders or substrate stages are highly engineered to precisely locate the PSC substrates in the chamber, normally directly above the evaporation source. The delicate geometrical setup of the evaporation source and substrate ensures that the thickness and coverage of the deposition are uniform across the entire solar cell. The gold contact produced is typically thin (ranging from 50 to 150 nm), uniform, and reflective. It offers both electrical conductivity and suitable reflective qualities, which are essential for the device's proper functioning. The precise alignment of this evaporated gold atom enables it to uniformly cover the hole-transport layer (e.g., Spiro-OMeTAD, PTAA, or other organic semiconductors) and create a strong, continuous metallic contact. Additionally, rotating substrate stages or shutters can be used to enhance

film uniformity further and provide fine control over exposure time and deposition thickness. The PV performance of PSCs is significantly enhanced by the uniformly high-quality gold contacts deposited by the VAKSIS PVD vapor_5s_Th system. The high-quality Au contacts exhibit low series resistance, extract charge optimally from the hole-transport layer, and notably enhance the FF of the entire device. Moreover, the reproducibility of the deposition process would produce reproducible cell performance, enabling the systematic optimization of device structures and achieving higher overall PCEs.

3.3. Experimental Setup for Characterization

3.3.1. Scanning Electron Microscopy

Scanning electron microscopy (SEM) is the method of choice for analyzing specimen surfaces. The electron gun, which consists of an electron source and an accelerating anode, electromagnetic lenses that are used to concentrate the electrons, a vacuum chamber that houses the specimen stage, and a selection of detectors that collect the signals that were released by the specimen, is all included in the usual configuration of a SEM. Secondary electrons (SE), backscattered electrons (BSE), and characteristic X-rays are some of the signals produced when the primary electron beam strikes the sample. These signals are created as a result of the interaction between the primary electron beam and the atoms of the specimen. The collection of secondary electrons, emitted by atoms near the surface, results in the formation of topographical images with an outstanding depth of field and surface detail. The compositional contrast provided by backscattered electrons is due to the fact that heavier materials backscatter more electrons, resulting in them appearing brighter in BSE images. Backscattered electrons arise from deeper elastic scattering processes. The combination of these signals enables precise morphological and compositional imaging of the surfaces and cross-sections of PSCs. SEM is commonly used in conjunction with an energy-dispersive X-ray (EDX) detector, which enables the elemental analysis of samples. The incident electron beam can knock out inner-shell electrons when it excites the atoms in the specimen. As a result, outer-shell electrons may drop down, and the incident electron beam may produce characteristic X-rays that are element-specific. The spectra formed by measuring the emitted X-ray energy and intensity of the EDX detector allow one to deduce the elemental composition of the irradiated area.

When applied to the study of PSCs, this pairing of SEM and EDX offers a twofold function: it can both image with nanometer spatial resolution. It can perform chemical analysis to detect and map the distribution of elements. Such synergy is essential for analyzing the quality and uniformity of perovskite multi-layered devices. SEM imaging can be used to examine the perovskite film morphology in detail, including grain size, shape, and surface coverage, as well as the presence of pinholes or defects. Monolithic grain size and thick film coverage are significant factors that demonstrate the high quality of the perovskite layers, directly relating to PV activity by reducing non-radiative recombination at the grain boundaries. Films prepared at different precursor compositions or under varying processing conditions may exhibit slight differences in texture in high-resolution scanning electron micrographs. The thickness and homogeneity of the perovskite absorber, ETL, HTL, and electrode can be better understood through cross-sectional SEM imaging of a multi-layer structure. Essential variables that affect efficient charge extraction and device stability are layer stacking and interface quality.

3.3.2. Photoluminescence

PL spectroscopy is a powerful optical characterisation technique that can be used to study the electrical and defect properties of PSCs and other semiconductor materials. When a material absorbs photons, electrons are excited to the conduction band, leaving behind electron-hole pairs or excitons. The PL signal generated upon radiative recombination of these charge carriers may predict crucial information about the bandgap and defect states in the material, the recombination processes of the carriers, and the overall quality. There exist two dominant forms of PL spectroscopy used to characterize perovskites: steady-state PL, in which a sample is constantly excited, and the intensity of the emitted light at various wavelengths is measured to produce an emission spectrum, and transient PL (TRPL), where time-resolved measurements are used to trace the decay of the photogenerated carriers following pulsed excitation, providing information on charge carrier lifetimes and recombination kinetics. These measurements together give complementary details on charge transport, non-radiative losses, and trap states in perovskite films. Under the above experimental conditions, steady-state and transient PL spectra are obtained at room temperature, simulating realistic device operation conditions without the need for cryogenic cooling. The excitation source is the pulsed laser with a wavelength of 532 nm provided by Standa Ltd., Vilnius, Lithuania. The

wavelength of the green laser matches well with the absorption spectrum of popular perovskite materials and can effectively excite electrons across the bandgap. The laser is modified to a fixed fluence of approximately 10 μJ/cm², a modest excitation density that does not lead to multi-exciton generation or sample heating effects, yet maintains a good signal-to-noise ratio, enabling the detection of the PL. Because the laser is pulsed, it can be used to provide high temporal resolution in TRPL measurements: a pulse serves as a discrete excitation event, and the decay of the emission is monitored. Samples of PSCs are typically placed on a temperature-controlled sample stage, which is crucial for controlling laser spot size and illumination geometry. The laser beam is directed to the sample surface with the help of the proper optics (lenses and mirrors) to form a uniform excitation spot, the diameter of which is optimized to ensure homogeneous excitation. The incident laser fluence is precisely adjusted using power meters and beam profilers to ensure the 10 μJ/cm² threshold without any degradation or photobleaching of the sensitive perovskite films caused by the laser.

Unless moisture-related degradation is a sensitivity issue, measurements are carried out in an ambient atmosphere. Transient PL spectroscopy utilizes the pulselike behavior of the laser to illuminate the sample with brief pulses (typically in the picosecond to nanosecond range). The emitted PL intensity is measured as a function of time following each excitation pulse with fast photon-counting detectors (avalanche photodiodes or streak cameras) with the capability of recording the decay dynamics on the nanosecond to microsecond timescale. The obtained PL decay curves give direct information on charge carrier recombination lifetimes and processes in the perovskite film. It can be said that when looking to extract charge-carrier lifetimes specifically as part of a multilayer construction, as is the case in an example like that shown (Glass/FTO/CompactTiO_2/PorousTiO_2/Perovskite /Spiro-OMeTAD/ Au), one must consider the interactions between the various layers. Both electron-transport (TiO_2) and hole-transport materials (Spiro-OMeTAD) are two of these layers, with distinctly different recombination properties and lifetimes; the interfaces also introduce new sources of recombination. Therefore, direct measurements usually provide an effective lifetime that takes into consideration the contributions of all layers and interfaces.

Advanced experimental and analysis techniques are used to selectively and distinctly identify the charge-carrier lifetime in the perovskite layer. One of the most frequently employed experimental methods is TRPL. One can

ensure that the generation of charge carriers will be primarily in the perovskite by selecting an excitation wavelength that is strongly absorbed by the perovskite layer. TRPL observes the degradation of luminescence intensity, which is directly associated with the charge recombination process in this layer. Nevertheless, recombination at the interfaces (perovskite/TiO_2 and perovskite/Spiro-OMeTAD) can have a significant impact on apparent lifetimes, even in the case of selective excitation, making interpretation complicated. TRPL may additionally be complemented through transient absorption spectroscopy (TAS). TAS can be used to observe the temporal evolution of absorption variations over time after a brief excitation pulse, allowing for forward probing of charge-carrier dynamics in perovskites by selecting probe wavelengths close to the perovskite layer. Nevertheless, as in the case of TRPL, the effects of interface recombination and transport-layer must be taken into account and carefully considered to make sure that the measurements are accurate, reporting the actual intrinsic perovskite lifetimes.

Selective optical probing, assisted by comparison with reference samples, detailed device modeling, and variations in experimental conditions (e.g., thickness variation of the layer or interface passivation), is required to extract the perovskite charge carrier lifetime in a multilayer structure. Through this combination, the perovskite lifetime can be effectively determined and separated from the effective lifetime affected by the "other" layers and interfaces in a multilayer architecture.

A single exponential decay is frequently associated with simple radiative recombination. In contrast, a multiexponential or stretched exponential decay suggests the existence of multiple recombination channels, such as trap-assisted nonradiative recombination. The implication of the longer PL lifetime is lower non-radiative recombination losses, which are typically associated with better PV performance. Carrying out PL and transient PL spectroscopy at ambient conditions closely resembles the realistic operating conditions of PSCs. It thus gives practically relevant information about the optoelectronic behavior of the latter. A pulsed laser at 532 nm with a controlled fluence supplied by a trustworthy manufacturer such as Standa Ltd. guarantees repeatability and excellent control over excitation. Caution must, however, be taken to ensure that laser-induced heating or degradation is avoided, as this can cause changes in the PL response. To minimize such effects, measurements are typically performed rapidly and under interrupted lighting conditions. Additionally, quantitative

spectral analysis necessitates calibration against reference standards and correction for detector response.

3.3.3. Transient Photovoltage

Transient Photovoltage (TPV) studies are a powerful test method for analysing charge carrier dynamics, recombination kinetics, and overall device quality in PSCs. Specifically, TPV monitors the time-resolved PV response of a solar cell to pulsed optical excitation and can indicate the lifetimes of charge carriers in an open circuit. TPV can provide data on the recombination mechanisms that limit the stability and efficiency of solar cells by applying a small perturbation to photogenerated carriers through a short laser pulse and observing the resultant voltage decay. Transient photovoltage experiments were performed using a diode-pumped, frequency-doubled Nd: YAG laser system, NL202, manufactured by Ekspla Ltd., Vilnius, Lithuania. This laser is pumped to produce pulses with a wavelength of 532 nm (green light), which is the second harmonic of the fundamental 1064 nm output of the Nd: YAG crystal. The experimental setup for transient photo-voltage measurement is shown in **Figure 16**.

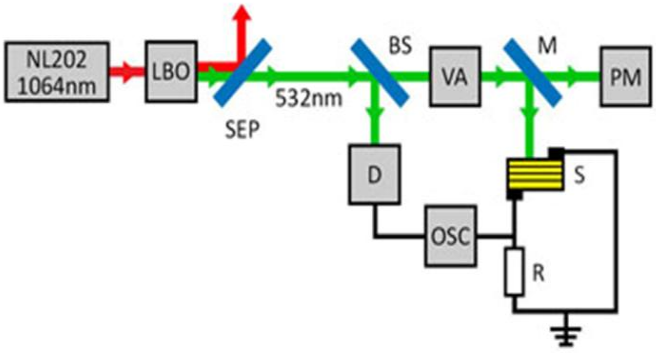

Figure 16. Scheme of experimental setup of transient photo voltage measurement.

The core of the system is an NL202 diode-pumped Nd: YAG laser, with a pulse duration of 10 ns at 1064 nm. Most semiconductor samples of interest (the bandgaps of which fall in the visible) are excited efficiently by the frequency-doubled basic 1064 nm laser beam in an LBO (lithium triborate) nonlinear crystal to produce 532 nm flashes. Any remaining light at 1064 nm is then removed by the SEP (second-harmonic separator), resulting in a clean green pump light. This is a short, high-intensity pulse

that supplies the rapid optical excitation needed to produce a fast photovoltage transient on the device under test.

A beam splitter (BS) sends a fraction of the 532nm pulse to an optical reference detector (D), which (a) produces an accurate timing start trigger signal to the oscilloscope, and (b) enables a check to be made of pulse-to-pulse energy variations. This then enters an adjustable attenuator (VA), commonly a slow rotation of a half-wave plate and polarizer or a neutral-density wheel, which allows the pump fluence to be varied continuously (and arbitrarily) without realignment. The flexibility is provided by a removable mirror (M), which allows you to insert a diagnostic or deflect the beam to perform an alignment, and then reestablish the measurement path. The sample (S), the object of study, conventionally a solar cell or semiconductor junction, is struck by the conditioned pulse, usually of near-normal incidence. The formation of electron-hole pairs causes a transient charge separation within the device's built-in field, which can be observed as a rapid increase in the open-circuit voltage, commonly referred to as a spike. To measure that in a quantitative signal, the device terminals are short-circuited together through a load resistor (R). This resistor serves the dual purpose of both impeding the circuit and defining the RC time constant of the measurement.

Additionally, it is the input impedance of the following electronics, thereby maximizing signal transfer. A high-bandwidth digital storage oscilloscope (OSC) captures the reference trigger and voltage across R, after any baseline or electrical signal has been subtracted from it. Multiple pulses are averaged (optionally), resulting in the transient photovoltage waveform: a fast component (hot-carrier or displacement current) followed by one or more slow components (carrier recombination, thermal equilibration, and circuit RC time constants). Fitting the complete rise time, amplitude, and decay constants provides access to the carrier lifetime and trap dynamics. The wavelength of 532 nm effectively coincides with the absorption profile of perovskite materials, where electron-hole pairs are excited across the band gap. The duration of each laser pulse is on the order of 9 nanoseconds, which is short enough to be classified as an impulsive excitation on the timescale of carrier recombination dynamics in perovskites. The repetition rate of the laser is 50 Hz, which delivers a continuous flow of pulses to enable repetitive and averaged TPV measurements, thereby enhancing signal-to-noise ratios without degrading the sample. **Figure 17** illustrates the temporal shapes of the laser pulse of TPV.

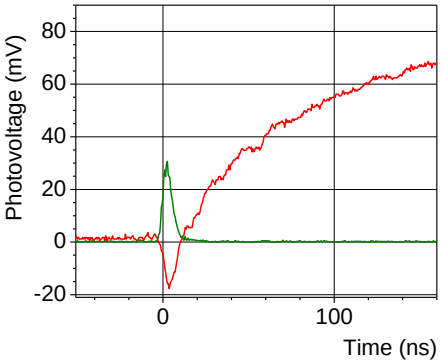

Figure 17. Temporal shapes of the laser pulse (green) and photovoltage (red) of the PSC

A high-speed digital oscilloscope or a fast photovoltage amplifier system that can resolve dynamics on the nanosecond-to-millisecond timescale records the TPV transient. We can determine how long photogenerated carriers persist before recombining by fitting the voltage decay to exponential or stretched-exponential functions. This gives us characteristic recombination time constants. Longer lifetimes are associated with reduced non-radiative recombination and improved solar cell quality. The TPV data can be used to determine the density of trap states, recombination pathways (monomolecular vs. bimolecular), and charge transport properties, as the excitation fluence and repetition rate are well-controlled and precisely known. These insights help improve perovskite films, interface engineering, and device architecture, enabling them to function more effectively and last longer.

3.3.4. Optical Transmittance

In PSC research, measuring absorbance spectra is essential for comprehending the efficiency of a perovskite film in capturing and converting solar photons into usable electrical energy. The absorbance spectrum provides direct information about the film's optical bandgap, its light collection efficiency, and potential loss mechanisms, such as defect-mediated sub-bandgap absorption. Researchers can determine the quality of the material, adjust the compositions of perovskites to achieve optimal coverage of the solar spectrum, and identify issues such as phase impurities or compositional inhomogeneity that could impact device performance by accurately estimating absorbance spectra. It is often not possible to directly measure absorbance because perovskite films are typically deposited as thin

layers on transparent substrates, such as glass or FTO-coated glass. Instead, transmission data is used to estimate the absorbance spectrum indirectly. This involves shining a collimated beam of light, typically a broadband source, through the perovskite film and measuring the amount of light transmitted at each wavelength. The AvaSpec-ULS2048XL-EVO spectrometer plays a crucial role in this process, as it accurately detects the transmitted light at various wavelengths. A schematic of optical transmittance is illustrated in **Figure 18.**

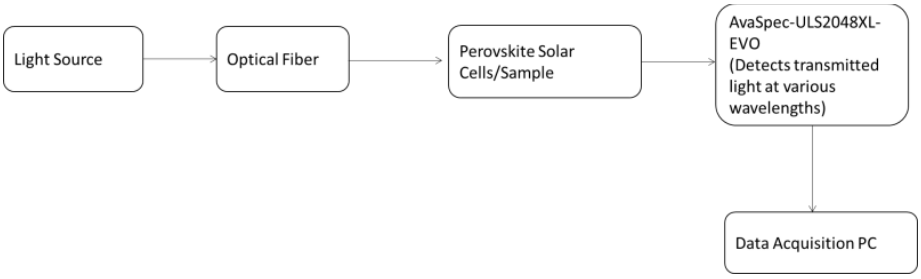

Figure 18. Schematic of optical transmittance measurements

To separate the effect of the perovskite film from the impact of the substrate, a reference spectrum is first obtained using an identical substrate but without a film. The transmission spectrum of the perovskite-coated substrate is divided by the reference to get the normalized transmission. This eliminates artifacts from the lamp spectrum, substrate absorption, and reflection.

The thickness of the layers in perovskite solar cells is crucial in determining the overall photovoltaic performance of the cell. The absorption of light, charge transport, and recombination processes will be balanced in each layer (excluding the perovskite absorber layer, the electron transport layer (ETL), and the hole transport layer (HTL)) by adjusting material properties. To illustrate, an adequate value of the perovskite absorber layer should possess enough thickness of at least 300 to 600 nanometers to capture a considerable amount of incoming light. When this layer is too thin, not enough light is absorbed, resulting in a limited generation of charge carriers and, consequently, a limited output current. On the other hand, an excessive thickness of the absorber material can result in large bulk recombination and inefficient charge extraction in the device, as carriers have to diffuse longer distances, which has been observed to have adverse effects on device performance. The thickness of the charge transport layers beyond the perovskite layer also affects the device's performance. Both the electron transport layer and the hole transport layer should be thin enough to enable

high charge extraction density while still forming continuous films to avoid shunting paths. The normal thickness of these layers is 30 to 100 nanometers. Series resistance can be increased, as can charge mobility, by using thicker layers; however, charging may not be complete due to excessively thin layers.

3.3.5. Current-voltage Measurements

Current-voltage (J–V) characterization under illumination is the primary method for evaluating the PV performance of PSCs. The J–V curve directly reveals the major device parameters: V_{OC}), J_{SC}, FF, and PCE. For measuring these characteristics, a well-calibrated source measurement unit (SMU) and a standard, well-characterized light source are required to ensure both electrical and optical reliability and reproducibility. The Keithley 2602A is a high-performance dual-channel SourceMeter instrument that simultaneously sources voltage and measures current (or vice versa) with high precision and minimal noise. In solar cell J–V measurements, the instrument is typically operated in "sweep" mode: the SourceMeter sources a voltage stepwise through the solar cell terminals while measuring the corresponding current at each voltage Step. This probe is chosen for its accuracy (picoampere-range current sensitivity), broad dynamic range, and programmability, which are appropriate for the typically low current output of laboratory-sized perovskite devices. Electrical contacts are established with the front (most commonly the transparent conducting oxide, such as FTO or ITO) and back (the metal electrode) of the solar cell using probe needles, alligator clips, or a specially designed sample holder to achieve low contact resistance and high mechanical stability. The Keithley 2602A can be operated under software-specific programs or command-driven scripts, providing fine control over the speed of voltage sweep, direction of sweep, Step size, and integration time of measurement. Accurate characterisation of PV devices must be performed under illumination that closely replicates the solar spectrum. Newport model 67005 spectrum lamp provides stable broadband light with spectral content traceable to the AM 1.5G standard (the internationally accepted "one sun" condition) required for comparing device measurements to the world.

The intensity of the lamp is carefully set before measurement to deliver exactly 100 mW/cm², equivalent to "one sun," to the sample plane. This calibration is performed using a calibrated reference photodiode or Silicon cell. The lamp-solar cell distance is standardized and adjusted with very high

accuracy, ensuring spatial uniformity and illumination reproducibility across the device area. The sample is positioned so that light strikes the device surface normally, minimizing angular effects and ensuring uniform exposure. Temperature measurement or control is often employed to prevent sample heating, which can impact the performance of devices.

3.4. Fabrication and Characterization of Samples

Perovskite films were prepared in this investigation using the procedures that were described earlier in the article. The prepared materials (perovskite, Spiro-OMeTAD, CsI, LiTFsI, Sn_2) are shown in **Figure 19.**

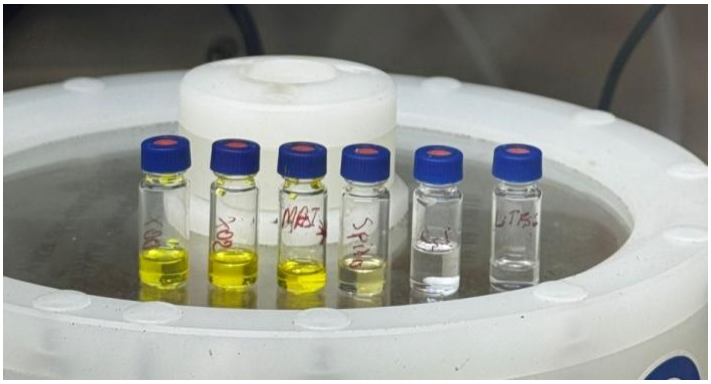

Figure 19. Materials for spin-coating inside the glovebox.

Along with the sequence of techniques and equipment that were utilized in the fabrication process of the $Cs_x(FA_{0.83}MA_{0.17})_{(1-x)}Pb(I_{0.83}Br_{0.17})_3$ PSC, it included a comprehensive analysis of the reagents, including parameters regarding their concentrations and levels of purity. Initially, the preparation process began with glass substrates of a specific dimension of 25×25 mm^2. These substrates were already uniformly covered on the transparent conductive FTO (TEC 10, Ossila B.V., Sheffield, UK). A particular area of this FTO layer (approximately 7x25 mm^2) was carefully scraped off on one side using a scratching procedure that comprised zinc powder (Sigma-Aldrich, St. Louis, Missouri, USA) and hydrochloric acid (Merck KGaA, Darmstadt, Germany). This was done to make sure that the border was clean and precision was absolute. The following steps of substrate cleaning were necessary and thorough, starting with a twenty-minute ultrasonic bath in a carefully prepared 2% solution of Hellmanex (Sigma-Aldrich, USA). This bath was meant to remove any organic residues that might have remained. Following ultrasonic cleaning, the item was washed multiple times with

ultra-pure deionized water to ensure thorough cleaning. A further ultrasonic treatment with isopropanol (Merck KGaA, Darmstadt, Germany) was performed for an additional 20-minute period to complete the further harsh cleaning process.

Lastly, the substrates were subjected to a plasma treatment that lasted precisely 10 minutes. This treatment further improved the surface cleanliness of the substrate, ensuring that succeeding layers would have optimal adhesion qualities. Each essential step involved in the production of these enhanced PSCs is depicted clearly and concisely in **Figure 20**.

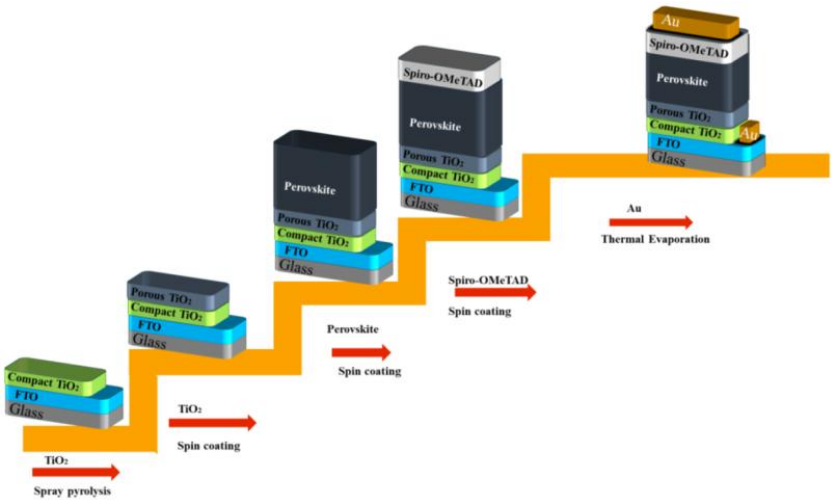

Figure 20. A schematic representation of the PSC development process is illustrated in a progressive manner.

In the first phase, a uniform, compact coating of TiO_2 was methodically deposited onto the cleaned FTO substrates using spray pyrolysis. The temperature was maintained at 450°C throughout the entire process. The precursor solution that was utilized in this stage consisted of titanium di-isopropoxide bis(acetylacetonate) (Ti(acac)OiPr, Merck-KGaA, Germany) that was precisely mixed in anhydrous ethanol (Sigma-Aldrich, Missouri, United States) at a volumetric ratio of 1:9. After the deposition process, the substrates were annealed at 450°C for precisely 15 minutes to improve the crystalline quality and attain the highest possible conductivity. After that, they were brought down to room temperature at a controlled rate to prevent any structural strains or faults from occurring. The second Step of the design process involved the fabrication of a mesoporous TiO_2 scaffold, which is

necessary to support electron transport and cell performance. A suspension consisting of titanium oxide nanoparticles, uniformly dispersed with an average diameter of 30 nm, was diluted with ethanol in a weight ratio of 1:6 with a precise volume of 180 μL. This suspension was spin-coated onto substrates at a rate of 4000 rpm in precisely 20 seconds, and the rate of acceleration was maintained at 2000 rpm·s^{-2}. To ensure the structural integrity of this layer, it was indeed well done; it required an annealing process at 450°C for 30 minutes. This procedure created clear pores, which are crucial for the subsequent infiltration of perovskite. The substrates were rapidly transferred to a glove box filled with nitrogen (M-Braun Inertgas-Systeme GmbH, Garching bei München, Germany) upon completion of the annealing process. The purpose of this glove box was to provide a strictly controlled, moisture-free environment.

The essential perovskite layer was carefully deposited from freshly generated precursor solutions during the third Step of the process. The following molar concentrations were utilized: 1.2 M lead iodide (PbI_2; Sigma-Aldrich, Missouri, United States of America), 0.2 M methylammonium bromide (MABr; Greatcell Solar Italia, Italy), 0.2 M lead bromide ($PbBr_2$; Sigma-Aldrich, Missouri, United States of America), and 1 M formamidinium iodide (FAI; Greatcell Solar Italia, Italy). To meticulously prepare the solvent system, anhydrous DMF and dimethylsulfoxide (DMSO, Sigma-Aldrich, Missouri, USA) were mixed at a volumetric ratio of 4:1. To accurately regulate the Cs concentration at 10%, Cs iodide (CsI, Strem Chemicals Inc., Massachusetts, United States) was added. The Cs were first dissolved at 1.5 M in DMSO. To manufacture films with the composition $Cs_x(FA_{0.83}MA_{0.17})_{(1-x)}Pb_{0.8}Sn_{0.2}(I_{0.83}\,Br_{0.17})_3$, PbI_2 and SnI_2 were incorporated into the mixture in a molar ratio of 4:1, which was precisely maintained. To ensure complete solubilization and homogeneity, the solution was thoroughly stirred at 60 °C for precisely one hour. A severe two-step technique was used to spin-coat this precursor solution. First, the solution was spun at a speed of 1000 rpm for precisely ten seconds. This was immediately followed by a spin at a higher speed of 6000 rpm for an additional thirty seconds. Over the final 10 seconds of spinning, an antisolvent treatment consisting of precisely 150 μL of chlorobenzene (Sigma Aldrich, Missouri, United States) was delivered. This treatment was essential for ensuring the optimal crystallization of perovskite. After that, a strong crystalline structure was obtained by annealing at 100°C for 60 minutes. In the fourth stage, the development of the HTL was the primary focus. Exactly 150 μL of a solution, which comprised 70 mM Spiro-

OMeTAD in chlorobenzene (CB) of 85.78 mg/mL concentration, was spun-coated. The solution was added to Li-TFSI salt (520 mg/mL in anhydrous acetonitrile) and 4-tert-butylpyridine (TBP), which were purchased separately from Sigma Aldrich, Missouri, United States of America, in a careful manner at a molar ratio of 0.5 and 3.3, respectively. The spin-coating process was carried out at 4000 rpm for 25 seconds, and a rapid acceleration of 2000 $rpm \cdot s^{-2}$ was maintained to ensure a uniform and defect-free HTL in the final phase. High-quality gold connections were then deposited using thermal evaporation. The thickness of these contacts was precisely controlled to be approximately 70 nm. During this crucial operation, which was carried out in a vacuum chamber of the advanced evaporation system known as VAKSIS-PVD-Vapor-5S_Th (Vaksis Research and Development & Engineering, Ankara, Turkey), the electrode creation was designed to be as strong as possible to achieve the highest possible level of device functionality.

3.4.1. Characterization

A scanning electron microscope (SEM) (Helios NanoLab 650, FEI, Hillsboro, Oregon, United States) was used to investigate the thickness and shape of the perovskite films. We were able to analyse the chemical composition of the films by combining SEM with an EDX system manufactured by INCA Energy and Oxford Instruments in Abingdon, United Kingdom. To determine the crystalline structure of the perovskite films, a theta/theta goniometer and an X-ray diffractometer (SmartLab, Rigaku, Tokyo, Japan) were used. The X-ray diffraction device is equipped with a revolving Cu anode X-ray source that has a power output of 9 kW. To measure the patterns within a 2θ range of 10–70°, the Bragg-Brentano geometry was specifically employed. We examined the fundamental characteristics of the X-ray diffraction (XRD) patterns of full-scale perovskite layers. Additionally, we conducted a comprehensive investigation of the XRD pattern fragments that fell within the 2θ range of 26–29°.

PL and TRPL spectra were systematically measured at room temperature to explore the optoelectronic properties and dynamics of the perovskite film's charge carriers. The measurements are significant for identifying the quality of the perovskite film, radiative recombination efficiency, and the presence of non-radiative decay channels, which have an impact on solar cell performance. Conducting these experiments at ambient temperature ensures that the data are relevant to real operating conditions where devices are typically deployed. Excitation was achieved through a

pulsed laser source with a wavelength of 532 nm, which provides photon energy sufficient to excite electrons across the bandgap of standard perovskite formulations. The laser, courtesy of Standa Ltd. (Vilnius, Lithuania), emitted pulses of controlled fluence of 10 μJ cm^{-2}. The density of this excitation is tuned to be strong enough to create a solid PL response without creating nonlinear effects or degrading the weak perovskite material. The pulsed laser also enables precise time resolution in transient PL measurements, allowing for the probing of fast carrier recombination and trapping processes on timescales ranging from nanoseconds to microseconds.

A highly advanced time-resolved experimental system, well established to illuminate charge carrier dynamics and recombination processes within PV devices, was used to examine the TPV response of PSCs. It utilized a diode-pumped, frequency-doubled Nd: YAG-LBO laser model NL202, supplied by Ekspla Ltd. (Vilnius, Lithuania), as the optical excitation source. Due to its capability to produce highly reproducible and stable pulses with a pulse length of 9 nanoseconds and an emission wavelength of 532 nm, well-suited to the absorption spectrum of the majority of perovskite materials, and providing efficient photogeneration of charge carriers within the active layer, this laser was specifically selected. An effective combination of sufficient data collection and reduced sample damage or cumulative heating was achieved by the laser pulses, which were created at a repetition rate of 50 Hz. This may be particularly significant for delicate perovskite materials. The average optical power transferred to the sample was accurately calibrated and controlled during experiments using the PM400 optical power meter manufactured by Thorlabs Inc. (Newton, NJ, USA). The excitation fluence used for illumination was kept constant for each measurement, based on the high accuracy and rapid response of this power meter, which is critically essential for a valid comparison and analysis of the TPV data. The PSC was usually kept in an open-circuit condition during every TPV measurement. Upon impact with the cell, the 9 ns laser pulse caused a brief surge in photovoltage by rapidly increasing the number of photogenerated carriers. The dynamics of charge carrier recombination and extraction were revealed by monitoring the following relaxation or decay of this photovoltage. One can learn a great deal about the device's recombination lifespan, trap state presence, and charge separation effectiveness from the temporal history of the transient photovoltage signal. We used a state-of-the-art digital storage oscilloscope from Agilent Technologies (Santa Clara, CA, USA) to accurately capture and analyze these rapid voltage transients. The

photovoltage decay curve can be acquired with high bandwidth and high sampling rates using this instrument, allowing it to capture transient response details that less capable instruments would have missed. Due to the millisecond durations involved, the laser excitation and voltage signal needed to be precisely timed. Additionally, a high-speed optical signal reference detector from Standa (Vilnius, Lithuania) was incorporated into the optical setup to precisely monitor and synchronize the exact timing of each laser pulse. For each incident laser pulse, this detector generates a reference signal that the oscilloscope can use as a trigger, allowing for precise temporal correlation between the laser excitation and the subsequent photovoltage response.

We used the AvaSpec-ULS2048XL-EVO, a highly accurate spectrometer manufactured by Avantes in Apeldoorn, the Netherlands, to measure transmission. With this data, investigators were able to make an accurate estimate of the optical absorbance spectra of the perovskite films. Most of the time, glass or FTO was used as the clear substrate through which the perovskite-coated white light passed. The intensity of the transmitted light passing through both the sample and the blank reference substrate was measured and recorded over a wide range of wavelengths, from ultraviolet to near-infrared. Using the 2602A SourceMeter instrument (Keithley Instruments Inc., Cleveland, Ohio, USA), renowned for its precision and low-noise characteristics, the direct measurement of the J–V behaviour of the as-prepared PSCs was performed to study their electrical performance. Electrical contacts were made on the front and back electrodes of the solar cell devices, resulting in low contact resistance and a firm connection. The solar cell devices were stored in a safe measurement station. To record the current that was developed at each Step of the process, the 2602A was programmed to sweep the applied voltage over the device in precisely controlled steps. A full characterisation of the diode's response, including the determination of series and shunt resistance values, as well as the accurate calculation of PV parameters such as J_{SC}, V_{OC}, FF, and overall PCE, was achieved by conducting these measurements in both dark and illuminated conditions. We illuminated the solar cells using a Newport model 67005 spectrum lamp (Newport Corp., Irvine, CA, USA) in a manner that ensured consistent electrical measurements, reflecting the device's potential as a PV device under standard test conditions. We made the light very uniform by keeping this light source at a particular distance above the device. A certified reference photodiode was used to calibrate the lamp, ensuring that the irradiance in the plane of the solar cell was precisely 100 mW/cm². This

corresponds to the AM1.5G solar spectrum, which is the reporting standard for the efficiency with which a solar cell operates. During the measurement campaign, the light source was periodically verified for stability and calibration to ensure the accuracy and reproducibility of the data. This rigorous process of measuring the optical and electrical properties of the PSCs enabled the attainment of reproducible performance metrics, which could be directly compared with one another. This was the basis upon which further development and comparison with the best solar panel technologies available could be made.

3.5. Results and Discussions

3.5.1. The Influence of Hot Carriers on Photovoltage Formation in PSCs

Extensive experimental research was done to present a systematic analysis of the structure, PL, and optical properties of two types of triple-cation perovskite films containing Cs. The first form that was researched was $Cs_x(FA_{0.83}\ MA_{0.17})_{(1-x)}Pb(I_{0.83}\ Br_{0.17})_3$. The second form consisted of partial substitution of lead with tin, resulting in the formation of $Cs_x(FA_{0.83}MA_{0.17})_{(1-x)}Pb_{0.8}Sn_{0.2}(I_{0.83}\ Br_{0.17}\ )_3$. These meticulously crafted compositions were selected to illuminate the impact of compositional tuning and element substitution on the film's structure and optoelectronic properties. The perovskite film crystallinity, grain size, and surface morphology were investigated in this study using a combination of characterization techniques, including SEM and XRD. PL spectroscopy was employed to investigate the defect states and carrier lifetimes in the films, as well as to evaluate the radiative recombination dynamics. Critical properties for effective solar energy harvesting, such as the optical bandgap and spectral range of light absorption, were also determined for all perovskite compositions through optical transmission and absorbance studies.

A central aim of the study was to determine how the HC functions in these perovskite layers. We utilized TPV measurements to investigate the hot carrier effect and its influence on device functionality when exposed to pulsed laser light. We were able to determine how PSC devices achieve PVs by measuring the process in real-time. The TPV measurements clearly showed that both types of perovskite layers had the hot carrier effect. It was demonstrated that HC significantly influences the initial stages of PV production. The time-resolved photovoltage response exhibited two distinct parts with opposite polarities that behaved in an unusual manner. This interesting finding suggests that each of these processes has a different effect

on photovoltage. These two findings on PV components demonstrate the complexity of carrier dynamics in optimized perovskite materials. It explains the relevance and importance of hot carrier relaxation processes on the physics of PSCs and their mechanism. In addition to deepening our understanding of the fundamental processes by which photovoltages are generated, this work suggests approaches to optimizing both material composition and device structure to exploit hot carrier effects. This may further increase the efficiency of PSCs. The fast photovoltage component, designated U_f, has a temporal shape that closely follows the form of the incident laser pulse used to excite the device. This direct correlation indicates that U_f is generated in the ultrafast events that occur after light absorption, specifically in the hot electrons and holes created by the high-energy photons. Exciting the perovskite layer with a short and intense laser pulse first allows the excess energy to be transferred into the charge carriers, creating a non-equilibrium, or hot, carrier population before allowing them to equilibrate with the lattice. This hot carrier heating results in a high-frequency, transient photovoltage response that is both temporally and physically distinct from the conventional photovoltage signals. Conversely, the slow component of the photovoltage observed is indicative of the regular process of the PV effect in PSCs. In this case, the incident photons generate electron-hole pairs in the perovskite absorber, which are subsequently separated and collected at the device electrodes, resulting in a conventional photovoltage. This typically occurs on a timescale that is longer and is determined by the dynamics of carrier generation, separation, transport, and extraction within the device. This slow, steady-state photovoltage is positive-going with the standard device operating conditions and is the source of external circuit current when the device is illuminated. One of the most surprising and new findings of these measurements is that the polarity of the fast component, Uf, is reversed compared to that of the traditional, slower photovoltage. That is to say, the rapid increase in hot carrier-generated photovoltage immediately after photoexcitation works in the opposite direction of the required, long-lived photovoltage that provides the current through the external circuit. This effect implies that hot-carrier effects will not just be a temporary novelty but can work to reverse or reduce the net photovoltage that can be used to produce power.

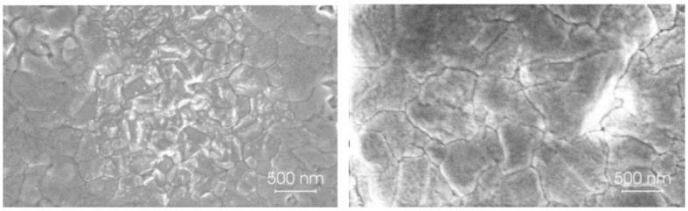

Figure 21 shows the top-view scanning electron microscopy (SEM) images of the two kinds of perovskite films, $Cs_x(FA_{0.83}MA_{0.17})_{(1-x)}Pb(I_{0.83}\,Br_{0.17})_3$ and $Cs_x(FA_{0.83}MA_{0.17})_{(1-x)}\,Pb_{0.8}Sn_{0.2}(I_{0.83}\,Br_{0.17}\,)_3$.

F**igure 21** provides a firsthand visual impression of the surface topography and grain structure of the prepared perovskite layers, which is crucial for interpreting and matching the microstructure of the material with its optoelectronic properties and solar cell performance. By examining the SEM micrographs carefully, it can be observed that both perovskite films exhibit a good formation of densely packed grains that are uniformly distributed on the surface. The shape of the grains in the Cs-incorporated lead-only perovskite and the mixed metal lead-tin perovskite is highly similar, meaning that the replacement of a part of lead with tin does not radically change the overall film-forming strategy and film quality in terms of grain coverage. Upon close observation of the SEM micrographs, it can be noted that both perovskite films exhibit a good and dense grain structure, which is uniformly dispersed over the surface. The shape of the grains in the Cs-containing lead-only perovskite and the mixed-metal lead-tin perovskite is strikingly similar, indicating that the replacement of part of the lead with tin does not significantly alter the overall film-forming tendency or the film quality, particularly in terms of grain coverage. Notably, the two films are smooth without pinholes, which is an essential requirement for high-performance PSCs. The absence of pinholes ensures that there are no direct Shunt routes between the electron and HTL, which reduces the possibility of leakage currents and increases the overall device efficiency. A closer examination of the SEM images, however, reveals some marginal differences in the grain size of the two types of perovskite films. The grains of the pure lead-based perovskite film, $Cs_x(FA_{0.83}MA_{0.17})_{(1-x)}Pb(I_{0.83}\,Br_{0.17})_3$, tend to be smaller and closer packed than those found in the mixed Pb-Sn perovskite, $Cs_x(FA_{0.83}MA_{0.17})_{(1-x)}Pb_{0.8}Sn_{0.2}(I_{0.83}\,Br_{0.17}\,)_3$ It also seems that the addition of tin into the perovskite lattice allows the formation of larger crystalline grains, which can be important concerning the optoelectronic properties. Bigger grains mean fewer grain boundaries per area, which is

desirable since grain boundaries can act as non-radiative recombination centres where carrier charges can be trapped, causing the device to become less efficient. The layer thickness of perovskite is frequently proportional to the average grain size. It is expected that thicker perovskite layers will form larger grains during annealing and crystallization because there is more material and space available for the grains to grow. This correlation highlights the importance of regulating deposition conditions and Film thickness during the fabrication process to optimize the microstructure and achieve optimal device results. In the current work, a keen control of the processing parameters has led to the observation that both films exhibit desirable smooth and compact morphologies with grain sizes suited to facilitate efficient charge transport and collection in PSCs.

The high-resolution cross-sectional SEM images of the two perovskite films, (a) the conventional lead-based perovskite, $Cs_x(FA_{0.83}MA_{0.17})_{(1-x)}Pb(I_{0.83}\ Br_{0.17})_3$ and (b) the lead-tin mixed perovskite, $Cs_x(FA_{0.83}MA_{0.17})_{(1-x)}\ Pb_{0.8}Sn_{0.2}(I_{0.83}\ Br_{0.17}\ )_3$ Such cross-sectional images provide visualization of the grain structure right across the thickness of the perovskite layer which is key to optimizing both optical absorption and charge transport properties when used as a solar cell. The images have accurately shown the measured film thicknesses. This indicates that the Pb-Sn mixed perovskite layer (**Figure 22b**) is significantly thicker, with the perovskite layer itself being approximately 1 μm (987.7 nm) thick, compared to the lead-only perovskite layer (**Figure 22a**), which is approximately 800 nm (804.3 nm) thick. This enhancement in the thickness of the Pb-Sn alloyed film can be attributed to the modification of the dynamics of the crystallization and film-formation process upon the addition of tin, which impacts the viscosity of the solution and alters the nucleation and crystal growth rates during deposition and annealing. Examining the internal microstructure, the lead-based perovskite film (**Figure 22a**) exhibits grains that are predominantly vertical and tend to stack on top of each other. This vertical grain orientation is potentially advantageous for the transport of charge carriers across the device's thickness, as it creates direct paths along which electrons and holes can be transported from the photoactive layer to the appropriate charge transport layers. Thus, the chance of recombination at the grain boundaries is minimized. Conversely, in the mixed Pb-Sn perovskite film (**Figure 22b**), the grains are much larger, and a lateral or horizontal orientation dominates their growth. Such a lateral design may benefit the uniformity of the film and also lead to increased mechanical strength. Non-radiative recombination losses could also be minimized by the

presence of larger grains and by the lower density of grain boundaries in the vertical direction, as long as the grain boundaries are well-passivated and free of defects. Direct visual confirmation of the effect of compositional engineering (through tin addition) on the thickness and internal grain orientation of perovskite films is given by the cross-sectional SEM image in **Figure 22**. These structural features are fundamental to the further development of PSC technology and require understanding and control as they determine the interaction between optical absorption, carrier dynamics, and device stability.

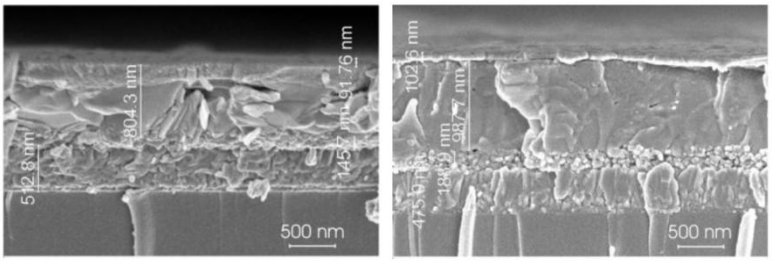

Figure 22. Cross-sectional SEM images of the formed perovskite films: (a) Pb-based perovskite; (b) Pb-Sn-based perovskite.

Figure 23 shows the optical transmittance spectra of the pure lead-based perovskite film (denoted by the green curve) and the mixed-metal lead-tin (Pb-Sn) perovskite film (denoted by the blue curve). The spectra directly provide information on how individual perovskite compositions respond to incident light of a wide spectrum, spanning from the visible to the near-infrared wavelength range. Optical transmittance spectra are not only crucial for understanding the optical bandgap and optical absorption properties of these materials but also for their applicability in the efficient harnessing of solar energy. After a close consideration of the curves, it is evident that both types of perovskite films exhibit extremely low transmittance (near zero) at shorter wavelengths, i.e**.,** less than 700 nm. Such an absorption feature is typical of good light absorption in the visible regime, as required in useful solar absorbers. However, sharp differences are observed when the wavelength extends further into the near-IR region. Compared to the pure Pb-based perovskite (green curve), the Pb-Sn-based perovskite (blue curve) invariably has a lower transmittance in the infrared**,** particularly at wavelengths longer than 800 nm. This decreased transparency implies that adding tin increases the material's capacity to absorb longer-

wavelength photons, which can lead to better utilization of solar light but also alters the material's basic optical characteristics. An interesting feature observed in the spectra is the difference in the redshift of the transmittance edge for the Pb-Sn-based perovskite film. The absorption edge, where transmittance increases steeply, having been near zero to higher values, is at a longer wavelength in the tin-containing perovskite than in the pure lead one. Such a redshift corresponds to the narrowing of the forbidden energy bandgap that is a direct result of the partial substitution of lead by tin in the perovskite crystal lattice.

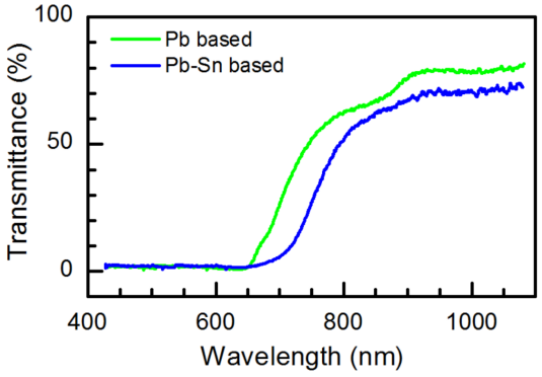

Figure 23. Optical transmittance spectra of Pb-based and Pb-Sn-based perovskite films.

The PL spectra and room temperature transients are presented in **Figure 24**. Two Gaussian functions are used to fit the peak of the Pb-based sample. This discrepancy approaches the exciton binding energy as calculated from absorption spectra by approximately 25 meV.[283]

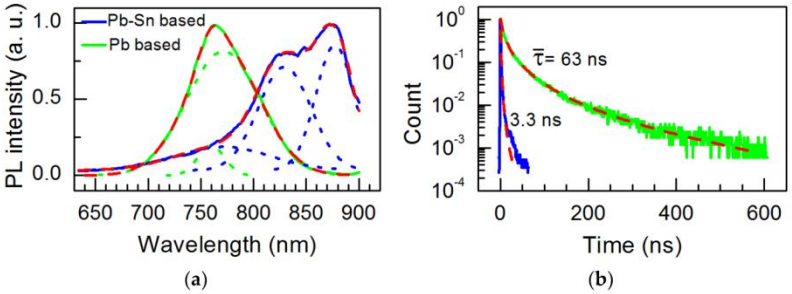

Figure 24 shows the perovskite layers made of Pb (green) and Pb-Sn (blue), together with their PL spectra (a) and transient decay (b). For fitting

findings, refer to the red dashed lines; for the Gaussian distribution, see the dotted lines.

A set of three Gaussian peaks fits the spectrum of the Pb-Sn-based sample. For the Sn-free sample, one remains constant, but the other two are moved to lower energies by 112 and 194 meV, respectively. The disparity of 82 meV between them is excessively large to be associated with the exciton binding energy. Consequently, these two peaks may correspond to emissions from crystallites of varying sizes or structures with distinct compositions [284]. The average decay time was computed numerically and found to be

$$\bar{\tau} = \frac{\int_0^\infty t I_{PL}(t) dt}{\int_0^\infty I_{PL}(t) dt} \qquad (26)$$

The transients were fit with a generic decay function that comprised the compressed hyperbola and stretched exponential in this instance.[285]

$$I_{PL}(t) = Ae^{\frac{1-(1+\alpha\frac{t}{\bar{\tau}_0})^\beta}{\alpha\beta}} \qquad (27)$$

Dimensionless parameters are represented by α and β. Also seen in **Figure 24** are the fittings. Adding tin causes flaws that boost nonradiative recombination and shorten the average decay period, which drops from 63 ns to 3.3 ns. A change in voltage and a drop in carrier density might result from the capture and accumulation of photogenerated carriers at defects. In addition, the eventual release has the potential to extend the duration of processes. One reliable measure of the carrier dynamics in perovskites is the photoluminescence lifespan. Optoelectronic devices benefit from photogenerated carriers that have a long photoluminescence lifetime because these carriers can remain excited for longer, as they encounter fewer nonradiative paths. Alternatively, a shorter PL lifespan, as observed in the Pb-Sn structure, suggests that carriers recombine more rapidly, often before being effectively utilized for charge transfer or emission.

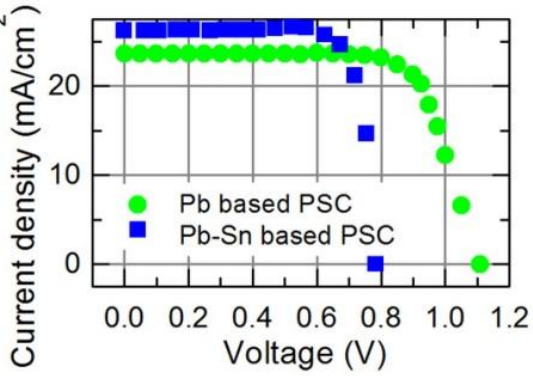

Figure 25. Results of white light irradiance at 100 mW/cm^2 for solar cells made on Pb-based and Pb-Sn-based perovskite films in terms of current-voltage.

Besides other device characteristics, the PCE of PSCs is also affected by the lifetime of the photogenerated charge carriers, with a strong dependency. The greater the lifetime of these carriers, the more likely they are to be captured at the electrodes before recombination, thus producing a larger current and higher efficiency. **Figure 25** presents the current-voltage characteristics of the best-performing PSCs, made with and without Sn incorporation in the perovskite absorber layer. To facilitate more comprehensive comparisons, the V_{oc}, J_{sc}, FF, and PCE corresponding photovoltaic characteristics are outlined in Table 1.

Table 1. Pb and lead-Sn combine with PSC: a few key factors for photovoltaics include PCE, FF, V_{oc}, and J_{sc}.

Perovskite Solar Cell	V_{oc}, V	J_{sc}, mA·cm^{-2}	FF, %	PCE, %
Pb based	1.11	23.6	73	19.1
Pb-Sn based	0.785	26.2	70	14.4

According to the J-V curves, it is evident that Pb-based PSCs exhibit larger values of PCE compared to their Pb-Sn mixed counterparts. The apparent disparate performances have been primarily ascribed to the superior open-circuit voltages of the Pb-based perovskite cells. A significant band gap results in higher V_{oc} in such devices due to the formation of larger potential differences across the illuminated cell.

The non-radiative recombination rate is also another influential element of the PCE. The non-radiative recombination is relatively weaker in the Pure

Pb-based perovskite films than in the mixed Pb-Sn films. Reduced non-radiative recombination means that fewer charge carriers are lost before they can be collected, leading to improved device efficiency. Regarding Pb-based PSCs, the achieved PCE of 19.1 is not high and is even below the average of the standard range of triple cation perovskite solar cells, which are usually reported to be between 16.5% and 19.2%.

On the other hand, there is variability in the performance of mixed Pb-Sn triple cation perovskite solar cells, as the PCE varies between 14% and 18% depending on the actual Sn content, film, and measurement conditions. The insertion of tin into the perovskite lattice, although potentially promising for tuning the band gap and expanding the absorption spectrum, tends to introduce additional non-radiative defect states. Such defects serve as recombination centres, thereby increasing both the bulk recombination rate and the surface recombination rate. Thus, a rise in the loss process by a non-radiative mechanism generates carriers, causing the overall device efficiency to decrease.

Furthermore, a weak peak is observed at a 2 theta angle of approximately 25.5 degrees, marked by a plus sign in both patterns. This reflection is attributed to the anatase TiO_2 plane, which is typically deposited on the FTO substrate as a dense layer used as an ETL in device stacks. The presence of the TiO_2 peak also indicates that the device is stratified and that the integration of this functional layer was successfully achieved during the fabrication process.

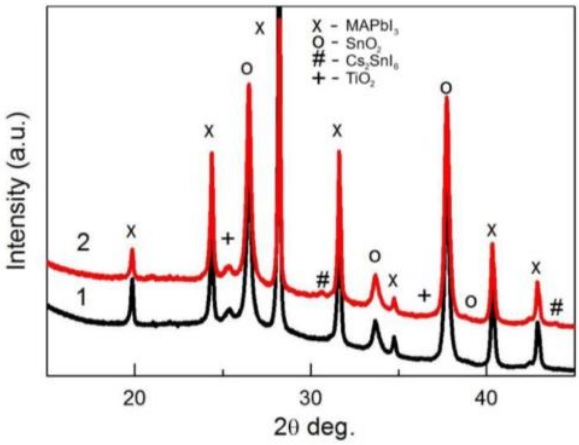

Figure 26. The XRD patterns of perovskite films on TiO_2/FTO/glass substrate: pattern 1 (black)—without Sn; pattern 2 (red)—with the addition of 20% SnI_2. Patterns were measured using the Bragg-Brentano method.

The XRD patterns of two perovskite films are shown in **Figure 26**. Pattern 1 (black curve) was prepared using a precursor solution with only PbI_2 (no SnI_2), and pattern 2 (red curve) was prepared using a precursor solution with 20% SnI_2 and 80% PbI_2. The XRD measurement employed the Bragg-Brentano geometry, a popular technique for phase identification and crystallographic characterization of thin film materials. This measurement not only provides vital structural data but also reveals the signatures of all the crystalline phases in the perovskite layer. Additionally, because it is a thin layer, it also detects signals from the underlying substrate and any interfacial layers. Both diffraction patterns exhibit strong peaks that can be indexed to the perovskite phase, i.e., $MAPbI_3$, as marked with the x symbols in the figure. The existence of these peaks proves the successful creation of the desired perovskite crystal structure in both samples. The location and relative intensity of these peaks can reveal information about the extent of crystallinity, preferred orientation (texture), and possible changes in lattice parameters resulting from compositional changes, such as partial substitution of tin. Remarkably, some of the peaks in both patterns are marked with the symbol o, which belongs to the SnO_2 phase. These are due to the underlying FTO substrate or due to a thin SnO_2 layer that was possibly deliberately deposited as an ETL before the perovskite deposition. These peaks in the XRD patterns indicate that the measurements are sensitive to both the perovskite layer and the substrate beneath it, due to the multilayered structure of PSCs. In the red pattern (pattern 2), a notable difference is that several small peaks, labelled with the symbol #, emerge. They are specific to the sample, including 20% $SnI_{2,}$ and are ascribed to the Cs_2 SnI_6 phase. These reflections indicate that a small portion of the precursor tin may crystallise into this secondary phase in addition to the primary perovskite phase under the synthesis conditions used. This secondary phase formation can impact the optoelectronic behaviour and device performance of the resulting device, as it can affect charge carrier recombination and provide a recombination centre or cause local inhomogeneity in the film.

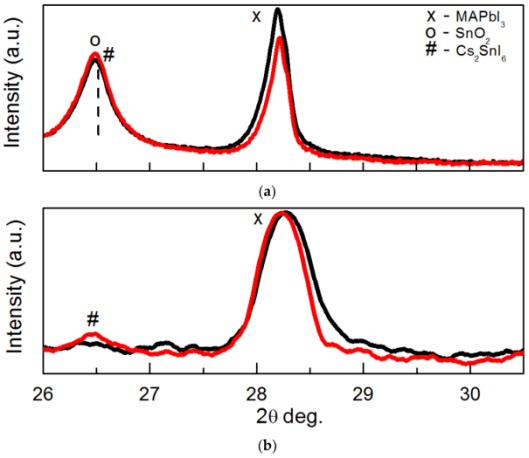

Figure 27. Bragg-Brentano (a) and GIXRD (b) measures of XRD pattern fragments. The black curves represent patterns of perovskites created without SnI_2, whereas the red curves represent patterns formed with SnI_2.

As **Figure 27a** indicates (scattered data in Bragg-Brentano geometry), the XRD patterns show that FTO and the perovskite layer have distinct peaks. In the case of Pb-based perovskite, the traces of only the (004) perovskite peak can be observed, which displays that there is no secondary phase. When SnI_2 was added to the precursor solution, however, some changes were noted. Most noticeably, the (004) perovskite peak shifts in smaller angles to the right of the diffraction. This change can be explained by a partial replacement of tin ions (Sn and Sn_2^+) in the perovskite lattice, which projects the lead ions (Pb_2^+). The smaller ionic radius of Sn_2^+ as compared to that of Pb_2^+ causes this replacement to result in the contraction of the lattice, especially on the c-axis, causing the lattice parameter c to change and the diffraction peak to shift out to higher angles. Also, in the case of the sample with SnI_2, XRD patterns show not only the perovskite (004) peak but another peak that represents the Cs_2SnI_6 phase. This means that a secondary phase was formed as a result of the addition of tin, which is not found in the pure Pb-based perovskite sample.

Figure 27b shows the XRD patterns obtained under different scan geometries, with the same 2θ range scanned. The perovskite (004) peak of the Sn-containing sample is shifted to lower diffraction angles in comparison with the pure Pb-based perovskite. Such an inversion dog should lead to a rise in the lattice parameter c. In the given case, the losses of smaller cations (Cs^+, Sn^{4+}, and I^-) during the formation of the Cs_2SnI_6 phase may result in a

general decrease in stoichiometry and, consequently, a reduction in lattice volume in one or several directions.

Figure 28 shows the TPV decay of PSCs prepared using two absorber layers. These TPV measurements are taken under carefully controlled experimental conditions: the devices are excited with a pulsed laser, with an incident power density of 0.6 mW/cm^2 in the case of the Pb-based PSCs and 0.8 mW/cm^2 in the case of the Pb-Sn-based PSCs. In both panels, the cyan trace represents the actual shape of the laser pulse itself, illustrating the sudden, short-duration excitation event. Will we measure a high Photovoltage in the device, which will decay back to baseline immediately after the laser pulse, as the excess carriers recombine or are swept out. **Figures 28(a) and (b)** display the TPV decay on a microsecond scale in Pb-based and Pb-Sn-based devices, respectively. The first photovoltage response is steep, and it peaks nearly instantly following the laser excitation. A slow decline in photovoltage then follows, indicating the recombination and extraction of photogenerated charge carriers within the device. This slower decay emphasizes that recombination processes in full device structures, where charge transport layers and interfaces are crucial, are more complex and may also involve long-lived electronic states, unlike isolated film PL measurements.

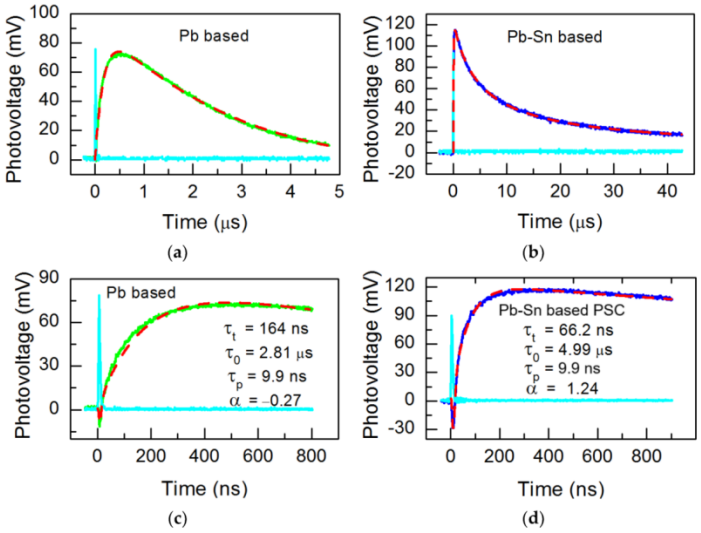

Figure 28. The transient photovoltage decay observed in solar cells constructed from Pb-based materials (**a**,**c**) and Pb-Sn-based (**b**,**d**) perovskite films. Excitation laser power density is 0.6 mW/cm^2 for Pb-based PSC and 0.8 mW/cm^2 for Pb-Sn-based PSC; the laser pulse is shown in cyan.

A closer look at the initial steps of the photovoltage decay on the nanosecond timescale is provided in Figures (c) and (d), along with the kinetic parameters obtained by curve fitting. In the case of the Pb-based device (**Figure 28c**), the decay could be modelled with several time constants: fast ($\tau_p \approx 9.9$ ns), slower ($\tau_t \approx 164$ ns), and long-lived ($\tau_0 \approx 2.81$ us), with an extra fitting parameter ($\alpha \approx -0.27$). In the case of the Pb-Sn-based PSC (**Figure 28d**), one has $\tau_p \approx 9.9$ ns, $\tau_t \approx 66.2$ ns, $\tau_0 \approx 4.99$ us, and $\alpha = 1.24$**.** The existence of a multi-time constant and the need for such fitting models suggests that the TPV decay behaviour is comprised of at least two distinct decay components: a fast and a slow component. The former (fast) is most often associated with the rapid relaxation of HC and recombination that occurs instantaneously. In contrast, the latter (slow) is related to the extraction and recombination of thermalized carriers in bulk and at interfaces. The photovoltage is composed of at least two distinct components, as shown in **Figures 28c and d**. The fast component is created almost instantly, no later than in a carrier energy relaxation time, and in many semiconductors, that is, a picosecond 10^{-12}s). Such a high speed of signal can be explained by the existence of so-called hot carriers, i.e., electrons and holes, which have already absorbed the energy of photons but have not yet reached thermal equilibrium with the lattice. These hot carriers may diffuse or drift between the junctions before relaxing (thermalizing) to generate a transient photovoltage. This fast component has been observed to possess a polarity opposite to the older, conventional slow photovoltage. Fast, hot carrier-induced photovoltage and the reversed polarity of this photovoltage have also been experimentally demonstrated. For instance, Gradauskas et al. observed a hot carrier photovoltage that was coupled simultaneously with a conventional generation-induced photovoltage in GaAs pn junctions under pulsed laser excitations [286]. They state: This hot carrier photovoltage is as fast as it is conditioned by the free carrier energy relaxation time (10^{-12}s). In contrast, the thermal one, which is determined by the change of the junction temperature, is much slower. Both of them have opposite signs compared to each other due to the generation of electron-hole pairs. Transport of the components in a state of simultaneous coexistence is supported experimentally in GaAs p-n junction irradiated with a pulsed 1.06 μm laser light." It is the slow part that results from the ordinary generation of electron-hole pairs and their separation in the built-in electric field across the p-n junction. This occurs after carriers cool to the band edge and, as such, is carrier lifetime, recombination, and diffusion limited. It is common to observe this process on a timescale ranging from nanoseconds to

microseconds. Indeed, the article by Masalskyi specifies that the hot-carrier photovoltage appears before the carriers become thermalized, and its polarity is exactly the opposite of the classical photovoltage [287]. Such an effect is intrinsic and presents an inherent loss process in classical p-n junction solar cells that impedes maximum performance. These two components and their physical origins are reflected in the time-resolved records of the transient experiments using perovskite and conventional semiconductors, both in evidence and in their signatures in the voltage transients. Hot carrier effects have now been persuasively attributed to the fast photovoltage component in most photovoltaic materials, both theoretically and experimentally. It exhibits ultrafast dynamics, a distinctly different physical mechanism, and negative polarity, compared to the classical photovoltage, which is replicated in various material systems, including silicon, GaAs, and perovskite solar cells. This two-phase, polar-opposite dynamic is now a crucial factor in modeling and optimizing high-end photovoltaic applications.

$$U = U_f + U_{ph} \tag{28}$$

Following the laser pulse, which is shown by a cyan-colored peak in all areas of **Figure 28**, the first component, denoted by the letter U_f, is the fast photovoltage component that has a negative polarity. This component is produced as a consequence of the heating of free carriers, which is triggered by laser radiation. The second component of photovoltage, known as U_{ph}, is a slow rate. It is possible to represent the form of U_f in a manner that is very similar to the shape of the laser pulse.

$$U_f = K_f I_p (\frac{\tau}{\tau_p})^4 \exp[-4\left(\frac{\tau}{\tau_p} - 1\right)] \tag{29}$$

In this particular context, the term "Ip" is used to designate the peak intensity of the laser, whereas the term "τp" is defined as the rise time of the laser. The coefficient k_f is determined from the measurements that were taken in the experiment. The second component of photovoltage, known as U_{ph}, is a slow component. The formation of electron-hole pairs is the primary cause of the photovoltage typically observed. The form that it takes can be expressed this way:

$$U_{ph} = U_o (\frac{e^{\frac{-t}{\tau t}} - e^{\frac{-t}{\tau rec}}}{\frac{1}{\tau rec} - \frac{1}{\tau t}}) \tag{30}$$

In this particular context, the term U_0 is used to designate the initial photovoltage. In contrast, the term τ_t is used to indicate the time constant associated with electron transport inside the perovskite layer. Additionally, the term τ_{rec} is used to refer to the time required for carrier recombination.

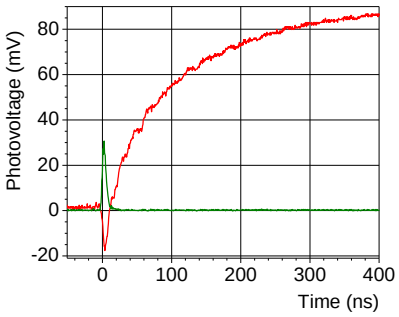

Figure 29. Temporal shapes of the laser pulse (green) and photovoltage (red) of the PSC. Excitation laser power density: 0.8 mW/cm^2.

When cesium-based triple-cation perovskite solar cells (PSCs) are exposed to a laser pulse (7 ns duration, 532 nm), the transient photovoltage (TPV) signal they produce demonstrates even greater complexity than the steady-state open-circuit voltage. To investigate how hot-carrier effects may occur in other band-structure landscapes, we examine two compositions of absorbers, with pure lead perovskites, $Cs_x(FA_{0.83}MA_{0.17})_{(1-x)}Pb(I_{0.83}\ Br_{0.17})_3$ and their alloyed counterparts, $Cs_x(FA_{0.83}MA_{0.17})_{(1-x)}Pb_{0.8}Sn_{0.2}(I_{0.83}\ Br_{0.17}\ )_3$.

In **Figure 29**, it is shown that the 7 ns laser pulse (green trace) is overlaid with the measured TPV (red trace). When the light is switched on, a fast spike of voltage is observed, rising and decaying on the same timescale as the optical pulse, followed by a slow second process of voltage build-up and decay. This fast component is explained by a hot carrier electromotive force. When the light is immediately absorbed, the carriers are swept out of thermal equilibrium and diffuse across the junction, producing a transient thermoelectric voltage of opposite polarity. As soon as these carriers thermalize (in a few picoseconds to nanoseconds)

Predominantly reflecting the classical photovoltage. The simultaneous occurrence (and inversion of signs) of these two signals emphasizes the presence of an intrinsic loss process in PSCs, related to hot-carrier effects, that can partly eliminate the desirable photovoltage and thereby restrict the power-conversion efficiency. This paper directly demonstrates, via the time domain, that hot-carrier EMF exists in perovskites and provides crucial evidence on how carrier heating must be controlled in next-generation devices.

The slope of the V_{oc} of the PSC against the log of incident light intensity is conveniently helpful in having an idea of the recombination processes that prevail in the device. In particular, the study of this relationship allows for

estimating whether recombination is mainly monomolecular, bimolecular, or Auger (see **Figure 30** for the experimental data).

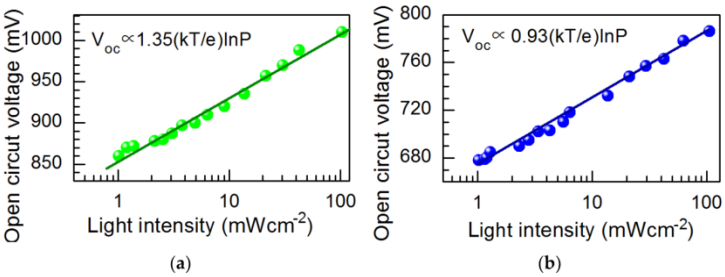

Figure 30. The relationship between the white light intensity and the open circuit voltage Voc in solar cells made on Pb-based (a) and Pb-Sn-based (b) perovskite films.

Figure 30 shows the association of the V_{oc} of the Incident White Light (P) of two distinct varieties of PSCs, viz., the ones that operate on a single-composition pure Pb and those that use a combined Pb-Sn mixture composition in their perovskite absorption layers. From the data, it is evident that the V_{oc} of the Pb-based PSCs will always be higher compared to the values measured in the mixed Pb-Sn devices under otherwise similar illumination conditions. This difference in Vocs can be explained mainly by two main factors: the smaller bandgap of the Pb-Sn perovskite substance and the even more substantial prevalence of surface recombination among such films. The smaller forbidden energy band gap of the Pb-Sn perovskite also contributes to a reduced theoretical maximum V_{oc} because the energy band gap of the absorber material inherently limits the open-circuit voltage of a solar cell. Additionally, the mixed Pb-Sn perovskite films are prone to increased surface recombination, which further lowers the possible V_{oc}. Surface recombination occurs when charge carriers, i.e., electrons and holes generated by light, recombine at the surface or other interfaces of the perovskite film before the component charges can be collected, thereby causing unnecessary losses and decreasing the overall device performance. Surface recombination responds to the device's operation, as also indicated by the dependence of Voc on illumination intensity observed. This numerical value is represented by the slope of the graph when Voc is plotted against the log scale of the light intensity. In the case of the Pb-Sn perovskite solar cells, this slope is 0.93 k_BT/e. As such, this smaller bandgap, combined with increased surface recombination, explains the observed decrease in V_{oc} of the mixed Pb-Sn perovskite solar cells compared to their pure Pb-based

counterparts. These results demonstrate that the material composition, as well as the surface passivation strategies of perovskite solar cells, should be optimized to reduce recombination losses and improve the efficiency of Pb-Sn perovskite solar cells.

The slope of v_{oc} vs. log light intensity of our samples of perovskite solar cells we measured proved to be very near one. It is observed that this observation is highly indicative of the proposed mechanism, namely bimolecular recombination, which is the predominant limiting open-circuit process in these devices. When using the terminology of solar cell physics, a slope of unity is indicative of a case where recombination proceeds via two charge carriers (an electron and a hole), which is typical of bimolecular recombination. This is in contrast to a slope of nearly two, which would imply that monomolecular or trap-assisted recombination is more predominant. Based on this experimental result, we also revised our theoretical model, which describes the V_{oc} dependence. Specifically, we rearranged the form of Equation (25) to more closely align it with the experimental data by introducing an additional factor that describes a hyperbolic decay. This substitution takes into account the effect of bimolecular recombination, allowing for a more accurate description of the Voc observed under different illumination strengths. The nonlinearity of the recombination kinetics in the perovskite layer is achieved by using a hyperbolic decay function, specifically one where the recombination rate varies as the square of the carrier concentration.

$$U_{ph} = U_o\left(\frac{e^{\frac{-t}{\tau_t}} - \left(1+\alpha\frac{t}{\tau_o}\right)^{\frac{-1}{\alpha}}}{\frac{1}{\tau_o} - \frac{1}{\tau_t}}\right) \qquad (31)$$

The time constant at $t = 0$ is denoted by τ_0, while α is a parameter that does not have any dimensions. If the value of α is less than 1, equation (31) transforms into a compressed hyperbola. If α is more than 1, the hyperbola is stretched. If α is less than zero, the integrated result is zero at a finite value of t. **Figure 30** depicts the results of the fitting, which were computed in accordance with Equations (29) and (31). These results are depicted as dashed lines. Given the relatively small electric field that is present in this setting, the mobility of excited charge carriers inside perovskite films is primarily driven by their diffusion through the material. Given that D represents the bipolar diffusion coefficient and L represents the thickness of the film, it can be concluded that τ_t is approximately equivalent to the ratio of L^2/D. Perovskite films based on lead and mixed perovskite films, including those with lead and tin, are expected to have D values of 0.04

cm^2/s and 0.15 cm^2/s, respectively. The spin-coated perovskite films often have values of D that are similar to these [90, 146, 151, 288, 289].

The formation of electron-hole pairs is the primary cause of the typical photovoltage observed. It can be observed that the PCE of the PSCs based on lead-sn is lower (14.4%) than that of the PSCs based on lead (19.1%). The high PCE of the Pb-based perovskite sample is primarily determined by the high value of the open-circuit voltage, which is the result of a higher forbidden energy gap compared to the Pb-Sn-based perovskite sample.

A formulation of the thesis can be derived from these observations: The fast component, U_f, follows the shape of the laser pulse and is caused by the heating of charge carriers by light. The slow component will be the typical photovoltage produced as a result of the creation of electron-hole pairs. The polarity of U_f is the opposite of that of conventional photovoltage, which means that the hot charge carriers can be another factor that restricts the PCE of PSCs.

3.6. Triple-cation perovskite/silicon tandem solar cell

This paper represents a thorough study of the photovoltaic characteristics of an innovative four-terminal tandem solar cell structure. The studied device has the triple cation perovskite/silicon structure, where the top sub-cell has a semitransparent perovskite film with the composition of $Cs_{0.06}(MA_{0.17}FA_{0.83})_{0.94}Pb(I_{0.83}Br_{0.17})_3$. It is this perovskite solar cell that is carefully placed on top of another type of solar cell, an industry-grade, n-type monocrystalline bifacial PERT silicon solar cell, which forms the bottom sub-cell. The resulting tandem device can achieve high performance by combining the optoelectronic characteristics of a triple cation perovskite, which is enhanced in both thermal and phase stability, with the well-known efficiencies of bifacial PERT silicon cells. Schematics of the perovskite solar cell are shown in **Figure 31**.

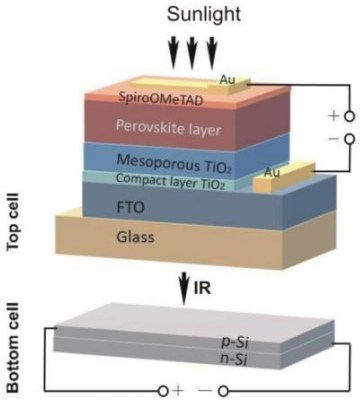

Figure 31. A triple-cation perovskite/silicon tandem solar cell was designed. The silicon cell at the bottom is grey.

This has the advantage that the perovskite layer is semitransparent, allowing light to pass through to the silicon cell below in sufficient quantity to make the best use of the entire solar spectrum. This design also permits the two sub-cells to be operated independently in a four-terminal cell, rather than in a half-cell pairing. Consequently, due to this synergetic design, the tandem solar cell has a superior PCE of 26.6. This efficiency also establishes one of the highest reported efficiencies to date for four-terminal perovskite/silicon tandem solar cells, demonstrating the viability of perovskite/silicon tandems as a future high-efficiency photovoltaic technology. The excellent performance promises promising prospects for this type of tandem structure in solar energy conversion, meeting the growing demand for renewable energy resources. In the fabrication of the perovskite/silicon tandem solar cell, we used a commercially available bottom sub-cell, which is an n-type monocrystalline bifacial PERT silicon solar cell (DS New Energy, China, **Figure 32**).

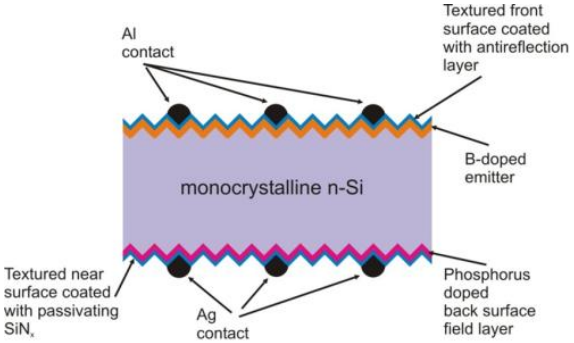

Figure 32. The silicon SC, which is the bottom cell of the perovskite/silicon tandem solar cell, is shown in a schematic cross-sectional perspective.

This is a state-of-the-art silicon cell architecture specifically designed to achieve very high performance and efficiency, enabling it to be integrated into tandem architectures. The PERT silicon solar cell consists of a monocrystalline n-type silicon wafer, which serves as the primary light-absorbing and charge-transporting region in the solar cell. The face of the silicon wafer is textured so that reflection is avoided and the amount of light incident is absorbed as much as possible. This textured surface is then enhanced with an additional layer of antireflection coating, which traps light and increases the device's overall efficiency. A p^+ emitter layer is added to the top surface of the n-type silicon substrate by diffusion using Boron.

Furthermore, it achieves perfect electrical compatibility and matching with the top perovskite cell in the two-cavity tandem scheme, enabling the charge extraction and transfer process between the two sub-cells to be highly effective. To further enhance surface passivation and minimize carrier recombination losses, a thin layer of SiN is deposited on the front textured surface. This layer further helps in decreasing the reflection of the surface. Electrical contacts made of aluminium (Al) are well-located on the front side to collect the generated electrical current and transport it.

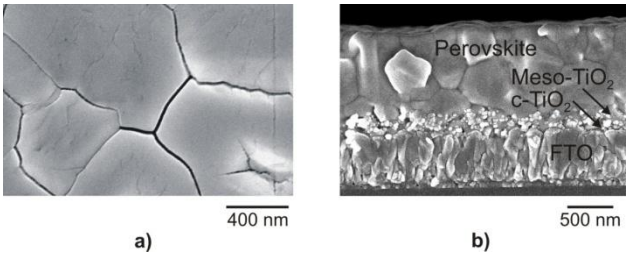

Figure 33. Surface SEM image (a) and cross-sectional SEM image (b) of the perovskite layer formed on mesoporous titanium dioxide.

Figure 33a exhibits a top-view SEM photograph of the triple cation perovskite membrane that is placed on a mesoporous TiO_2 layer. The picture illustrates the polycrystalline structure of the perovskite film, with an unambiguous presence of grain boundaries and a noticeable variation in grain size throughout the surface. It is observed that a few grains of perovskite exceed 1000 nm in lateral dimensions, indicating the successful growth and coalescence of grains during the film growth process. The surface morphology is exceptionally flat and smooth, which concurs with the high-quality films reported in the literature. These smooth surfaces are advantageous for charge conduction, as well as for minimizing charge

recombination losses at the interface. Therefore, the resulting solar cell devices perform better.

The SEM cross-sectional image of the multilayer perovskite solar cell stack, as shown in **Figure 33b**, provides further insight into its structure and morphology. The thickness of the perovskite layer is seen to be a constant value of about (710±40) nm, which denotes the uniformity of the deposition that took place during the process. In the cross-section, it is identified that the film is composed of stacked perovskite grains, although the grains are not within the full thickness of the layer. They are instead positioned in columns or clusters, thus creating grain boundaries that expand vertically throughout the film. This structural feature may be essential in charge carrier dynamics, as the existence of vertically oriented grain boundaries may promote or hinder carrier movement based on crystallographic orientation or due to defects. The underlying layers are well characterized, as it can be observed that there is a mesoporous TiO_2 (meso-TiO_2) scaffold, a compact TiO_2 (c-TiO_2) blocking layer, and an FTO substrate, which is a conducting glass. In general, the SEM analysis revealed that the triple cation perovskite films produced during the present research work possess the necessary structural features, including sizable grain sizes, smooth surfaces, and well-defined layer boundaries. The highlighted characteristics should play a positive role in the photovoltaic operation of tandem solar cell devices.

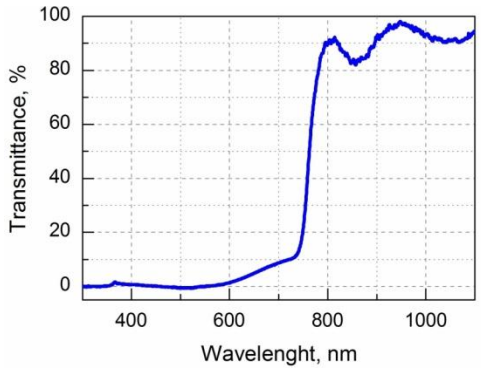

Figure 34. The perovskite layer with triple cations and its optical transmittance spectrum.

Figure 34 shows the transmittance spectrum of the perovskite layer measured by the researcher. The data show that the perovskite film exhibits excellent absorption properties in the visible spectrum, with transmittance values remaining close to zero until the wavelength reaches approximately 750 nm and above. This poor transmittance indicates that the perovskite

material effectively captures the majority of the visible light entering the material, thereby revealing it to be the primary light absorber in the photovoltaic device. Beyond 750 nm, the transmittance rates increase significantly, indicating the onset of semitransparency in the near-IR. Between 800 and 1100 nm, the transmittance increases significantly and remains above 80%. Such a high magnitude of transmittance in the near-infrared indicates that the perovskite layer does not absorb most of the infrared light but transports it. These optical characteristics are beneficial for tandem solar cell applications. Effective absorption in the visible part of the spectrum and high transmittance in the near-infrared ensure the efficient utilization of the most energetic part of the solar spectrum, with photons of longer wavelengths reaching the silicon sub-cell beneath. This enables the tandem structure to collect extra solar energy that would otherwise be lost, thus boosting the device's efficiency.

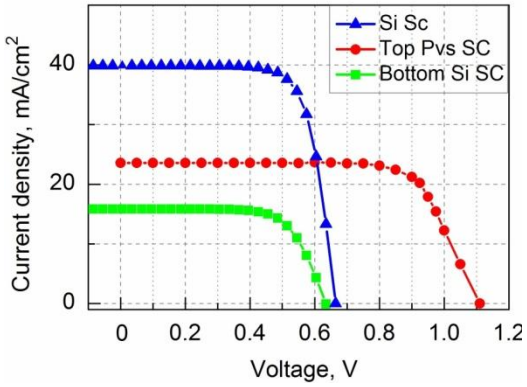

Figure 35. Under 100 mW/cm^2 light, current-voltage characteristics of triple cation perovskite (red points) and silicon (blue points) solar cells are shown, and green dots indicate the current-voltage characteristics of the Si cell.

Figure 35 shows the measured J-V characteristics of the fabricated triple-cation perovskite solar cell, as indicated by the red circles in each panel. This perovskite solar cell exhibits a high Jsc, which is a strong indication of the excellent optoelectronic quality and efficient photon absorption capacity of the perovskite layer, making it a promising material for solar energy applications. This high Jsc indicates an efficient generation and collection of charge carriers, as it is optimized in terms of the structure and defect concentration of the perovskite film. In **Table 2**, along with the J-V curve, the significant photovoltaic parameters of the triple cation perovskite solar cell are tabulated, including V_{oc}, J_{sc}, FF, and PCE. Such

metrics are essential for assessing the device's performance and comparing it to other photovoltaic technologies.

Table 2. Photovoltaic parameters of the perovskite solar cell separate it from the silicon solar cell, which serves as the bottom cell in the tandem cell.

Solar cell	V_{oc}, V	J_{sc}, mA·cm^{-2}	FF, %	PCE, %
Top perovskite SC	1.11	23.6	74	19.4
Separate Si SC	0.67	40.0	72	19.3
Bottom Si SC	0.64	15.8	71	7.2

For comparison, **Figure 35** also shows the I-V curve of a standard industrial silicon solar cell, measured under AM1.5G standard illumination (100 mW/cm²), using blue triangles. As it has been found, the silicon solar cell alone has a significantly higher short-circuit current density than the perovskite device, which is explained by its wider absorption spectrum that extends into the near-infrared region. Table 2 also provides the photovoltaic parameters of the stand-alone silicon solar cell, which will be used as a reference. The high power conversion efficiency and semitransparent quality of the triple cation perovskite solar cell is an excellent choice to form part of a 4T tandem design alongside a commercial silicon solar cell as the bottom sub-cell. **Figure 35** shows the current-voltage characteristic of the bottom silicon cell in a tandem-proposed structure, plotted by green squares. When placed above, the perovskite cell absorbs most of the incident photons with wavelengths falling within the visible spectrum, resulting in a substantial decrease in the short-circuit current density of the silicon cell behind it. The total PCE of the overall device is a remarkable 26.6%, achieved by combining the efficiencies of the four-terminal tandem structure of the two sub-cells. This is the total of the PCE (19.4 %) of the semitransparent perovskite top cell and the PCE (7.2 %) of the bottom silicon cell. The findings demonstrate the potential of semitransparent triple cation perovskites/silicon four-terminal tandem solar cells to play a superior role in photovoltaic developments, ultimately enhancing the efficiency of solar energy conversion.

4. CONCLUSIONS

- Transient photovoltage in single-junction perovskite solar cells exhibits two oppositely polarized components: a rapid negative part driven by hot carriers resulting from carrier heating and a slower positive contribution caused by the traditional generation of electron-hole pairs. This behaviour of the two components indicates that the hot carriers have adverse effects on photovoltage, thereby lowering the overall power conversion efficiency of single-junction perovskite solar cells.
- Stacking wide-bandgap perovskite cells on top of narrow-bandgap cells (e.g., silicon) allows the top cell to absorb high-energy photons and pass the low-energy photons that were absorbed. Tandem solar cells reduce thermalisation losses and increase the practical utilisation of the solar spectrum, resulting in increased total efficiency. Carrier lifetimes can be increased and recombination losses reduced by lowering defect density (particularly upon alloying perovskites with other metals) and by interface optimization to improve both the voltage and current outputs of perovskite solar cells.
- The existence of potential barriers caused by band bending at charge transport layers further contributes to the development of the hot carrier thermoelectromotive force, which is detrimental to the device's efficiency. The elimination or weakening of these possible barriers, such as flat-band conditions, removes the thermoelectromotive force and thereby enhances the device's performance.
- The addition of tin (Sn) in perovskite films decreases the bandgap. It contributes to the creation of non-radiative defects, which increase the recombination rates on the surface and significantly decrease the photoluminescence lifetime. These kinds of structural modifications deteriorate the photoelectric behavior of perovskite solar cells and reduce their total power conversion efficiency relative to those composed of pure lead-based perovskites.
- Experimental analyses have already demonstrated that using perovskite/silicon tandem solar cells can lead to significant advances in power conversion efficiencies that surpass the limits of single-junction cells. A four-terminal tandem solar cell architecture, constructed from a silicon bottom cell and a spectrally semi-transparent triple-cation perovskite top cell, achieved a combined efficiency of 26.6% (19.4% from the semi-transparent perovskite top cell and 7.2% from the bottom silicon cell). That

surpassed the individual efficiency of the standalone perovskite and silicon cells. This demonstrates the efficiencies and importance of multi-junction schemes in overcoming the drawbacks caused by both hot-carrier effects and thermalization losses.

SUMMARY IN LITHUANIAN

ĮVADAS

Saulės energija atsirado ir tapo svarbia alternatyva įprastiems iškastinio kuro energijos šaltiniams, reaguojant į augančią pasaulinę energijos paklausą ir poreikį švelninti aplinkosaugos problemas, įskaitant taršą ir klimato kaitą. Augant susidomėjimui atsinaujinančios energijos sistemomis, saulės fotovoltinė (FV) technologija išsiskiria savo gebėjimu tiesiogiai paversti saulės energiją elektra neteršiant aplinkos ir neeikvojant gamtos išteklių. Perovskito saulės elementai (PSC) tarp įvairių fotovoltinių technologijų sulaukė didelio tyrėjų dėmesio dėl išskirtinių optoelektroninių savybių, ekonomiško apdorojimo, paprasto gamybos proceso ir sparčiai gerėjančio energijos konversijos efektyvumo (PCE). Perovskito junginių istorija siekia 1839 m., kai vokiečių mineralogas Gustavas Rose pirmą kartą identifikavo kalcio titanatą ($CaTiO_3$) ir pavadino jį rusų mineralogo Levo Perovskio garbei. Nepaisant intensyvių perovskito darinių tyrimų įvairiose srityse, įskaitant katalizę, superlaidininkus ir feroelektrikus, jis ilgai nebuvo panaudotas FV technologijoje.

Reikšmingas žingsnis į priekį buvo žengtas 2009 m., kai Kojima ir kt. aprašė praktinį metilamonio švino jodido ($MAPbI_3$), kaip aktyvios fotovoltinės absorbuojančios medžiagos, turinčios daug žadantį pradinį efektyvumą, pritaikymą. Šis proveržis sukėlė didelį mokslininkų susidomėjimą, to pasekoje buvo aktyviai plėtojama perovskito saulės elementų technologija.

Trigubų katijonų perovskito dariniai pasižymi geresniais našumo rodikliais, ypač tandeminėse saulės elementų (TSC) topologijose. Jose naudojamos įvairios FV medžiagos, siekiant sukaupti daugiau saulės šviesos, taip padidinant bendrą saulės elementų efektyvumą, viršijantį vienos jungties įrenginių ribas. Įtraukus trigubų katijonų perovskitus į tandeminius saulės elementus reikia atlikti sudėtingas gamybos procedūras. Norint pasiekti optimalų našumą, būtina kruopščiai reguliuoti kiekvieno perovskito sluoksnio sudėtį, storį ir vienalytiškumą. Be to, siekiant optimizuoti efektyvumą ir stabilumą, būtina suprasti sudėtingą krūvio pernašos dinamiką ir rekombinacijos procesus šiuose naujuose perovskito dariniuose.

Disertacijoje nuodugniai nagrinėjamos pagrindinės problemos, atsirandančios siekiant pagaminti ir ištirti trijų katijonų perovskito darinius, skirtus tandeminių saulės elementų taikymams. Jų gamyba apima integravimą sudėtingų nusodinimo procesų, tokių kaip purškiama pirolizė elektronų pernašos sluoksniams (ETL) nusodinti ir sukimosi padengimo

metodas perovskito dariniams ir skylių pernašos sluoksniams (HTL) nusodinti. Eksperimentai apima optinių ir elektrinių charakteristikų matavimus, įskaitant absorbcijos ir pralaidumo spektroskopiją, pereinamųjų fotoįtampos procesų registravimą ir kruopščius FV elementų veikimo tyrimus.

Šio darbo tikslas – susintetinti trijų katijonų perovskito darinius ir išsamiai ištirti jų optoelektronines savybes bei sukurti didelio našumo tandeminius saulės elementus.

Tikimasi, kad šių tyrimų rezultatai gerokai paspartins efektyvių, stabilių ir komerciškai perspektyvių perovskito trigubų katijonų tandeminių saulės elementų kūrimą. Tai tiesiogiai prisideda prie pagrindinio tikslo – pereiti prie atsinaujinančių ir tvarių energijos sistemų, sprendžiant esminius pasaulinius energetinio saugumo ir aplinkos tvarumo klausimus. Šiame darbe daug padaryta, siekiant praktinio ir plataus pažangių FV technologijų diegimo atsinaujinančiosios energijos sektoriuje.

Tyrimo projekto uždaviniai

Sukurti ir patobulinti trijų katijonų perovskito sluoksnių gamybos metodus.

Gaminti ETL(TiO_2) purškiamosios pirolizės ir sukimosi dengimo metodais.

Naudojant sukimosi dengimą inertinėje pirštinių dėžės aplinkoje pagaminti perovskito absorbcinius sluoksnius ($MAPbI_3$) ir skylių pernašos sluoksnius (Spiro-OMeTAD).

Išmatuoti perovskito sluoksnių absorbciją ir pralaidumą.

Nustatyti pagamintų saulės elementų energijos konversijos efektyvumą.

Išsamiai išanalizuoti gautus tyrimų rezultatus, nustatyti saulės elementų našumo apribojimus ir pasiūlyti patobulinimus.

GINAMIEJI TEIGINIAI

- Pereinamosios fotoįtampos matavimai vienos sandūros perovskito saulės elementuose leidžia aptikti karštųjų krūvininkų buvimą ir jų įtaką fotoįtampos generavimui. Fotoįtampa, indukuota saulės elementuose veikiant lazerio impulsiniam lazerio sužadinimui, susideda iš dviejų priešingo poliškumo komponenčių. Greitoji komponentė atsiranda dėl krūvininkų kaitinimo šviesa, ir jos forma atitinka impulso formą, o lėtoji yra tipinė fotoįtampa, susikurianti dėl elektronų ir skylių porų generacijos.

- Neigiamą karštųjų krūvininkų poveikį perovskito saulės elementų energijos konversijos efektyvumui galima sušvelninti sumažinant juostos išlinkimą šalia krūvio pernešimo sluoksnių arba naudojant daugiasandūrinius elementus, kurie geriau išnaudoja saulės spektrą ir sumažina nuostolius dėl šiluminės elektrovaros atsiradimo.
- Pridėjus alavo į švino halogenidų perovskito medžiagą saulės elementų energijos konversijos efektyvumas sumažėja dėl susiaurėjusios draustinių energijų juostos ir išaugusio nespindulinių defektų skaičiaus bei paviršinės rekombinacijos greičio.

NAUJUMAS IR AKTUALUMAS

Šioje disertacijoje aprašytas perovskito sluoksnių auginimas naudojant išbandytus ir pakartotus Burshkos ir kt. bei Salibos ir kt. metodus. Disertacijoje nagrinėjamos esamos žinių spragos ir išsamiai nagrinėjami fotofizikiniai mechanizmai vienos sandūros perovskito saulės elementuose. Pirmą kartą buvo nustatyta, kad apšvietus vienos sandūros perovskito saulės elementą trumpu lazerio impulsu, indukuota fotoįtampa susideda iš dviejų priešingo poliškumo dedamųjų. Greitoji dedamoji yra nulemta krūvininkų kaitimo šviesa, o lėtoji – fotoįtampa, susidaranti dėl elektronų ir skylių porų generacijos. Disertacijoje siūlomos strategijos, siekiant sušvelninti neigiamą karštųjų krūvininkų įtaką perovskito saulės elementų energijos konversijos efektyvumui. Visų pirma, siūloma kuo labiau sumažinti energijos juostos išlinkimą krūvio pernašos sąsajose arba naudoti daugiasandūrinius darinius, kad būtų naudingiau panaudotas visas saulės spektras ir sumažinti nuostoliai dėl termalizacijos.

Tyrimo rezultatai rodo, kad pridėjus alavo ir dėl to susiaurėjus draudžiamųjų energijų juostai bei išaugus nespindulinių defektų koncentracijai labai sumažėja energijos konversijos efektyvumas, kurį dėl išaugusių paviršiaus rekombinacijos greičių pagrindinai nulemia nepalankus poveikis atvirosios grandinės įtampai ir trumpojo jungimo srovei.

Disertacijoje pateikti tyrimo rezultatai išplečia esamą žinių bazę apie perovskito saulės elementų našumą ribojančius veiksnius ir pateikia įžvalgių minčių apie tai, kaip galima patobulinti elementų architektūrą ir sudėtį, siekiant įveikti šiuos iššūkius.

Mokslinių publikacijų sąrašas

P1. Asmontas S., Gradauskas J., Griguceviciene A., Leinartas K., Lucun A., Mujahid* M., Petrauskas K., Selskis A., Suziedelis A., Silenas A., and Sirmulis E., Triple-cation perovskite/silicon tandem solar cell, Ukrainian

Journal of Physical Optics (2022), Vol. 23, Issue 4, pp. 193 – 200. Q1 (IF: 3.9)

P2. Steponas Ašmontas, Muhammad Mujahid*, Recent Progress in Perovskite Tandem Solar Cells, Nanomaterials (2023), 13(12), 1886. Q2 (IF: 4.3)

P3. Muhammad Mujahid*, Aurimas Čerškus, Jonas Gradauskas, Asta Grigucevičienė, Raimondas Giraitis, Konstantinas Leinartas, Andžej Lučun, Kazimieras Petrauskas, Algirdas Selskis, Algirdas Sužiedėlis, Aldis Šilėnas, Edmundas Širmulis, Steponas Ašmontas. Unveiling the Influence of Hot Carriers on Photovoltage Formation in Perovskite Solar Cells, Materials 2025, 18(1), 85. Q2, (IF: 3.2)

P4. Muhammad Mujahid*, Jonas Gradauskas, Algirdas Sužiedelis, Edmundas Širmulis, and Steponas Ašmontas*, Recent Advancements in Understanding Hot Carrier Dynamics in Perovskite Solar Cells, Energies 2025, 18(13), 3543. Q3 (IF=3.2)

Konferencijos

C1. Muhammad Mujahid*, Steponas Ašmontas. Triple cation perovskite/silicon tandem solar cell, Apropos 18 Conference, Sauletekio av. 3 Vilnius, Lithuania, 5-7 October 2022.

C2. M.Mujahid*, Ašmontas S. Triple cation perovskite/silicon tandem solar cell, FizTech2022 conference, Sauletekio av. 3 Vilnius, Lithuania, 19 – 20 October, 2022.

C3. Muhammad Mujahid*. A Road Map to Perovskite Perovskite Tandem Solar Cells. 13th Conference of Doctoral Students and Young Scientists FizTeCh-2023, Sauletekio av. 3 Vilnius, Lithuania, 18 October 2023.

C4. S. Ašmontas, A. Čerškus, J. Gradauskas, A. Grigucevičienė, R. Juškėnas, K. Leinartas, A. Lučun, O. Masalskyi, M. Mujahid*, K. Petrauskas, A. Selskis, A. Sužiedėlis, E. Širmulis, Laser induced photoresponse in perovskite solar cells. International Conference, Laser Technologies. (LTLA 2023)“ June 29-30, 2023, Truskavets, Ukraine.

C5. Steponas Ašmontas, Jonas Gradauskas, Asta Grigucevičienė,Konstantinas Leinartas, Andžej Lučun, Muhammad Mujahid*, Kazimieras Petrauskas, Edmundas Širmulis, Algirdas Sužiedelis. Photovoltage formation in perovskite solar cell under laser excitation. The international APROPOS 19 conference. Sauletekio av. 3, Vilnius, Lithuania, 1-4 October 2024.

C6. Muhammad Mujahid*, Steponas Ašmontas. Investigation of Photovoltage Formation in Perovskite Solar Cells. FizTeCh 2024. Saulėtekio al. 3, Vilnius, 15-17 October, 2024.

C7. E. Širmulis, S. Ašmontas, A. Čerškus, J. Gradauskas, A. Grigucevičienė, R. Giraitis, K. Leinartas, A. Lučun, M. Mujahid*, K. Petrauskas, A. Selskis, A. Sužiedėlis, A. Šilėnas. Photoelectric behavior of perovskite solar cells excited with a nanosecond laser pulse. Truskavets, Ukraine, June 26-27, 2025.

Autoriaus indėlis

Tiesioginis autoriaus indėlis:

TiO_2 elektronų pernašos sluoksnių gamybos metodų tobulinimas ir plėtojimas purškiamosios pirolizės ir sukimosi padengimo procedūromis.

Perovskito sluoksnių ir skylių pernašos sluoksnių (Spiro-OMeTAD) gamyba inertinėje pirštinių dėžėje.

Tikslių optinių matavimų, įskaitant absorbcijos, pralaidumo, atlikimas ir efektyvumo vertinimus.

Išsami eksperimentinių duomenų analizė ir rezultatų interpretavimas.

Mokslinių straipsnių rengimas ir publikavimas bei reikšmingų išvadų pristatymas tarptautinėse ir FTMC organizuojamose mokslinėse konferencijose.

VYSTYMASIS NUO VIENKATIJONIŲ IKI TRIJŲ KATIJONIŲ PEROVSKITŲ

Švino halogenidų perovskito medžiagos yra reikšmingas proveržis šiuolaikinioje fotovoltaikoje. Archetipinį organinį-neorganinį (hibridinį) perovskitą galima apibūdinti kaip darinį ABX_3, kur A yra monovalentis organinis arba neorganinis katijonas, pvz., metilamonis (MA), formamidinis (FA) arba Cs^+, B yra dvivalentis metalo katijonas (Pb_2^+ arba Sn_2^+), o X – halogenidas (Cl^-, Br^-, I^-). Visame pasaulyje atlikta daug tyrimų, siekiant stabilizuoti įrenginius ir padidinti jų veikimo efektyvumą. Perovskito plėvelės atveju, norint pagerinti jos vidinį stabilumą, reikalingas idealus Goldšmito tolerancijos koeficientas ir oktaedrinis koeficientas. Tolerancijos koeficientą galima padidinti naudojant didesnį katijoną A. Didesnio B katijono panaudojimas sumažina tolerancijos koeficientą, tuo pačiu padidindamas oktaedrinį koeficientą. Perovskito sudėties keitimas yra viena iš strategijų, kurią galima panaudoti siekiant patvaresnio ir efektyvesnio perovskito saulės elemento. Įrenginio draudžiamųjų energijų juosta ir

absorbcija išlieka nepakitę, nepriklausomai nuo to, ar keičiamas A katijonų santykis, ar įvedami nauji A katijonai. Kita vertus, tai gali pagerinti našumą, padidinant arba sumažinant paviršiaus defektų kiekį ir padarant paviršius lygesnius su didesniais grūdeliais. Bet kokio santykio pakeitimas taip pat keičia oktaedrinį koeficientą ir Goldšmidto tolerancijos koeficientą. Todėl perovskite esantys katijonai (ir anijonai) gali pakeisti nuosavą stabilumą. Perovskito plėvelių gamybai tradiciškai buvo naudojami įvairūs formamidinio ir metilamonio santykiai. Norint gauti įrenginius su didesniu energijos konversijos efektyvumu, pastaruoju metu buvo naudojami nedideli rubidžio (Rb) ir Cs kiekiai. Palyginti su $MAPbI_3$, $FAPbI_3$ yra labiau kubinis dėl šiek tiek didesnio FA katijono joninio spindulio, maždaug 2,79 Å. Yra dvi skirtingos $FAPbI_3$ perovskito fazės: kubinė fotoaktyvioji fazė (α-$FAPbI_3$) ir šešiakampė nefotoaktyvioji fazė (δ-$FAPbI_3$). $FAPbI_3$ $FAPbI_3$ perovskite dėl didesnių ir netolygesnių riebalų rūgščių grupių yra didelė fazės nestabilumo problema. Dėl to kambario temperatūroje jis keičia savo būseną iš α-$FAPbI_3$ fazės į δ-$FAPbI_3$ fazę, o tirpikliai ir drėgmė dar labiau jį veikia.

TRIJŲ KATIJONIŲ PEROVSKITAI

Neseniai centrifuginio dengimo metodu buvo susintezuoti trijų katijonų mišrių halogenidų perovskitų monokristalai. Iš pradžių, $MAPbBr_3$ prekursoriaus dalį pakeitus $CsPbBr_3$, buvo pagaminta mišrių katijonų/halogenidų perovskitų seka $(FAPbI3)_{1-x-y}(MAPbBr_3)y(CsPbBr_3)_x$., turinti įvairios sudėties Cs monokristalus. Autoriai atrado, kad perovskito saulės elemento stabilumui įtakos turi Br ir Cs koncentracijos, todėl labai svarbu teisingai nustatyti šias vertes. Buvo nustatyta ideali formulė $(FAPbI_3)_{0.9}(MAPbBr_3)_{0.05}(CsPbBr_3)_{0.05}$, kuri pasižymėjo išskirtiniu stabilumu esant aplinkos sąlygoms, šviesai ir karščiui, ir ilgai krūvininkų gyvavimo trukmei – 16 μs. Dauguma perovskito sluoksnių, naudojamų didelio efektyvumo perovskito tandeminiuose saulės elementuose, yra sudaryti iš trijų katijonų perovskitų. Šios plėvelės pasižymi didesniu optiniu ir terminiu stabilumu, paprastai yra mažesnės ir neturi jokių adatinių skylučių. Albrecht ir kt. nustatė, kad perovskito tandeminių saulės elementų energijos konversijos efektyvumas yra 29,15 % [176]. Perovskito TSC atvirosios grandinės įtampa siekė 1,92 V dėl greito skylių ištraukimo ir skylių slopinančios nespindulinės rekombinacijos skyles išrenkančioje sąsajoje. Jie pasižymėjo puikiu stabilumu, išlaikant pradinį 95 % efektyvumą po 300 veikimo valandų be kapsulės. Be to, mūsų grupė nustatė, kad efektyvus saulės elementas buvo sukurtas sujungiant pusiau skaidrų perovskito viršutinį sluoksnį su apatiniu pramoniniu n tipo dvifaziu monokristaliniu

PERT Si. Toks elementas vadinamas trijų katijonų perovskito/Si tandeminiu saulės elementu. Galutinis dizainas nustatė naujas energijos konversijos efektyvumo gaires tarp keturių sluoksnių architektūrų, pasiekdamas 26,6 % efektyvumą. Apatinis Si elementas sudarė 7,2 % viso efektyvumo, o vien viršutinis elementas perovskitas sudarė 19,4 %.

KARŠTIEJI KRŪVININKAI PEROVSKITŲ SAULĖS ELEMENTUOSE

Perovskito saulės elementų kontekste karštieji krūvininkai yra svarbūs kaip fundamentalūs fizikiniai veiksniai, taip pat ir praktinėje prietaisų inžinerijoje: krūvininkai, turi didelę kinetinę energiją iškart po fotosužadinimo, todėl jie yra potencialių nuostolių šaltinis, bet taip pat leidžia įveikti įprastus efektyvumo apribojimus. Tradicinėse fotovoltinėse medžiagose, tokiose kaip Si, didelės energijos fotonai (kurių energija gerokai viršija draudžiamųjų energijų juostą) sukuria karštus elektronus ir skyles. Tačiau jie labai greitai (per mažesnius nei pikosekundžių laiko intervalus) praranda savo perteklinę energiją dėl krūvininkų ir fononų sąveikos, kol jų energija dar negali būti naudinga, todėl susidaro dideli terminiai nuostoliai, kurie tiesiogiai riboja konversijos efektyvumą pagal ShockleyQueisser (SQ) detaliosios pusiausvyros dėsnį. Perovskito medžiagose, priešingai, karštieji krūvininkai šąla labai lėtai (nuo dešimčių iki šimtų pikosekundžių) dėl daugelio efektų, įskaitant stiprią elektronų ir fononų sąveiką, didelės energijos poliaronų susidarymą, karštųjų fononų siaurą praėjimą ir santykinai minkštą gardelę, todėl po fotonų absorbcijos didelių energijų karšti krūvinikai perovskituose išlieka ilgiau nei daugumoje kitų puslaidininkių. Perovskito pagrindu sukurtoje tandeminėje saulės elementų architektūroje, kur yra bent du skirtingų draudžiamųjų energijos juostų absorberio sluoksniai, karštųjų krūvinikų valdymas yra dar svarbesnis: viršutinis sluoksnis, pagamintas iš plačios draudžiamosios juostos perovskito, sugeria didesnės energijos fotonus, todėl šiame sluoksnyje susidaro tam tikras karštųjų krūvinikų kiekis, o apatinis sluoksnis (kuris gali būti Si arba mažos draudžiamosios juostos perovskitas) sugeria tik mažesnės energijos fotonus, todėl sukuria mažą karštųjų krūvinikų kiekį. Įprastas dviejų sluoksnių perovskito TSC turės plačios draudžiamosios juostos (~1,7–1,8 eV) viršutinį subsluoksnį ir siauros draudžiamosios juostos (~1,1–1,3 eV perovskito arba ~1,12 eV Si) apatinį subsluoksnį. Šioje konfigūracijoje galima atlikti spektrinį skaidymą, kai didelės energijos fotonai sugeriami viršutiniame sluoksnyje, o praėję mažesnės energijos fotonai, sugeriami apatiniame sluoksnyje, taip konvertuojant kuo daugiau energijos ir sumažinant nuostolius dėl terminio energijos atidavimo.

Fotonų sugertis viršutiniuose perovskito tandeminių saulės elementų sluoksniuose yra iš esmės svarbus procesas, leidžiantis tokios architektūros saulės elementuose viršyti vienos sandūros efektyvumo ribas, atveriant kelią naujos kartos saulės energijos konversijos technologijoms. Įprastame perovskito tandeminiame elemente viršutiniam sluoksniui pagaminti naudojama plačios draudžiamosios juostos perovskitas. Fotonų absorbcija ir karštųjų krūvininkų elgesys perovskito TSC viršutiniuose elementuose yra raktas į anksčiau nepasiektą naujos kartos fotovoltinį našumą dėl nepaprastos perovskito medžiagų optinės kokybės ir neįprastos karštųjų krūvininkų fizikos derinio. Iš principo tandeminė geometrija gali būti naudojama spektrui padalinti taip, kad kiekvienas sluoksnis galėtų veikti netoli savo draudžiamosios juostos, sumažinant nuostolius dėl terminio atšalimo. Tačiau fotonai, kurių energija artima apatinio elemento draudžiamosios juostos pločiui, karštųjų krūvinikų nesukuria. Viršutinis perovskito sluoksnis veikia kaip spektrinis filtras apatiniam, kur fotonai su energija didesne už draudžiamosios energijos juostos plotį, yra sugeriami viršutiniame sluoksnyje, o mažesnios energijos fotonai gali praeiti pro viršutinį sluoksnį ir pasiekti apatinį. Šis filtravimas turi įtakos krūvininkų populiacijai apatiniame sluoksnyje tiek srauto, tiek energetiniu požiūriu. Esant visiškai absorbcijai arba nespindulinei rekombinacijai viršutiniame sluoksnyje, apatiniame sluoksnyje nėra galimybės sugeneruoti vadinamuosius karštus krūvininkus su pertekline energija.

MEDŽIAGOS IR METODAI

Atsižvelgiant tiek į naujų medžiagų, kurios gali būti naudojamos perovskito lustų gamyboje, kūrimą, tiek į pastaruoju metu pasiektą pažangą siekiant geriau suprasti perovskito prietaisų veikimo principus, pastebėtina, kad abu šie dalykai vyksta kartu. Tiek visa PSC architektūra, tiek naudojamų medžiagų pasirinkimas daro didelę įtaką pagaminto prietaiso elektrinėms ir optinėms savybėms. Taip pat galima optimizuoti perovskitų charakteristikas modifikuojant jų elementinę sudėtį. Kalbant apie optinę absorbciją, draudžiamąją juostą, stabilumą ir defektų leistiną nuokrypį, yra labai svarbus tikslus medžiagų pasirinkimas ir jų derinys. Pavyzdžiui, perovskitų terminis ir drėgmės stabilumas gali būti gerokai padidintas naudojant mišrius katijonus ir halogenidus. Tai taip pat leidžia tiksliai sureguliuoti draudžiamąją juostą, kad būtų maksimaliai sugerta saulės šviesa. Perovskito saulės elementuose naudojami penki pagrindiniai medžiagų tipai: metalinė kontaktinė medžiaga, šviesą sugerianti perovskito medžiaga, elektronų ir skylių pernašos sluoksniai ir skaidrus laidus oksidas sluoksnis.

Šios disertacijos rėmuose pasirinkome švino pagrindu sudarytas trijų katijonų perovskito kompozicijas. Kruopščiai suprojektuoti du pavyzdiniai trijų katijonų perovskito dariniai: $Cs_x(FA_{0.83}MA_{0.17})_{(1-x)}Pb(I_{0.83}Br_{0.17})_3$ ir Sn modifikuotas jo atitikmuo $Cs_x(FA_{0.83}MA_{0.17})_{(1-x)}Pb_{0.8}Sn_{0.2}(I_{0.83}Br_{0.17})_3$. Pirmasis Pb pagrindu sukurtas darinys $Cs_x(FA_{0.83}MA_{0.17})_{(1-x)}Pb(I_{0.83}Br_{0.17})_3$ buvo taktiškai pasirinktas, nes jis stabilesnis, optimizuotesnis jo fotovoltinis elgesys ir optimali krūvininkų judrumo bei rekombinacijos dinamikos pusiausvyra. Siekiant pagerinti fazinį stabilumą, į šią formulę įterpiami Cs^+ jonai, o tai padeda išvengti nepageidaujamų fazinių virsmų, kurie buvo paplitę grynai organiniuose perovskito analoguose, įskaitant gryną $FAPbI_3$ ir $MAPbI_3$. Pridėjus Cs^+ palengvėja problemos dėl jautrumo šilumai ir drėgmei sprendimas, todėl kristalizacija vyksta nuolat ir tolygiai, o grūdelių ribose smarkiai sumažėja defektų tankis. Pridėjus alavo į antrąjį darinį, $Cs_x(FA_{0.83}MA_{0.17})_{(1-x)}Pb_{0.8}Sn_{0.2}(I_{0.83}Br_{0.17})_3$ atsiranda dar daugiau naujų jo savybių. Dėl selektyvaus alavo įterpimo draudžiamoji juosta susiaurėja, ir šviesos absorpcijos kraštas slenka link ilgesniųjų bangų.

BANDINIŲ GAMYBA

Pirmajame etape ant išvalytų FTO substratų, naudojant purškiamąją pirolizę, buvo metodiškai nusodinamas vienodas, kompaktiškas TiO_2 sluoksnis. Viso proceso metu buvo palaikoma 450°C temperatūra. Šiame etape naudotas pirmtako tirpalas buvo sudarytas iš titano diizopropoksido bis(acetilacetonato) (Ti(acac)OiPr, „Merck-KGaA“, Vokietija), kuris buvo sumaišytas su bevandeniu etanoliu („Sigma-Aldrich“, Misūris, JAV) tiksliu tūrio santykiu 1:9. Po nusodinimo proceso substratai buvo atkaitinti 450°C temperatūroje tiksliai 15 minučių, siekiant pagerinti kristalinę kokybę ir pasiekti didžiausią įmanomą laidumą. Po to jie buvo kontroliuojamu greičiu atvėsinti iki kambario temperatūros, kad būtų išvengta bet kokių struktūrinių deformacijų ar defektų. Antrajame projektavimo proceso žingsnyje buvo gaminamas mezoporinio TiO_2 karkasas, kuris būtinas elektronų pernašai ir sluoksnių veikimui. Titano oksido nanodalelių, tolygiai disperguotų, kurių vidutinis skersmuo yra 30 nm, suspensija buvo praskiesta etanoliu santykiu 1:6, kurios tikslus tūris 180 µL automatine pipete buvo užlašinama ant kompaktiško TiO_2 sluoksnio.Tada buvo paleidžiama sukimosi programa: 4000 aps./min. greičiu 20 sekundžių su2000 aps./min/s pagreičiu. Siekiant suformuoti šio sluoksnio struktūrinį vientisumą, jį reikėjo atkaitinti 450°C temperatūroje 30 minučių. Ši procedūra sukūrė skaidrias poras, kurios yra labai svarbios vėlesnei perovskito infiltracijai. Pasibaigus atkaitinimo

procesui, bandiniai buvo greitai perkelti į azotu pripildytą spintą („M-Braun Inertgas-Systeme GmbH“, Garching prie Miuncheno, Vokietija). Šioje spintoje buvo sukurti griežtai kontroliuojamą drėgmės neturinčią aplinką. Trečiajame proceso etape pagrindinis perovskito sluoksnis buvo kruopščiai nusodintas iš šviežiai sukurtų pirmtakų tirpalų. Buvo naudojamos tokios molinės koncentracijos: 1,2 M švino jodidas (PbI_2; „Sigma-Aldrich“, Misūris, Jungtinės Amerikos Valstijos), 0,2 M metilamonio bromidas (MABr; „Greatcell Solar Italia“, Italija), 0,2 M švino bromidas ($PbBr_2$; „Sigma-Aldrich“, Misūris, Jungtinės Amerikos Valstijos) ir 1 M formamidinio jodidas (FAI; „Greatcell Solar Italia“, Italija). Reikėjo kruopščiai paruošti tirpiklių sistemą: bevandenis DMF ir dimetilsulfoksidas (DMSO, „Sigma-Aldrich“, Misūris, JAV) buvo sumaišyti tūrio santykiu 4:1. Norint tiksliai reguliuoti Cs koncentraciją ties 10 %, buvo pridėta Cs jodido (CsI, „Strem Chemicals Inc.“, Masačusetsas, Jungtinės Amerikos Valstijos). Cs pirmiausia buvo ištirpintas 1,5 M DMSO tirpale. Norint pagaminti plėveles, kurių sudėtis $Cs_x(FA_{0.83}MA_{0.17})_{(1-x)}Pb_{0.8}Sn_{0.2}(I_{0.83}Br_{0.17})_3$, į mišinį buvo įmaišyta PbI_2 ir SnI_2 tiksliu moliniu santykiu 4:1. Siekiant, kad būtų užtikrintas visiškas tirpimas ir vienalytiškumas, lygiai vieną valandą tirpalas buvo kruopščiai maišomas 60°C temperatūroje. Šiam pirmtako tirpalui padengti buvo naudojamas griežtas dviejų pakopų metodas. Pirmiausia tirpalas buvo sukamas 1000 aps./min. greičiu lygiai dešimt sekundžių. Iškart po to dar trisdešimt sekundžių buvo sukamas didesniu 6000 aps./min. greičiu. Per paskutines 10 sukimo sekundžių buvo apdorota antitirpikliu, sudarytu iš lygiai 150 µl chlorbenzeno („Sigma Aldrich“, Misūris, JAV). Šis apdorojimas buvo būtinas, kad būtų užtikrinta optimali perovskito kristalizacija. Po to, 60 minučių atkaitinus 100°C temperatūroje, buvo gautas kristalinis darinys. Ketvirtajame etape pagrindinis dėmesys buvo skiriamas HTL sukūrimui. Sunaudota lygiai 150 µl tirpalo, kurį sudarė 70 mM Spiro-OMeTAD chlorbenzene (CB), kurio koncentracija 85,78 mg/ml. Tirpalas buvo atsargiai įpilamas į Li-TFSI druską (520 mg/ml bevandeniame acetonitrilyje) ir 4-tret-butilpiridiną (TBP), kurie buvo atskirai įsigyti iš „Sigma Aldrich“, Misūris, Jungtinės Amerikos Valstijos, atitinkamai, ir sumaišyti 0,5 ir 3,3 moliniu santykiu. Sukimosi dengimo procesas buvo vykdomas 4000 aps./min. greičiu 25 sekundes, o spartus 2000 aps./min./s^{-2} pagreitis buvo palaikomas, siekiant galutinėje fazėje užtikrinti vienodą ir be defektų HTL. Aukso kontaktai buvo nusodinti naudojant terminį garinimą. Buvo kontroliuojamas jų storis – maždaug 70 nm. Šios svarbios operacijos, atliktos pažangios garinimo sistemos, žinomos kaip VAKSIS-PVD-Vapor-5S_Th („Vaksis Research and Development & Engineering“, Ankara,

Turkija), vakuuminėje kameroje, metu elektrodas buvo suprojektuotas taip, kad būtų kuo tvirtesnis, siekiant aukščiausio įmanomo įrenginio funkcionalumo lygio.

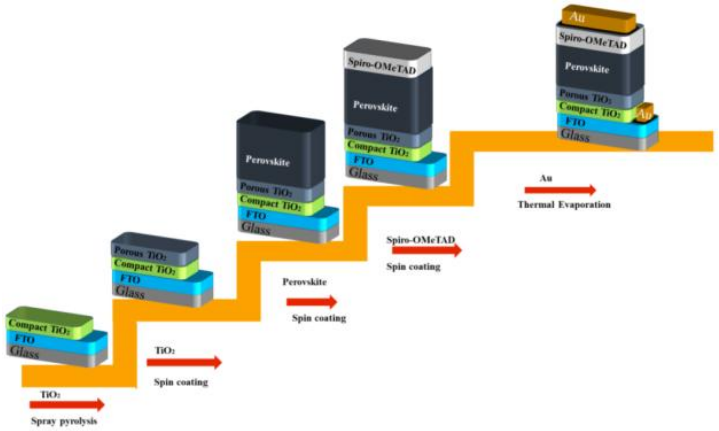

1 pav. Schema, palaipsniui iliustruojanti perovskito saulės elementų kūrimo procesą.

REZULTATAI IR DISKUSIJOS

Karštųjų krūvininkų vaidmuo formuojant fotoįtampą perovskito saulės elementuose

Išsamūs eksperimentiniai tyrimai buvo atlikti, siekiant sistemingai išanalizuoti dviejų tipų trijų katijonų perovskito plėvelių struktūrą, fotoluminescenciją ir optines savybes. Buvo tiriami $Cs_x(FA_{0.83}MA_{0.17})_{(1-x)}Pb(I_{0.83}Br_{0.17})_3$ perovskito sluoksniai, pagaminti švino pagrindu, ir sluoksniai $Cs_x(FA_{0.83}MA_{0.17})_{(1-x)}Pb_{0.8}Sn_{0.2}\,(I_{0.83}Br_{0.17})_3$ su švino ir alavo mišiniu.

2 paveiksle parodyti dviejų perovskito plėvelių skerspjūvio didelės skiriamosios gebos skenuojančio elektroninio mikroskopo (SEM) vaizdai: (a) įprasto švino pagrindo perovskito, $Cs_x(FA_{0.83}MA_{0.17})_{(1-x)}Pb(I_{0.83}Br_{0.17})_3$ ir (b) švino ir alavo mišinio perovskito, $Cs_x(FA_{0.83}MA_{0.17})_{(1-x)}Pb_{0.8}Sn_{0.2}(I_{0.83}Br_{0.17})_3$. Tokie skerspjūvio vaizdai leidžia vizualizuoti grūdelių struktūrą per visą perovskito sluoksnio storį, o tai yra labai svarbu siekiant optimizuoti optinę sugertį ir krūvio pernašos savybes, kai jis naudojamas kaip saulės elementas. Vaizduose tiksliai parodytas išmatuotas plėvelės storis. Tai rodo, kad Pb-Sn mišraus perovskito sluoksnis (2b pav.) yra daug storesnis, o paties perovskito sluoksnio storis yra apie 1 μm (987,7 nm), palyginti su vien švino pagrindu pagamintu perovskito sluoksniu (2a pav.),

kuris yra maždaug 800 nm (804,3 nm) storio. Šis Pb-Sn legiruotos plėvelės pastorėjimas gali būti siejamas su tuo, kad pakinta kristalizacijos ir plėvelės formavimosi proceso dinamika pridėjus alavo, kuris daro įtaką tirpalo klampumui ir keičia kristalizaciją bei kristalizacijos augimo greitį nusodinimo ir atkaitinimo metu. Nagrinėjant vidinę mikrostruktūrą, švino pagrindu pagamintoje perovskito plėvelėje (2a pav.) grūdeliai linkę daugiausia dėtis vertikaliai vienas ant kito. Ši vertikali grūdelių orientacija yra potencialiai naudinga krūvininkų pernašai per įrenginio storį, nes ji gali sukurti tiesioginius kelius, kuriais elektronai ir skylės gali būti pernešami iš fotoaktyvaus sluoksnio į atitinkamus krūvio pernašos sluoksnius. Taigi, grūdelių ribose yra sumažinta rekombinacijos tikimybė. Ir atvirkščiai, mišrioje Pb-Sn perovskito plėvelėje (2b pav.) grūdeliai yra daug didesni, o jų augime vyrauja šoninė arba horizontali orientacija.

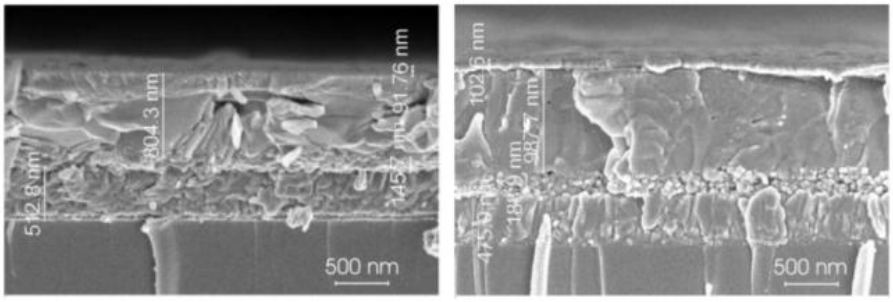

2 pav. Suformuotų perovskito plėvelių skerspjūvio SEM vaizdai: (a) Pb pagrindo perovskitas; (b) Pb-Sn pagrindo perovskitas.

3 paveiksle pateikti gryno švino pagrindo perovskito plėvelės (atvaizduotos žalia kreive) ir mišraus švino-alavo metalo (Pb-Sn) perovskito plėvelės (atvaizduotos mėlyna kreive) optinio pralaidumo spektrai. Įdomus spektrų bruožas yra tas, kad Pb-Sn pagrindo perovskito plėvelės atveju skiriasi raudonasis poslinkis. Sugerties kraštas, kur pralaidumas staigiai didėja, buvęs artimas nuliui išauga iki didesnių verčių, alavo turinčiame perovskite yra esant ilgesniam bangos ilgiui nei gryno švino turinčiame perovskite. Toks raudonasis poslinkis atitinka draudžiamosios energijos juostos susiaurėjimą, kuris yra tiesioginis dalinio švino pakeitimo alavu perovskito kristalinėje gardelėje rezultatas.

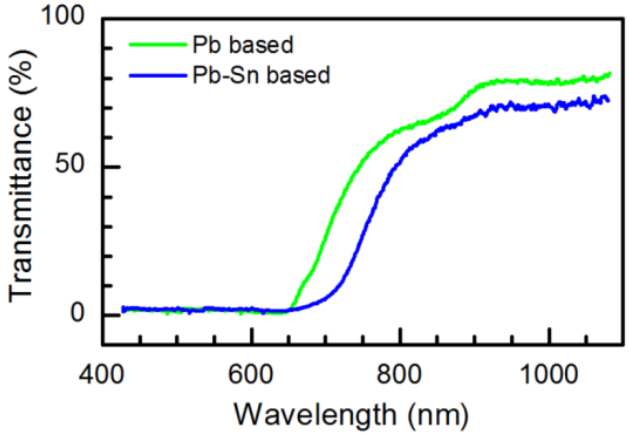

3 pav. Pb ir Pb-Sn pagrindu pagamintų perovskito plėvelių optinio pralaidumo spektrai.

4 pav. parodyta dviejų skirtingų absorbcinių sluoksnių pagrindu pagamintų saulės elementų fotoįtampos kinetika. Šie matavimai atlikti kruopščiai kontroliuojamomis eksperimentinėmis sąlygomis: prietaisai sužadinami impulsiniu lazeriu, kurio krintančios šviesos galios tankis yra 0,6 mW/cm^2 Pb pagrindu pagamintų PSC atveju, ir 0,8 mW/cm^2 – Pb-Sn pagrindu pagamintų PSC atveju.

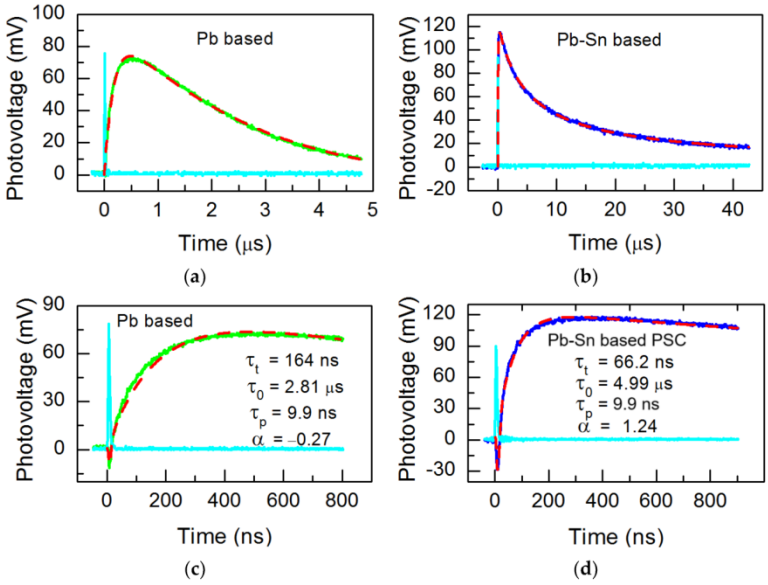

4 pav. Fotovoltinės įtampos priklausomybė nuo laiko, stebima perovskito saulės elementuose, pagamintuose Pb pagrindu (a, c) ir Pb-Sn pagrindu (b,

d). Sužadinimo lazerio galios tankis yra 0,6 mW/cm^2 Pb pagrindo PSC ir 0,8 mW/cm^2 Pb-Sn pagrindo PSC; lazerio impulsas pavaizduotas žydra spalva.

Šis fotoatsakas susidedantis iš priešingo poliariškumo dedamųjų yra svarbus veiksnys modeliuojant ir optimizuojant aukštos klasės fotovoltinius taikymus.

$$U = U_f + U_{ph} \qquad (1)$$

Po lazerio impulso, kuris 4 paveiksle visose srityse atvaizduotas žydros spalvos piku, seka pirmoji dedamoji, žymima raide U_f, kuri yra greitoji neigiamo poliariškumo fotoįtampos dedamoji. Ši dedamoji atsiranda dėl laisvųjų krūvininkų kaitinimo, kurį sukelia lazerio spinduliuotė. Antroji fotoįtampos dedamoji U_{ph}, yra lėtoji. Greitosios dedamosios U_f forma seka lazerio impulso formą ir galima aprašyti išraiška

$$U_f = K_f I_p \left(\frac{\tau}{\tau_p}\right)^4 \exp\left[-4\left(\frac{\tau}{\tau_p} - 1\right)\right] \qquad (2)$$

Čia I_p yra didžiausias lazerio intensyvumas, o τ_p yra lazerio impulso kilimo laikas. Koeficientas K_f nustatomas pagal eksperimente atliktus matavimo rezultatus. Antroji fotoįtampos dedamoji U_{ph} yra lėtoji dedamoji. Elektronų ir skylių porų susidarymas yra atsiradusios stebimos fotoįtampos priežastis. Jos formą galima išreikšti taip:

$$U_{ph} = U_o \left(\frac{e^{\frac{-t}{\tau_t}} - e^{\frac{-t}{\tau_{rec}}}}{\frac{1}{\tau_{rec}} - \frac{1}{\tau_t}}\right) \qquad (3)$$

Čia U_0 yra pradinė fotoįtampa. Tuo tarpu τ_t yra laiko konstanta, susijusi su elektronų pernaša perovskito sluoksnio viduje, τ_{rec} – krūvininkų rekombinacijos laikas.

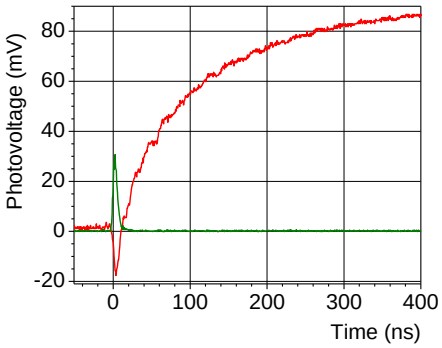

5 pav. Lazerio impulso (žalia spalva) ir fotoįtampos (raudona spalva) priklausomybė nuo laiko. Sužadinimo lazerio galios tankis yra 0,8 mW/cm^2.

Paveikus švino pagrindu pagamintus trijų katijonų perovskito saulės elementus lazerio impulsu (7 ns trukmė, 532 nm), jų fotoįtampos atsakas yra

pavaizduotas 5 pav. Norint ištirti, kaip karštųjų krūvininkų efektai gali pasireikšti kitų energetinių juostų dariniuose, nagrinėjame dvi absorberių sudėtis: grynus švino perovskitus $Cs_x(FA_{0.83}MA_{0.17})_{(1-x)}Pb(I_{0.83}\ Br_{0.17})_3$ ir švino alavo mišinio $Cs_x(FA_{0.83}MA_{0.17})_{(1-x)}Pb_{0.8}Sn_{0.2}(I_{0.83}\ Br_{0.17}\ )_3$ perovskito sluoksnius. Peroskito saulės elementų energijos konversijos efektyvumui didelę įtaką daro fotogeneruotų krūvininkų gyvavimo trukmė. Kuo ilgesnis šių krūvininkų gyvavimo laikas, tuo didesnė tikimybė, kad jie bus užfiksuoti elektroduose prieš sujungiant, taip sukuriant didesnę srovę ir efektyvumą. 6 paveiksle pateiktos geriausiai veikiančių PSC, pagamintų su ir be Sn įterpimo į perovskito absorberio sluoksnį, išmatuotos srovės ir įtampos charakteristikos.

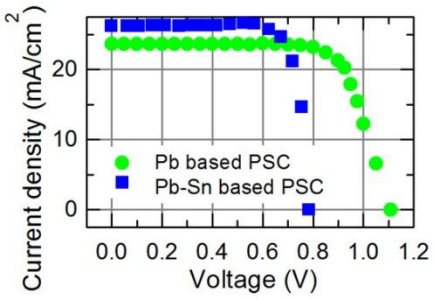

6 pav. Saulės elementų, pagamintų iš Pb ir Pb-Sn pagrindu išaugintų perovskito plėvelių, baltos šviesos apšvitos atsako priklausomybė nuo įtampos, esant 100 mW/cm^2.

Siekiant išsamiau palyginti perovskitų saulės elementų parametrus, 1 lentelėje pateiktos atitinkamos fotovoltinės charakteristikos elementų, pagamintų Pb ir Pb-Sn pagrindu: atviros grandinės įtampa V_{oc}, trumpo jungimo srovė J_{sc}, užpildos faktorius FF ir PCE.

1 lentelė. Perovskitų saulės elementų, pagamintų Pb ir Pb-Sn pagrindu parametrai: PCE, FF, V_{oc} ir J_{sc}.

Perovskite saulės elementas	V_{oc}, V	J_{sc}, mA·cm^{-2}	FF, %	PCE, %
Pb pagrindo	1,11	23,6	73	19,1
Pb-Sn pagrindo	0,785	26,2	70	14,4

Trijų katijonų perovskito/silicio tandeminis saulės elementas

Šiame darbe pateikiami išsamūs inovatyvaus keturių kontaktų tandeminio saulės elemento fotovoltinių charakteristikų tyrimo rezultatai. Tiriamasis įrenginys yra pagamintas iš trijų katijonų perovskito/silicio, kur ant viršutinio subelemento yra pusiau permatoma perovskito plėvelė, kurios sudėtis yra $Cs_x(FA_{0.83}MA_{0.17})_{(1-x)}Pb(I_{0.83}Br_{0.17})_3$. Būtent šis perovskito saulės elementas yra kruopščiai uždėtas ant pramoninės klasės n tipo monokristalinio dvifazio PERT silicio saulės elemento. Derinant optoelektronines charakteristikas trijų katijonų perovskito sluoksnio, kuris yra patobulintas tiek terminio, tiek fazinio stabilumo ir geresnio krūvininkų pernešimo srityse, su gerai žinomu PERT silicio saules elementų gautas efektyvus tandeminis saulės elementas. Tandeminio perovskito/silicio saulės elemento schema parodyta 7 paveiksle.

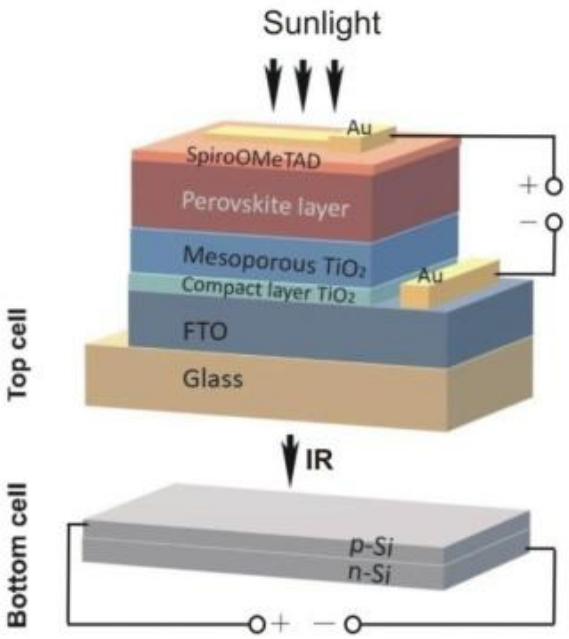

7 pav. Suprojektuotas trijų katijonų perovskito/silicio tandeminis saulės elementas. Apačioje esantis silicio elementas yra pilkos spalvos.

Šio sprendimo privalumas yra tas, kad perovskito sluoksnis yra pusiau skaidrus, ir šviesa gali prasiskverbti į apačioje esantį silicio elementą, būdama pakankamo intensyvumo, kad būtų kuo geriau išnaudotas visas saulės spektras; ši konstrukcija taip pat leidžia dviem subelementams veikti nepriklausomai keturių terminalų elemente, o ne pusės elemento poroje.

Taigi, dėl šios sinergetinės konstrukcijos tandeminio saulės elemento energijos konversijos efektyvumas yra geresnis – 26,6. Toks efektyvumas taip pat yra vienas didžiausių iki šiol užfiksuotų keturių terminalų perovskito/silicio tandeminių saulės elementų efektyvumo rodiklių, o tai rodo perovskito/silicio tandemų, kaip būsimos didelio efektyvumo fotovoltinės technologijos, gyvybingumą. Puikus veikimas rodo daug žadančias šio tipo tandeminio darinio perspektyvas saulės energijos konversijoje ir didėjančių atsinaujinančių energijos išteklių poreikių tenkinime. Gaminant perovskito/silicio tandeminį saulės elementą, naudojome komerciškai prieinamą apatinį subelementą – n tipo monokristalinį dvifazį PERT silicio saulės elementą („DS New Energy“, Kinija).

8a paveiksle pateikta ant mezoporinio TiO_2 sluoksnio užauginto trigubo katijono perovskito sluoksnio skenuojančio elektroninio mikroskopo (SEM) nuotrauka iš viršaus. Pastebėta, kad nedaugelio perovskito grūdelių šoniniai matmenys viršija 1000 nm, o tai rodo, kad plėvelės augimo proceso metu buvo sėkmingi grūdelių augimas ir koalescencija. Paviršiaus morfologija yra itin plokščia ir lygi, atitinkanti aukštos kokybės plėveles, apie kurias anksčiau buvo pranešta literatūroje. Šie lygūs paviršiai yra pranašesni krūvio laidumo atžvilgiu, taip pat sumažina krūvio rekombinacijos nuostolių tikimybę sąsajoje. 8b paveiksle matyti daugiau informacijos apie Perovskito sluoksnio struktūrą ir morfologiją: perovskito sluoksnio storis yra pastovus, maždaug (710±40) nm. Tai rodo nusodinimo, įvykusio proceso metu, tolygumą. Skerspjūvyje nustatyta, kad plėvelę sudaro perovskito grūdeliai, nors jie išdėstyti ne per visą sluoksnio storį. Jie yra išdėstyti stulpeliais arba klasteriais, taip sukurdami grūdelių ribas, kurios yra vertikalios visoje plėvelėje. Ši struktūrinė ypatybė gali būti esminė krūvininkų dinamikoje, nes vertikaliai orientuotų grūdelių ribų egzistavimas gali skatinti arba trukdyti krūvininkų judėjimui dėl kristalografinės orientacijos arba dėl defektų. Apatiniai sluoksniai yra gerai apibūdinti, nes galima stebėti mezoporinį TiO_2 (mezo-TiO_2) karkasą, kompaktišką TiO_2 (c-TiO_2) blokuojantį sluoksnį ir FTO substratą, kuris yra laidus stiklas. Apskritai, SEM analizė įrodė, kad atliekant šį tyrimą pagamintos trigubų katijonų perovskito plėvelės gali turėti reikiamas struktūrines ypatybes, įskaitant stambius grūdelių dydžius, lygius paviršius ir tinkamas sluoksnių ribas. Išvardintos savybės turėtų atlikti teigiamą vaidmenį tandeminių saulės elementų fotovoltiniame veikime.

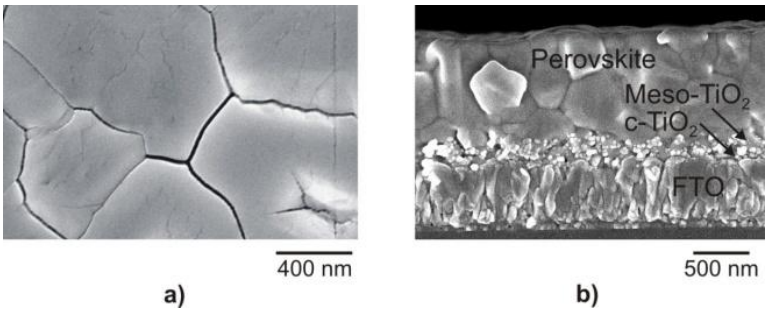

8 pav. Ant mezoporinio titano dioksido susidariusio perovskito sluoksnio paviršiaus skenuojančio elektroninio mikroskopo vaizdas (a) ir skerspjūvio SEM vaizdas (b).

9 paveiksle parodytos išmatuotos pagaminto trijų katijonų perovskito/silicio tandeminio saulės elemento voltamperinės charakteristikos, pažymėtos raudonais taškais. Šis perovskito saulės elementas turi didelę trumpo jungimo srovę, kurį yra gana tvirtas geros perovskito sluoksnio optoelektroninės kokybės ir efektyvaus fotonų sugerties pajėgumo įrodymas. Didelė trumpo jungimo srovė rodo, kad krūvininkų generavimas ir surinkimas yra efektyvus, nes jis yra optimizuotas perovskito plėvelės struktūros ir defektų koncentracijos atžvilgiu.

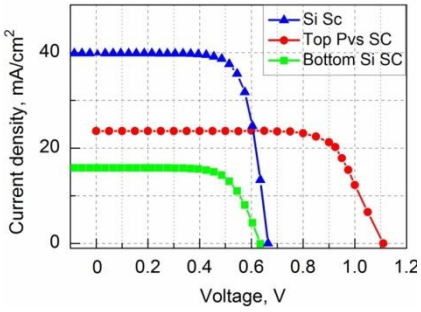

9 pav. Trijų katijonų perovskito/silicio tandeminio saulės elemento (raudoni taškai) ir silicio saulės elemento (mėlyni taškai) srovės tankio priklausomybės nuo įtampos, žali taškai –apatinio Si elemento VACh, esant 100 mW/cm^2 šviesos intensyvumui

2 lentelėje pateikti svarbiausi trijų katijonų perovskito saulės elemento fotovoltiniai parametrai: tai V_{oc}, J_{sc}, FF ir PCE. Tokie rodikliai yra būtini norint įvertinti įrenginio veikimą ir palyginti jį su kitomis fotovoltinėmis technologijomis.

2 lentelė. Perovskito saulės elemento, atskiro silicio saulės elemento ir silicio saulės elemento kaip apatinio elemento tandeminiame elemente fotovoltiniai parametrai.

Saulės elementas	V_{oc}, V	J_{sc}, mA·cm^{-2}	FF, %	PCE, %
Viršutinis perovskito SC	1,11	23,6	74	19,4
Atskiriantis Si SC	0,67	40,0	72	19,3
Apatinis Si SC	0,64	15,8	71	7,2

IŠVADOS

• Apšvietus trumpu lazerio impulsu vienos sandūros perovskito saulės elementą fotoįtampos atsakas pasižymi dviem priešingai poliarizuotomis dedamosiomis: greita neigiama dalimi, kurią sukelia karštieji krūvininkai dėl krūvininkų kaitinimo šviesa, ir lėtesne teigiama dalimi, kurią sukelia tradicinė elektronų ir skylių porų generacija. Toks dviejų dedamųjų elgesys rodo, kad karštieji krūvininkai neigiamai veikia fotoįtampą, todėl sumažėja bendras vienos sandūros perovskito saulės elementų energijos konversijos efektyvumas.

• Plačiajuosčių perovskito elementų išdėstymas ant siaurajuosčių elementų (pvz., silicio): didelės energijos fotonus sugeria viršutinis elementas, o praleistus mažos energijos fotonus sugeria apatinis elementas. Toks išdėstymas sumažina šiluminės energijos nuostolius ir pagerina saulės spektro panaudojimą, todėl padidėja bendras efektyvumas. Siekiant pagerinti perovskito saulės elementų įtampos ir srovės reikšmes reikia pailginti krūvininkų gyvavimo trukmę ir sumažinti rekombinacijos nuostolius mažinant defektų tankį.

• Potenciniai barjerai, esantys krūvio pernašos sluoksniuose dėl energijų juostos lenkimo prisideda prie karštųjų krūvininkų termoelektrovaros atsiradimo, o tai kenkia įrenginio efektyvumui. Šių galimų barjerų pašalinimas arba susilpninimas, sumažina karštųjų krūvininkų termoelektrovarą ir taip pagerina peroskitų saulės elementų energijos konversios efektyvumą.

•Į perovskito plėveles pridėjus alavo, susiaurėja draudžiamųjų energijų juosta. Tai prisideda prie nespinduliuojančių defektų susidarymo, kurie padidina rekombinacijos greitį paviršiuje ir labai sutrumpina fotoliuminescencijos gesimo trukmę. Tokios struktūrinės modifikacijos pablogina perovskito saulės elementų fotoelektrines savybes ir sumažina jų bendrą energijos konversijos efektyvumą, palyginti su jų analogais, pagamintais iš gryno švino pagrindu sukurtų perovskitų.

• Eksperimentinių rezultatų analizė jau parodė, kad naudojant perovskito/silicio tandeminius saulės elementus galima pasiekti reikšmingų energijos konversijos efektyvumo pokyčių, viršijančių vienos sandūros elementų ribas. Keturių terminalų tandeminės saulės elementų architektūros, sudarytos iš apatinio silicio elemento ir spektriniu požiūriu pusiau skaidraus trijų katijonų perovskito viršutinio elemento, bendras efektyvumas buvo 26,6 % (19,4 % pusiau skaidraus perovskito viršutinio elemento ir 7,2 % apatinio silicio elemento PCE), kuris viršijo atskirų perovskito ir silicio elementų efektyvumą. Tai rodo daugiasandūrinių saulės elementų efektyvumą ir svarbą siekiant įveikti tiek karštųjų krūvininkų efektų, tiek ir terminės energijos atidavimo sukeltus trūkumus.

PADĖKA

Norėčiau nuoširdžiai padėkoti savo vadovui prof. dr. Steponui Ašmontui, kurio besąlygiška parama, išsamūs patarimai ir griežtumas mokslo klausimais lėmė šio darbo suformulavimą visais jo aspektais. Jo aistra perovskitinių saulės elementų tyrimams paskatino mane peržengti per save ir leistis į kitą mokslo dimensiją. Laikas, praleistas su juo, buvo didžiulė garbė ir didžiausia privilegija, jam vadovaujant padėjusi man tobulėti.

Norėčiau padėkoti Valstybiniam fizinių ir technologijos mokslų centrui (FTMC), suteikusiam galimybę, išteklius ir paramą, kas leido man atlikti šį tyrimą. Čia buvo man palanki bendradarbiavimo atmosfera. Išskirtinė infrastruktūra ir mąstyti skatinanti akademinė bendruomenė, kurią teikia centras, suvaidino lemiamą vaidmenį praturtinant mano studijas.

Taip pat norėčiau padėkoti savo bendradarbiams dr. Aurimui Čerškui, dr. Jonui Gradauskui, dr. Astai Grigucevičienei, dr. Andžejui Lučunui, dr.Algirdui Sužiedėliui ir dr. Edmundui Širmuliui, kurie yra mano draugai, atvirai aptarė kai kuriuos klausimus ir praktiškai padėjo man laboratorijoje. Taip pat norėčiau pareikšti ypatingą padėką dr. Oleksandrui Masalskiui ir Ihoriui Žarčenkai, kurie lydėjo mane šioje kelionėje pastaruosius ketverius metus ir padėjo man ištverti net sudėtingiausias situacijas, pasitelkiant jų nuolatinę paramą ir draugystę.

Norėčiau padėkoti savo magistro studijų vadovui, prof. dr. Duan Yu, kuris supažindino mane su nuostabiu perovskitų pasauliu ir suteikė man galimybę ištirti jų galimybes savo tyrimų laboratorijoje. Šis darbas paremtas jo padrąsinimu ankstesniame darbo periode.

Galiausiai, esu dėkingas už viską savo tėvams, kurie suteikė emocinį šio sumanymo pagrindą; tylų ir tvirtą tikėjimą manimi, kuriems nesąmoningai, bet neatšaukiamai esu dėkingas. Ir savo žmonai, kuri savo beribe kantrybe, supratimu ir meile paskatino mane parašyti šį darbą, be kurios šis darbas nebūtų buvęs įmanomas.

REFERENCES

1. Owusu, P. A.; Asumadu-Sarkodie, S., A review of renewable energy sources, sustainability issues and climate change mitigation. *Cogent Engineering* **2016,** 3, (1), 1167990.
2. Katz, E. A., Perovskite: name puzzle and German-Russian odyssey of discovery. *Helvetica Chimica Acta* **2020,** 103, (6), e2000061.
3. Kojima, A.; Teshima, K.; Shirai, Y.; Miyasaka, T., Organometal halide perovskites as visible-light sensitizers for photovoltaic cells. *Journal of the american chemical society* **2009,** 131, (17), 6050-6051.
4. Li, H.; Shen, N.; Chen, S.; Guo, F.; Xu, B., Recent progress on synthesis, intrinsic properties and optoelectronic applications of perovskite single crystals. *Advanced Functional Materials* **2023,** 33, (24), 2214339.
5. Ašmontas, S.; Mujahid, M., Recent progress in perovskite tandem solar cells. *Nanomaterials* **2023,** 13, (12), 1886.
6. Chu, Q.-Q.; Sun, Z.; Hah, J.; Moon, K.-s.; Cheng, B.; Wang, D.; Xiao, P.; Zhou, Y.; Petrozza, A.; Yang, G.-J.; Wang, H.; Wong, C.-P., Progress, challenges, and further trends of all perovskites tandem solar cells: A comprehensive review. *Materials Today* **2023,** 67, 399-423.
7. Burschka, J.; Pellet, N.; Moon, S.-J.; Humphry-Baker, R.; Gao, P.; Nazeeruddin, M. K.; Grätzel, M., Sequential deposition as a route to high-performance perovskite-sensitized solar cells. *Nature* **2013,** 499, (7458), 316-319.
8. Saliba, M.; Matsui, T.; Seo, J.-Y.; Domanski, K.; Correa-Baena, J.-P.; Nazeeruddin, M. K.; Zakeeruddin, S. M.; Tress, W.; Abate, A.; Hagfeldt, A., Cesium-containing triple cation perovskite solar cells: improved stability, reproducibility and high efficiency. *Energy & environmental science* **2016,** 9, (6), 1989-1997.
9. Jaiswal, K. K.; Chowdhury, C. R.; Yadav, D.; Verma, R.; Dutta, S.; Jaiswal, K. S.; Karuppasamy, K. S. K., Renewable and sustainable clean energy development and impact on social, economic, and environmental health. *Energy nexus* **2022,** 7, 100118.
10. Abbasi, T.; Abbasi, S., Is the use of renewable energy sources an answer to the problems of global warming and pollution? *Critical Reviews in Environmental Science and Technology* **2012,** 42, (2), 99-154.
11. Rahman, M. M.; Alam, K.; Velayutham, E., Reduction of CO2 emissions: The role of renewable energy, technological innovation and export quality. *Energy Reports* **2022,** 8, 2793-2805.
12. Abas, N.; Kalair, A.; Khan, N., Review of fossil fuels and future energy technologies. *Futures* **2015,** 69, 31-49.

13. Suman, S., Hybrid nuclear-renewable energy systems: A review. *Journal of Cleaner Production* **2018,** 181, 166-177.
14. Panwar, N. L.; Kaushik, S. C.; Kothari, S., Role of renewable energy sources in environmental protection: A review. *Renewable and sustainable energy reviews* **2011,** 15, (3), 1513-1524.
15. Agrawal, S.; Soni, R., Renewable energy: Sources, importance and prospects for sustainable future. *Energy: Crises, Challenges and Solutions* **2021**, 131-150.
16. Demirbas, A., Global renewable energy projections. *Energy Sources, Part B* **2009,** 4, (2), 212-224.
17. Bulavko, G., Organic photovoltaics: A journey through time, advancements, and future opportunities. *History of science and technology* **2024,** 14, (1), 10-32.
18. Clegg, B., *Light Years: The Extraordinary Story of Mankind's Fascination with Light*. Icon Books Ltd: 2015.
19. Singh, V., Albert Einstein: His Miracle Year (1905). *Theoretical Physics* 5, 6.
20. Schrödinger, E., *Collected papers on wave mechanics*. American Mathematical Soc.: 2003; Vol. 302.
21. Wilson, A. H., The theory of electronic semi-conductors.-ii. *Proceedings of the Royal Society of London. Series A, Containing Papers of a Mathematical and Physical Character* **1931,** 134, (823), 277-287.
22. Tsakalakos, L., Introduction to photovoltaic physics, applications, and technologies. In *Nanotechnology for photovoltaics*, CRC Press: 2010; pp 19-66.
23. Bouroushian, M.; Bouroushian, M., Electrochemical Processes and Technology. *Electrochemistry of Metal Chalcogenides* **2010**, 309-349.
24. Fritts, C. E., On a new form of selenium cell, and some electrical discoveries made by its use. *American Journal of Science* **1883,** 3, (156), 465-472.
25. Wuebbles, D. J.; Jain, A. K., Concerns about climate change and the role of fossil fuel use. *Fuel processing technology* **2001,** 71, (1-3), 99-119.
26. Kumler, A.; Kravitz, B.; Draxl, C.; Vimmerstedt, L.; Benton, B.; Lundquist, J. K.; Martin, M.; Buck, H. J.; Wang, H.; Lennard, C., Potential effects of climate change and solar radiation modification on renewable energy resources. *Renewable and Sustainable Energy Reviews* **2025,** 207, 114934.
27. Faisal, S. S.; Hashim, E. T., An Approach to Solar Photovoltaic Systems Simulation Utilizing Builder Block: A Case Study of A 100 MW System. *Journal of Engineering* **2025,** 31, (1), 98-119.

28. Peráček, T.; Kaššaj, M., Legal Easements as Enablers of Sustainable Land Use and Infrastructure Development in Smart Cities. *Land* **2025,** 14, (4), 681.
29. Scully, M. O.; Sargent, M., The concept of the photon. *Physics Today* **1972,** 25, (3), 38-47.
30. Karzazi, Y.; Arbouch, I., Inorganic photovoltaic cells: Operating principles, technologies and efficiencies-Review. *Journal of Materials and environmental science* **2014,** 5, (5), 1505-2525.
31. El-Afifi, M. I., Solar Energy: Our Future for Sustainable Energy. *Nile Journal of Communication and Computer Science* **2024,** 7, (1), 67-83.
32. Olomiyesan, B.; Oyedum, O. D.; Ugwuoke, P.; Ezenwora, J. A.; Ibrahim, A., Solar energy for power generation: a review of solar radiation measurement processes and global solar radiation modelling techniques. **2015**.
33. Dragoni, M., Energy Flows at Earth's Surface. *The Physics Teacher* **2024,** 62, (9), 754-757.
34. Barbaro, S.; Coppolino, S.; Leone, C.; Sinagra, E., An atmospheric model for computing direct and diffuse solar radiation. *Solar Energy* **1979,** 22, (3), 225-228.
35. Green, M. A.; Bremner, S. P., Energy conversion approaches and materials for high-efficiency photovoltaics. *Nature materials* **2017,** 16, (1), 23-34.
36. Kangsabanik, J.; Svendsen, M. K.; Taghizadeh, A.; Crovetto, A.; Thygesen, K. S., Indirect band gap semiconductors for thin-film photovoltaics: high-throughput calculation of phonon-assisted absorption. *Journal of the American Chemical Society* **2022,** 144, (43), 19872-19883.
37. Bayod-Rújula, A. A., Solar photovoltaics (PV). In *Solar hydrogen production*, Elsevier: 2019; pp 237-295.
38. Wolf, M., The present state-of-the-art of photovoltaic solar energy conversion. *Solar Energy* **1961,** 5, (3), 83-94.
39. Sclar, N., Extrinsic silicon detectors for 3–5 and 8–14 μm. *Infrared Physics* **1976,** 16, (4), 435-448.
40. Haas, R.; Duic, N.; Auer, H.; Ajanovic, A.; Ramsebner, J.; Knapek, J.; Zwickl-Bernhard, S., The photovoltaic revolution is on: How it will change the electricity system in a lasting way. *Energy* **2023,** 265, 126351.
41. Saravanan, S.; Teja, T. K.; Dubey, R.; Kalainathan, S., Design and analysis of GaAs thin film solar cell using an efficient light trapping bottom structure. *Materials Today: Proceedings* **2016,** 3, (6), 2463-2467.
42. Dzimano, G. J. Modeling of photovoltaic systems. The Ohio State University, 2008.

43. Hamaguchi, C.; Hamaguchi, C., *Basic semiconductor physics*. Springer: 2010; Vol. 9.
44. Raval, N.; Gupta, A. K., Historic Developments, Current Technologies and Potential of Nanotechnology to Develop Next Generation Solar Cells with Improved Efficiency. *International Journal of Renewable Energy Development* **2015,** 4, (2).
45. Chapin, D. M.; Fuller, C. S.; Pearson, G. L., A new silicon p-n junction photocell for converting solar radiation into electrical power. *Journal of applied physics* **1954,** 25, (5), 676.
46. Bube, R. H., *Photovoltaic materials*. World Scientific: 1998; Vol. 1.
47. Geisz, J. F.; France, R. M.; Schulte, K. L.; Steiner, M. A.; Norman, A. G.; Guthrey, H. L.; Young, M. R.; Song, T.; Moriarty, T., Six-junction III–V solar cells with 47.1% conversion efficiency under 143 Suns concentration. *Nature energy* **2020,** 5, (4), 326-335.
48. Chopra, K.; Paulson, P.; Dutta, V., Thin-film solar cells: an overview. *Progress in Photovoltaics: Research and applications* **2004,** 12, (2-3), 69-92.
49. Pastuszak, J.; Węgierek, P., Photovoltaic Cell Generations and Current Research Directions for Their Development. *Materials* **2022,** 15, (16), 5542.
50. Sampaio, P. G. V.; González, M. O. A., Photovoltaic solar energy: Conceptual framework. *Renewable and Sustainable Energy Reviews* **2017,** 74, 590-601.
51. Green, M. A.; Hishikawa, Y.; Warta, W.; Dunlop, E. D.; Levi, D. H.; Hohl-Ebinger, J.; Ho-Baillie, A. W. H., Solar cell efficiency tables (version 50). *Progress in Photovoltaics: Research and Applications* **2017,** 25, (7), 668-676.
52. C. B, I.; Marques Lameirinhas, R. A.; N. Torres, J. P.; Fernandes, C. A. F., Comparative study of the copper indium gallium selenide (CIGS) solar cell with other solar technologies. *Sustainable Energy & Fuels* **2021,** 5, (8), 2273-2283.
53. Green, M. A., Crystalline and thin-film silicon solar cells: state of the art and future potential. *Solar Energy* **2003,** 74, (3), 181-192.
54. Kessler, F.; Rudmann, D., Technological aspects of flexible CIGS solar cells and modules. *Solar Energy* **2004,** 77, (6), 685-695.
55. Zhong, M.; Yang, D.; Zhang, J.; Shi, J.; Wang, X.; Li, C., Improving the performance of CdS/P3HT hybrid inverted solar cells by interfacial modification. *Solar Energy Materials and Solar Cells* **2012,** 96, 160-165.
56. Dunlap-Shohl, W. A.; Zhou, Y.; Padture, N. P.; Mitzi, D. B., Synthetic approaches for halide perovskite thin films. *Chemical reviews* **2018,** 119, (5), 3193-3295.
57. Mulligan, J. F., Heinrich Hertz and the development of physics. *Physics Today* **1989,** 42, (3), 50-57.

58. Smith, G. E., JJ Thomson and the Electron, 1897–1899. *Histories of the electron. The birth of microphysics* **2001**, 21-76.
59. Gingras, Y., The creative power of formal analogies in physics: The case of Albert Einstein. *Science & Education* **2015,** 24, (5), 529-541.
60. Ward, P. L., On the Planck-Einstein Relation. In 2020.
61. Asif, M. H.; Zhongfu, T.; Ahmad, B.; Irfan, M.; Razzaq, A.; Ameer, W., Influencing factors of consumers' buying intention of solar energy: a structural equation modeling approach. *Environmental Science and Pollution Research* **2023,** 30, (11), 30017-30032.
62. Marcelino, R. B.; Amorim, C. C., Towards visible-light photocatalysis for environmental applications: band-gap engineering versus photons absorption—a review. *Environmental Science and Pollution Research* **2019,** 26, 4155-4170.
63. Peymanfar, R.; Yektaei, M.; Javanshir, S.; Selseleh-Zakerin, E., Regulating the energy band-gap, UV–Vis light absorption, electrical conductivity, microwave absorption, and electromagnetic shielding effectiveness by modulating doping agent. *Polymer* **2020,** 209, 122981.
64. Daxini, R.; Wu, Y., Review of methods to account for the solar spectral influence on photovoltaic device performance. *Energy* **2024,** 286, 129461.
65. Riverola, A.; Vossier, A.; Chemisana, D., Fundamentals of solar cells. In *Nanomaterials for Solar Cell Applications*, Elsevier: 2019; pp 3-33.
66. Tamulaitis, G.; Juška, G., Energiją taupančios puslaidininkinės technologijos. *Vilnius: Progretus* **2008**, 116-121.
67. Rida, K.; Al-Waeli, A.; Al-Asadi, K., The impact of air mass on photovoltaic panel performance. *Eng. Sci. Rep* **2016,** 1, (1), 1-9.
68. Shnishil, A. H.; Chid, S. S.; Yaseen, M. J.; Alwana, T. J., Influence of air mass on the performance of many types of PV modulus in Baghdad. *Energy Procedia* **2011,** 6, 153-159.
69. Passow, K.; Lee, M. In *Effect of spectral shift on solar PV performance*, 2016 IEEE Conference on Technologies for Sustainability (SusTech), 2016; IEEE: 2016; pp 246-250.
70. Xue, Y.; Igari, S., Reference solar spectra and their generation models. *Journal of Science and Technology in Lighting* **2023,** 46, 6-18.
71. website http://hyperphysics.phy-astr.gsu.edu/hbase/Solids/band.html#c5. http://hyperphysics.phy-astr.gsu.edu/hbase/Solids/band.html#c5
72. Ngwashi, D. K.; Tsafack, P., Enhancement of Ready-Made Silicon Photo-voltaic Panels' Field Performance-a Review. *American Journal of Electrical Power and Energy Systems* **2023,** 12, (4), 59-67.

73. Bondoc, C. C. E. Feasibility and Environmental Life Cycle Assessment of Mono-Crystalline Silicon (Mono-Si) Solar Photovoltaic Panels with Recycled Vs. Non-Recycled Materials. Villanova University, 2023.
74. Limmanee, A.; Sitthiphol, N.; Jaroensathainchok, S.; Pluemkamon, R.; Kotesopa, S.; Udomdachanut, N.; Hongsingthong, A., A survey of decommissioned photovoltaic modules from solar power plants in Thailand: Performance and second life opportunities. *IEEJ Transactions on Electrical and Electronic Engineering* **2023,** 18, (12), 1967-1972.
75. Smith, A. R.; Ghamari, M.; Velusamy, S.; Sundaram, S., Thin-Film Technologies for Sustainable Building-Integrated Photovoltaics. *Energies* **2024,** 17, (24), 6363.
76. Messenger, R. A., *Photovoltaic systems engineering*. CRC press: 2018.
77. Baiju, A.; Yarema, M., Status and challenges of multi-junction solar cell technology. *Frontiers in Energy Research* **2022,** 10, 971918.
78. Hoppe, H.; Sariciftci, N. S., Organic solar cells: An overview. *Journal of materials research* **2004,** 19, (7), 1924-1945.
79. Akkerman, Q. A.; Rainò, G.; Kovalenko, M. V.; Manna, L., Genesis, challenges and opportunities for colloidal lead halide perovskite nanocrystals. *Nature materials* **2018,** 17, (5), 394-405.
80. Mitchell, R. H.; Welch, M. D.; Chakhmouradian, A. R., Nomenclature of the perovskite supergroup: A hierarchical system of classification based on crystal structure and composition. *Mineralogical Magazine* **2017,** 81, (3), 411-461.
81. Peña, M. A.; Fierro, J., Chemical structures and performance of perovskite oxides. *Chemical reviews* **2001,** 101, (7), 1981-2018.
82. Era, M.; Morimoto, S.; Tsutsui, T.; Saito, S., Organic-inorganic heterostructure electroluminescent device using a layered perovskite semiconductor (C6H5C2H4NH3) 2PbI4. *Applied physics letters* **1994,** 65, (6), 676-678.
83. Wells, H. L., Über die cäsium-und kalium-bleihalogenide. *Zeitschrift für anorganische Chemie* **1893,** 3, (1), 195-210.
84. Kagan, C. R.; Mitzi, D. B.; Dimitrakopoulos, C. D., Organic-inorganic hybrid materials as semiconducting channels in thin-film field-effect transistors. *Science* **1999,** 286, (5441), 945-947.
85. Kojima, A.; Teshima, K.; Miyasaka, T.; Shirai, Y. In *Novel photoelectrochemical cell with mesoscopic electrodes sensitized by lead-halide compounds (2)*, ECS Meeting Abstracts, 2006; IOP Publishing: 2006; p 397.
86. Im, J.-H.; Lee, C.-R.; Lee, J.-W.; Park, S.-W.; Park, N.-G., 6.5% efficient perovskite quantum-dot-sensitized solar cell. *Nanoscale* **2011,** 3, (10), 4088-4093.

87. Kim, H.-S.; Lee, C.-R.; Im, J.-H.; Lee, K.-B.; Moehl, T.; Marchioro, A.; Moon, S.-J.; Humphry-Baker, R.; Yum, J.-H.; Moser, J. E., Lead iodide perovskite sensitized all-solid-state submicron thin film mesoscopic solar cell with efficiency exceeding 9%. *Scientific reports* **2012,** 2, (1), 591.
88. Ponseca Jr, C. S.; Savenije, T. J.; Abdellah, M.; Zheng, K.; Yartsev, A.; Pascher, T. r.; Harlang, T.; Chabera, P.; Pullerits, T.; Stepanov, A., Organometal halide perovskite solar cell materials rationalized: ultrafast charge generation, high and microsecond-long balanced mobilities, and slow recombination. *Journal of the American Chemical Society* **2014,** 136, (14), 5189-5192.
89. Yin, W.-J.; Shi, T.; Yan, Y., Unusual defect physics in CH3NH3PbI3 perovskite solar cell absorber. *Applied physics letters* **2014,** 104, (6).
90. Stranks, S. D.; Eperon, G. E.; Grancini, G.; Menelaou, C.; Alcocer, M. J.; Leijtens, T.; Herz, L. M.; Petrozza, A.; Snaith, H. J., Electron-hole diffusion lengths exceeding 1 micrometer in an organometal trihalide perovskite absorber. *Science* **2013,** 342, (6156), 341-344.
91. Muljarov, E. A.; Tikhodeev, S.; Gippius, N.; Ishihara, T., Excitons in self-organized semiconductor/insulator superlattices: PbI-based perovskite compounds. *Physical Review B* **1995,** 51, (20), 14370.
92. Ogomi, Y.; Morita, A.; Tsukamoto, S.; Saitho, T.; Fujikawa, N.; Shen, Q.; Toyoda, T.; Yoshino, K.; Pandey, S. S.; Ma, T., CH3NH3Sn x Pb (1–x) I3 Perovskite solar cells covering up to 1060 nm. *The journal of physical chemistry letters* **2014,** 5, (6), 1004-1011.
93. Stranks, S. D.; Snaith, H. J., Metal-halide perovskites for photovoltaic and light-emitting devices. *Nature nanotechnology* **2015,** 10, (5), 391-402.
94. Dong, Q.; Fang, Y.; Shao, Y.; Mulligan, P.; Qiu, J.; Cao, L.; Huang, J., Electron-hole diffusion lengths> 175 μm in solution-grown CH3NH3PbI3 single crystals. *Science* **2015,** 347, (6225), 967-970.
95. Giorgi, G.; Fujisawa, J.-I.; Segawa, H.; Yamashita, K., Small photocarrier effective masses featuring ambipolar transport in methylammonium lead iodide perovskite: a density functional analysis. *The journal of physical chemistry letters* **2013,** 4, (24), 4213-4216.
96. Grätzel, M., The light and shade of perovskite solar cells. *Nature materials* **2014,** 13, (9), 838-842.
97. Yin, W.-J.; Yang, J.-H.; Kang, J.; Yan, Y.; Wei, S.-H., Halide perovskite materials for solar cells: a theoretical review. *Journal of Materials Chemistry A* **2015,** 3, (17), 8926-8942.
98. Schmidt-Mende, L.; Dyakonov, V.; Olthof, S.; Ünlü, F.; Lê, K. M. T.; Mathur, S.; Karabanov, A. D.; Lupascu, D. C.; Herz, L. M.; Hinderhofer, A.; Schreiber, F.; Chernikov, A.; Egger, D. A.;

Shargaieva, O.; Cocchi, C.; Unger, E.; Saliba, M.; Byranvand, M. M.; Kroll, M.; Nehm, F.; Leo, K.; Redinger, A.; Höcker, J.; Kirchartz, T.; Warby, J.; Gutierrez-Partida, E.; Neher, D.; Stolterfoht, M.; Würfel, U.; Unmüssig, M.; Herterich, J.; Baretzky, C.; Mohanraj, J.; Thelakkat, M.; Maheu, C.; Jaegermann, W.; Mayer, T.; Rieger, J.; Fauster, T.; Niesner, D.; Yang, F.; Albrecht, S.; Riedl, T.; Fakharuddin, A.; Vasilopoulou, M.; Vaynzof, Y.; Moia, D.; Maier, J.; Franckevičius, M.; Gulbinas, V.; Kerner, R. A.; Zhao, L.; Rand, B. P.; Glück, N.; Bein, T.; Matteocci, F.; Castriotta, L. A.; Di Carlo, A.; Scheffler, M.; Draxl, C., Roadmap on organic–inorganic hybrid perovskite semiconductors and devices. *APL Materials* **2021,** 9, (10).

99. Xiao, Z.; Yan, Y., Progress in theoretical study of metal halide perovskite solar cell materials. *Advanced Energy Materials* **2017,** 7, (22), 1701136.
100. Motta, C.; El-Mellouhi, F.; Kais, S.; Tabet, N.; Alharbi, F.; Sanvito, S., Revealing the role of organic cations in hybrid halide perovskite CH3NH3PbI3. *Nature communications* **2015,** 6, (1), 7026.
101. Prasanna, R.; Gold-Parker, A.; Leijtens, T.; Conings, B.; Babayigit, A.; Boyen, H.-G.; Toney, M. F.; McGehee, M. D., Band gap tuning via lattice contraction and octahedral tilting in perovskite materials for photovoltaics. *Journal of the American Chemical Society* **2017,** 139, (32), 11117-11124.
102. Protesescu, L.; Yakunin, S.; Bodnarchuk, M. I.; Krieg, F.; Caputo, R.; Hendon, C. H.; Yang, R. X.; Walsh, A.; Kovalenko, M. V., Nanocrystals of cesium lead halide perovskites (CsPbX3, X= Cl, Br, and I): novel optoelectronic materials showing bright emission with wide color gamut. *Nano letters* **2015,** 15, (6), 3692-3696.
103. Gholipour, S.; Saliba, M., Bandgap tuning and compositional exchange for lead halide perovskite materials. In *Characterization Techniques for Perovskite Solar Cell Materials*, Elsevier: 2020; pp 1-22.
104. Walsh, A.; Payne, D. J.; Egdell, R. G.; Watson, G. W., Stereochemistry of post-transition metal oxides: revision of the classical lone pair model. *Chemical Society Reviews* **2011,** 40, (9), 4455-4463.
105. Andalibi, S.; Rostami, A.; Darvish, G.; Moravvej-Farshi, M. K., Band gap engineering of organo metal lead halide perovskite photovoltaic absorber. *Optical and Quantum Electronics* **2016,** 48, 1-12.
106. Houari, M.; Bouadjemi, B.; Matougui, M.; Haid, S.; Lantri, T.; Aziz, Z.; Bentata, S.; Bouhafs, B., Optoelectronic properties of germanium iodide perovskites AGeI 3 (A= K, Rb and Cs): first principles investigations. *Optical and Quantum Electronics* **2019,** 51, 1-14.

107. Miah, M. H.; Khandaker, M. U.; Aminul Islam, M.; Nur-E-Alam, M.; Osman, H.; Ullah, M. H., Perovskite materials in X-ray detection and imaging: recent progress, challenges, and future prospects. *RSC Advances* **2024,** 14, (10), 6656-6698.
108. Bardeen, J.; Shockley, W., Deformation Potentials and Mobilities in Non-Polar Crystals. *Physical Review* **1950,** 80, (1), 72-80.
109. Frost, J. M.; Butler, K. T.; Brivio, F.; Hendon, C. H.; van Schilfgaarde, M.; Walsh, A., Atomistic Origins of High-Performance in Hybrid Halide Perovskite Solar Cells. *Nano Letters* **2014,** 14, (5), 2584-2590.
110. Wang, T.; Daiber, B.; Frost, J. M.; Mann, S. A.; Garnett, E. C.; Walsh, A.; Ehrler, B., Indirect to direct bandgap transition in methylammonium lead halide perovskite. *Energy & Environmental Science* **2017,** 10, (2), 509-515.
111. Hu, Z.; Lin, Z.; Su, J.; Zhang, J.; Chang, J.; Hao, Y., A Review on Energy Band-Gap Engineering for Perovskite Photovoltaics. *Solar RRL* **2019,** 3, (12), 1900304.
112. Zhang, L.; Liu, C.; Wang, L.; Liu, C.; Wang, K.; Zou, B., Pressure-Induced Emission Enhancement, Band-Gap Narrowing, and Metallization of Halide Perovskite Cs3Bi2I9. *Angewandte Chemie International Edition* **2018,** 57, (35), 11213-11217.
113. Zhu, H.; Cai, T.; Que, M.; Song, J.-P.; Rubenstein, B. M.; Wang, Z.; Chen, O., Pressure-Induced Phase Transformation and Band-Gap Engineering of Formamidinium Lead Iodide Perovskite Nanocrystals. *The Journal of Physical Chemistry Letters* **2018,** 9, (15), 4199-4205.
114. Yamada, Y.; Nakamura, T.; Endo, M.; Wakamiya, A.; Kanemitsu, Y., Near-band-edge optical responses of solution-processed organic–inorganic hybrid perovskite CH3NH3PbI3 on mesoporous TiO2 electrodes. *Applied Physics Express* **2014,** 7, (3), 032302.
115. Brivio, F.; Butler, K. T.; Walsh, A.; van Schilfgaarde, M., Relativistic quasiparticle self-consistent electronic structure of hybrid halide perovskite photovoltaic absorbers. *Physical Review B* **2014,** 89, (15), 155204.
116. Filip, M. R.; Eperon, G. E.; Snaith, H. J.; Giustino, F., Steric engineering of metal-halide perovskites with tunable optical band gaps. *Nature Communications* **2014,** 5, (1), 5757.
117. Shockley, W.; Queisser, H. J., Detailed Balance Limit of Efficiency of p-n Junction Solar Cells. *Journal of Applied Physics* **1961,** 32, (3), 510-519.
118. Noh, J. H.; Im, S. H.; Heo, J. H.; Mandal, T. N.; Seok, S. I., Chemical Management for Colorful, Efficient, and Stable Inorganic–Organic Hybrid Nanostructured Solar Cells. *Nano Letters* **2013,** 13, (4), 1764-1769.

119. Eperon, G. E.; Stranks, S. D.; Menelaou, C.; Johnston, M. B.; Herz, L. M.; Snaith, H. J., Formamidinium lead trihalide: a broadly tunable perovskite for efficient planar heterojunction solar cells. *Energy & Environmental Science* **2014,** 7, (3), 982-988.
120. Lehner, A. J.; Fabini, D. H.; Evans, H. A.; Hébert, C.-A.; Smock, S. R.; Hu, J.; Wang, H.; Zwanziger, J. W.; Chabinyc, M. L.; Seshadri, R., Crystal and Electronic Structures of Complex Bismuth Iodides A3Bi2I9 (A = K, Rb, Cs) Related to Perovskite: Aiding the Rational Design of Photovoltaics. *Chemistry of Materials* **2015,** 27, (20), 7137-7148.
121. Liu, C.; Yang, Y.; Rakstys, K.; Mahata, A.; Franckevicius, M.; Mosconi, E.; Skackauskaite, R.; Ding, B.; Brooks, K. G.; Usiobo, O. J., Tuning structural isomers of phenylenediammonium to afford efficient and stable perovskite solar cells and modules. *Nature communications* **2021,** 12, (1), 6394.
122. He, M.; Zheng, D.; Wang, M.; Lin, C.; Lin, Z., High efficiency perovskite solar cells: from complex nanostructure to planar heterojunction. *Journal of Materials Chemistry A* **2014,** 2, (17), 5994-6003.
123. Yun, J. S.; Ho-Baillie, A.; Huang, S.; Woo, S. H.; Heo, Y.; Seidel, J.; Huang, F.; Cheng, Y.-B.; Green, M. A., Benefit of grain boundaries in organic–inorganic halide planar perovskite solar cells. *The journal of physical chemistry letters* **2015,** 6, (5), 875-880.
124. Xing, G.; Mathews, N.; Sun, S.; Lim, S. S.; Lam, Y. M.; Grätzel, M.; Mhaisalkar, S.; Sum, T. C., Long-range balanced electron-and hole-transport lengths in organic-inorganic CH3NH3PbI3. *Science* **2013,** 342, (6156), 344-347.
125. Raoui, Y.; Ez-Zahraouy, H.; Kazim, S.; Ahmad, S., Energy level engineering of charge selective contact and halide perovskite by modulating band offset: Mechanistic insights. *Journal of Energy Chemistry* **2021,** 54, 822-829.
126. Louwen, A.; Van Sark, W.; Schropp, R.; Faaij, A., A cost roadmap for silicon heterojunction solar cells. *Solar Energy Materials and Solar Cells* **2016,** 147, 295-314.
127. Mahmood, K.; Sarwar, S.; Mehran, M. T., Current status of electron transport layers in perovskite solar cells: materials and properties. *Rsc Advances* **2017,** 7, (28), 17044-17062.
128. Bhattarai, S.; Pandey, R.; Madan, J.; Muchahary, D.; Gogoi, D., A novel graded approach for improving the efficiency of Lead-Free perovskite solar cells. *Solar Energy* **2022,** 244, 255-263.
129. Serpetzoglou, E.; Konidakis, I.; Kakavelakis, G.; Maksudov, T.; Kymakis, E.; Stratakis, E., Improved carrier transport in perovskite solar cells probed by femtosecond transient absorption spectroscopy. *ACS Applied Materials & Interfaces* **2017,** 9, (50), 43910-43919.

130. Bhatt, P.; Pandey, K.; Yadav, P.; Tripathi, B.; Pandey, M. K.; Kumar, M., Investigating the charge carrier transport within the hole-transport material free perovskite solar cell processed in ambient air. *Solar energy materials and solar cells* **2015,** 140, 320-327.
131. Liu, Y.; Hong, Z.; Chen, Q.; Chang, W.; Zhou, H.; Song, T.-B.; Young, E.; Yang, Y.; You, J.; Li, G.; Yang, Y., Integrated Perovskite/Bulk-Heterojunction toward Efficient Solar Cells. *Nano Letters* **2015,** 15, (1), 662-668.
132. Wu, W.-Q.; Chen, D.; Caruso, R. A.; Cheng, Y.-B., Recent progress in hybrid perovskite solar cells based on n-type materials. *Journal of Materials Chemistry A* **2017,** 5, (21), 10092-10109.
133. Sakthivel, P.; Foo, S.; Thambidurai, M.; Harikesh, P.; Mathews, N.; Yuvakkumar, R.; Ravi, G.; Dang, C., Efficient and stable planar perovskite solar cells using co-doped tin oxide as the electron transport layer. *Journal of Power Sources* **2020,** 471, 228443.
134. Noh, M. F. M.; Teh, C. H.; Daik, R.; Lim, E. L.; Yap, C. C.; Ibrahim, M. A.; Ludin, N. A.; bin Mohd Yusoff, A. R.; Jang, J.; Teridi, M. A. M., The architecture of the electron transport layer for a perovskite solar cell. *Journal of Materials Chemistry C* **2018,** 6, (4), 682-712.
135. Seo, Y. S.; Lee, C.; Lee, K. H.; Yoon, K. B., 1:1 and 2:1 Charge-Transfer Complexes between Aromatic Hydrocarbons and Dry Titanium Dioxide. *Angewandte Chemie International Edition* **2005,** 44, (6), 910-913.
136. Paik, M. J.; Lee, Y.; Yun, H.-S.; Lee, S.-U.; Hong, S.-T.; Seok, S. I., TiO2 Colloid-Spray Coated Electron-Transporting Layers for Efficient Perovskite Solar Cells. *Advanced Energy Materials* **2020,** 10, (39), 2001799.
137. Thambidurai, M.; Foo, S.; Salim, K. M.; Harikesh, P. C.; Bruno, A.; Jamaludin, N. F.; Lie, S.; Mathews, N.; Dang, C., Improved photovoltaic performance of triple-cation mixed-halide perovskite solar cells with binary trivalent metals incorporated into the titanium dioxide electron transport layer. *Journal of Materials Chemistry C* **2019,** 7, (17), 5028-5036.
138. Chen, Y.; Meng, Q.; Zhang, L.; Han, C.; Gao, H.; Zhang, Y.; Yan, H., SnO2-based electron transporting layer materials for perovskite solar cells: A review of recent progress. *Journal of energy chemistry* **2019,** 35, 144-167.
139. Yang, D.; Yang, R.; Wang, K.; Wu, C.; Zhu, X.; Feng, J.; Ren, X.; Fang, G.; Priya, S.; Liu, S., High efficiency planar-type perovskite solar cells with negligible hysteresis using EDTA-complexed SnO2. *Nature communications* **2018,** 9, (1), 3239.
140. Shao, S.; Loi, M. A., The role of the interfaces in perovskite solar cells. *Advanced Materials Interfaces* **2020,** 7, (1), 1901469.

141. Urieta-Mora, J.; García-Benito, I.; Molina-Ontoria, A.; Martín, N., Hole transporting materials for perovskite solar cells: a chemical approach. *Chemical Society Reviews* **2018,** 47, (23), 8541-8571.
142. Ozturk, T.; Akman, E.; Surucu, B.; Dursun, H.; Ozkaya, V.; Akin, S., The role of pioneering hole transporting materials in new generation perovskite solar cells. *European Journal of Inorganic Chemistry* **2021,** 2021, (41), 4251-4264.
143. Bakr, Z. H.; Wali, Q.; Fakharuddin, A.; Schmidt-Mende, L.; Brown, T. M.; Jose, R., Advances in hole transport materials engineering for stable and efficient perovskite solar cells. *Nano energy* **2017,** 34, 271-305.
144. Alfurayj, I. A.; Li, Z.; Burda, C., Interfaces and interfacial carrier dynamics in perovskites. *The Journal of Physical Chemistry C* **2021,** 125, (28), 15113-15124.
145. Han, Y.; Meyer, S.; Dkhissi, Y.; Weber, K.; Pringle, J. M.; Bach, U.; Spiccia, L.; Cheng, Y.-B., Degradation observations of encapsulated planar CH 3 NH 3 PbI 3 perovskite solar cells at high temperatures and humidity. *Journal of Materials Chemistry A* **2015,** 3, (15), 8139-8147.
146. Wehrenfennig, C.; Eperon, G. E.; Johnston, M. B.; Snaith, H. J.; Herz, L. M., High charge carrier mobilities and lifetimes in organolead trihalide perovskites. *Advanced Materials (Deerfield Beach, Fla.)* **2013,** 26, (10), 1584.
147. Krishna, A.; Grimsdale, A. C., Hole transporting materials for mesoscopic perovskite solar cells–towards a rational design? *Journal of Materials Chemistry A* **2017,** 5, (32), 16446-16466.
148. Kim, G. W.; Choi, H.; Kim, M.; Lee, J.; Son, S. Y.; Park, T., Hole transport materials in conventional structural (n–i–p) perovskite solar cells: from past to the future. *Advanced Energy Materials* **2020,** 10, (8), 1903403.
149. Schloemer, T. H.; Christians, J. A.; Luther, J. M.; Sellinger, A., Doping strategies for small molecule organic hole-transport materials: impacts on perovskite solar cell performance and stability. *Chemical science* **2019,** 10, (7), 1904-1935.
150. Liao, Q.; Wang, Y.; Yao, X.; Su, M.; Li, B.; Sun, H.; Huang, J.; Guo, X., A dual-functional conjugated polymer as an efficient hole-transporting layer for high-performance inverted perovskite solar cells. *ACS Applied Materials & Interfaces* **2021,** 13, (14), 16744-16753.
151. Ščajev, P.; Qin, C.; Aleksiejūnas, R. n.; Baronas, P.; Miasojedovas, S.; Fujihara, T.; Matsushima, T.; Adachi, C.; Juršėnas, S., Diffusion Enhancement in Highly Excited MAPbI3 Perovskite Layers with Additives. *The Journal of Physical Chemistry Letters* **2018,** 9, (12), 3167-3172.

152. Hawash, Z.; Ono, L. K.; Qi, Y., Recent advances in spiro-MeOTAD hole transport material and its applications in organic–inorganic halide perovskite solar cells. *Advanced Materials Interfaces* **2018,** 5, (1), 1700623.
153. Christians, J. A.; Fung, R. C.; Kamat, P. V., An inorganic hole conductor for organo-lead halide perovskite solar cells. Improved hole conductivity with copper iodide. *Journal of the American Chemical Society* **2014,** 136, (2), 758-764.
154. Kung, P. K.; Li, M. H.; Lin, P. Y.; Chiang, Y. H.; Chan, C. R.; Guo, T. F.; Chen, P., A review of inorganic hole transport materials for perovskite solar cells. *Advanced Materials Interfaces* **2018,** 5, (22), 1800882.
155. Singh, R.; Singh, P. K.; Bhattacharya, B.; Rhee, H.-W., Review of current progress in inorganic hole-transport materials for perovskite solar cells. *Applied Materials Today* **2019,** 14, 175-200.
156. Zhao, D.; Yu, Y.; Wang, C.; Liao, W.; Shrestha, N.; Grice, C. R.; Cimaroli, A. J.; Guan, L.; Ellingson, R. J.; Zhu, K., Low-bandgap mixed tin–lead iodide perovskite absorbers with long carrier lifetimes for all-perovskite tandem solar cells. *Nature Energy* **2017,** 2, (4), 1-7.
157. Li, Z.; Yang, M.; Park, J.-S.; Wei, S.-H.; Berry, J. J.; Zhu, K., Stabilizing perovskite structures by tuning tolerance factor: formation of formamidinium and cesium lead iodide solid-state alloys. *Chemistry of Materials* **2016,** 28, (1), 284-292.
158. Rolston, N.; Printz, A. D.; Tracy, J. M.; Weerasinghe, H. C.; Vak, D.; Haur, L. J.; Priyadarshi, A.; Mathews, N.; Slotcavage, D. J.; McGehee, M. D., Effect of cation composition on the mechanical stability of perovskite solar cells. *Advanced Energy Materials* **2018,** 8, (9), 1702116.
159. Mali, S. S.; Patil, J. V.; Arandiyan, H.; Hong, C. K., Reduced methylammonium triple-cation Rb 0.05 (FAPbI 3) 0.95 (MAPbBr 3) 0.05 perovskite solar cells based on a TiO 2/SnO 2 bilayer electron transport layer approaching a stabilized 21% efficiency: the role of antisolvents. *Journal of Materials Chemistry A* **2019,** 7, (29), 17516-17528.
160. Niu, C.; Wang, C.; Zhang, G.; Zhao, Q.; Fang, C.; Li, W.; Huang, F.; Ku, Z.; Cheng, Y.-b., High-Performance Rb–Cs0. 14FA0. 86Pb (BrxI1− x) 3 Perovskite Solar Cells Achieved by Regulating the Halogen Exchange in Vapor–Solid Reaction Process. *Solar Rrl* **2021,** 5, (5), 2100102.
161. Gu, L.; Zhang, D.; Kam, M.; Zhang, Q.; Poddar, S.; Fu, Y.; Mo, X.; Fan, Z., Significantly improved black phase stability of FAPbI 3 nanowires via spatially confined vapor phase growth in nanoporous templates. *Nanoscale* **2018,** 10, (32), 15164-15172.

162. Zheng, X.; Wu, C.; Jha, S. K.; Li, Z.; Zhu, K.; Priya, S., Improved phase stability of formamidinium lead triiodide perovskite by strain relaxation. *ACS Energy Letters* **2016,** 1, (5), 1014-1020.
163. Jeon, N. J.; Noh, J. H.; Yang, W. S.; Kim, Y. C.; Ryu, S.; Seo, J.; Seok, S. I., Compositional engineering of perovskite materials for high-performance solar cells. *Nature* **2015,** 517, (7535), 476-480.
164. Møller, C. K., Crystal structure and photoconductivity of caesium plumbohalides. *Nature* **1958,** 182, (4647), 1436-1436.
165. Karlsson, M.; Yi, Z.; Reichert, S.; Luo, X.; Lin, W.; Zhang, Z.; Bao, C.; Zhang, R.; Bai, S.; Zheng, G., Mixed halide perovskites for spectrally stable and high-efficiency blue light-emitting diodes. *Nature Communications* **2021,** 12, (1), 361.
166. Kim, J. Y.; Lee, J.-W.; Jung, H. S.; Shin, H.; Park, N.-G., High-efficiency perovskite solar cells. *Chemical reviews* **2020,** 120, (15), 7867-7918.
167. Leguy, A. M.; Frost, J. M.; McMahon, A. P.; Sakai, V. G.; Kockelmann, W.; Law, C.; Li, X.; Foglia, F.; Walsh, A.; O'regan, B. C., The dynamics of methylammonium ions in hybrid organic–inorganic perovskite solar cells. *Nature communications* **2015,** 6, (1), 7124.
168. Zhu, H.; Miyata, K.; Fu, Y.; Wang, J.; Joshi, P. P.; Niesner, D.; Williams, K. W.; Jin, S.; Zhu, X.-Y., Screening in crystalline liquids protects energetic carriers in hybrid perovskites. *Science* **2016,** 353, (6306), 1409-1413.
169. Eperon, G. E.; Paternò, G. M.; Sutton, R. J.; Zampetti, A.; Haghighirad, A. A.; Cacialli, F.; Snaith, H. J., Inorganic caesium lead iodide perovskite solar cells. *Journal of Materials Chemistry A* **2015,** 3, (39), 19688-19695.
170. Mailoa, J. P.; Bailie, C. D.; Johlin, E. C.; Hoke, E. T.; Akey, A. J.; Nguyen, W. H.; McGehee, M. D.; Buonassisi, T., A 2-terminal perovskite/silicon multijunction solar cell enabled by a silicon tunnel junction. *Applied Physics Letters* **2015,** 106, (12).
171. Werner, J.; Weng, C.-H.; Walter, A.; Fesquet, L.; Seif, J. P.; De Wolf, S.; Niesen, B.; Ballif, C., Efficient monolithic perovskite/silicon tandem solar cell with cell area> 1 cm2. *The journal of physical chemistry letters* **2016,** 7, (1), 161-166.
172. Wang, Y.; Wang, Y.; Gao, F.; Yang, D., Efficient Monolithic Perovskite/Silicon Tandem Photovoltaics. *Energy & Environmental Materials* **2024,** 7, (3), e12639.
173. Wang, S.; Wang, P.; Chen, B.; Li, R.; Ren, N.; Li, Y.; Shi, B.; Huang, Q.; Zhao, Y.; Grätzel, M., Suppressed recombination for monolithic inorganic perovskite/silicon tandem solar cells with an approximate efficiency of 23%. *Escience* **2022,** 2, (3), 339-346.
174. McMeekin, D. P.; Sadoughi, G.; Rehman, W.; Eperon, G. E.; Saliba, M.; Hörantner, M. T.; Haghighirad, A.; Sakai, N.; Korte, L.; Rech,

B., A mixed-cation lead mixed-halide perovskite absorber for tandem solar cells. *Science* **2016,** 351, (6269), 151-155.
175. Saliba, M.; Matsui, T.; Domanski, K.; Seo, J.-Y.; Ummadisingu, A.; Zakeeruddin, S. M.; Correa-Baena, J.-P.; Tress, W. R.; Abate, A.; Hagfeldt, A., Incorporation of rubidium cations into perovskite solar cells improves photovoltaic performance. *Science* **2016,** 354, (6309), 206-209.
176. Xie, L.-Q.; Chen, L.; Nan, Z.-A.; Lin, H.-X.; Wang, T.; Zhan, D.-P.; Yan, J.-W.; Mao, B.-W.; Tian, Z.-Q., Understanding the cubic phase stabilization and crystallization kinetics in mixed cations and halides perovskite single crystals. *Journal of the American Chemical Society* **2017,** 139, (9), 3320-3323.
177. Bush, K. A.; Palmstrom, A. F.; Yu, Z. J.; Boccard, M.; Cheacharoen, R.; Mailoa, J. P.; McMeekin, D. P.; Hoye, R. L.; Bailie, C. D.; Leijtens, T., 23.6%-efficient monolithic perovskite/silicon tandem solar cells with improved stability. *Nature Energy* **2017,** 2, (4), 1-7.
178. Chen, L.; Tan, Y.-Y.; Chen, Z.-X.; Wang, T.; Hu, S.; Nan, Z.-A.; Xie, L.-Q.; Hui, Y.; Huang, J.-X.; Zhan, C., Toward long-term stability: single-crystal alloys of cesium-containing mixed cation and mixed halide perovskite. *Journal of the American Chemical Society* **2019,** 141, (4), 1665-1671.
179. Al-Ashouri, A.; Köhnen, E.; Li, B.; Magomedov, A.; Hempel, H.; Caprioglio, P.; Márquez, J. A.; Morales Vilches, A. B.; Kasparavicius, E.; Smith, J. A., Monolithic perovskite/silicon tandem solar cell with> 29% efficiency by enhanced hole extraction. *Science* **2020,** 370, (6522), 1300-1309.
180. Ašmontas, S.; Gradauskas, J.; Grigucevičienė, A.; Leinartas, K.; Lučun, A.; Mujahid, M.; Petrauskas, K.; Selskis, A.; Sužiedėlis, A.; Šilėnas, A., Triple-cation perovskite/silicon tandem solar cell. *Ukr. J. Phys. Opt* **2022,** 23, (4), 193.
181. Kivisaari, P., From computational models to improved light-emitting diodes and new devices. **2014**.
182. Kioupakis, E.; Rinke, P.; Delaney, K. T.; Van de Walle, C. G., Indirect Auger recombination as a cause of efficiency droop in nitride light-emitting diodes. *Applied Physics Letters* **2011,** 98, (16).
183. Delaney, K. T.; Rinke, P.; Van de Walle, C. G., Auger recombination rates in nitrides from first principles. *Applied Physics Letters* **2009,** 94, (19).
184. Zhou, Y.; Chen, J.; Bakr, O. M.; Sun, H.-T., Metal-doped lead halide perovskites: synthesis, properties, and optoelectronic applications. *Chemistry of Materials* **2018,** 30, (19), 6589-6613.
185. Stranks, S. D.; Burlakov, V. M.; Leijtens, T.; Ball, J. M.; Goriely, A.; Snaith, H. J., Recombination kinetics in organic-inorganic perovskites: excitons, free charge, and subgap states. *Physical Review Applied* **2014,** 2, (3), 034007.

186. Zhang, Y.; Yin, J.; Parida, M. R.; Ahmed, G. H.; Pan, J.; Bakr, O. M.; Brédas, J.-L.; Mohammed, O. F., Direct-indirect nature of the bandgap in lead-free perovskite nanocrystals. *The Journal of Physical Chemistry Letters* **2017,** 8, (14), 3173-3177.
187. Filip, M. R.; Hillman, S.; Haghighirad, A. A.; Snaith, H. J.; Giustino, F., Band gaps of the lead-free halide double perovskites Cs2BiAgCl6 and Cs2BiAgBr6 from theory and experiment. *The journal of physical chemistry letters* **2016,** 7, (13), 2579-2585.
188. Volonakis, G.; Haghighirad, A. A.; Milot, R. L.; Sio, W. H.; Filip, M. R.; Wenger, B.; Johnston, M. B.; Herz, L. M.; Snaith, H. J.; Giustino, F., Cs2InAgCl6: a new lead-free halide double perovskite with direct band gap. *The journal of physical chemistry letters* **2017,** 8, (4), 772-778.
189. Meng, W.; Wang, X.; Xiao, Z.; Wang, J.; Mitzi, D. B.; Yan, Y., Parity-forbidden transitions and their impact on the optical absorption properties of lead-free metal halide perovskites and double perovskites. *The journal of physical chemistry letters* **2017,** 8, (13), 2999-3007.
190. Price, M. B.; Butkus, J.; Jellicoe, T. C.; Sadhanala, A.; Briane, A.; Halpert, J. E.; Broch, K.; Hodgkiss, J. M.; Friend, R. H.; Deschler, F., Hot-carrier cooling and photoinduced refractive index changes in organic–inorganic lead halide perovskites. *Nature Communications* **2015,** 6, (1), 8420.
191. Boriskina, S. V.; Chen, G., Exceeding the solar cell Shockley–Queisser limit via thermal up-conversion of low-energy photons. *Optics Communications* **2014,** 314, 71-78.
192. Richter, J. M.; Branchi, F.; Valduga de Almeida Camargo, F.; Zhao, B.; Friend, R. H.; Cerullo, G.; Deschler, F., Ultrafast carrier thermalization in lead iodide perovskite probed with two-dimensional electronic spectroscopy. *Nature Communications* **2017,** 8, (1), 376.
193. Guo, Z.; Wan, Y.; Yang, M.; Snaider, J.; Zhu, K.; Huang, L., Long-range hot-carrier transport in hybrid perovskites visualized by ultrafast microscopy. *Science* **2017,** 356, (6333), 59-62.
194. Kahmann, S.; Loi, M. A., Hot carrier solar cells and the potential of perovskites for breaking the Shockley–Queisser limit. *Journal of Materials Chemistry C* **2019,** 7, (9), 2471-2486.
195. Arnold, D.; Cartier, E.; DiMaria, D., Theory of high-field electron transport and impact ionization in silicon dioxide. *Physical Review B* **1994,** 49, (15), 10278.
196. Nozik, A. J., Spectroscopy and hot electron relaxation dynamics in semiconductor quantum wells and quantum dots. *Annual review of physical chemistry* **2001,** 52, (1), 193-231.
197. Burda, C.; Link, S.; Mohamed, M.; El-Sayed, M., The relaxation pathways of CdSe nanoparticles monitored with femtosecond time-

resolution from the visible to the IR: Assignment of the transient features by carrier quenching. *The Journal of Physical Chemistry B* **2001,** 105, (49), 12286-12292.
198. Ross, R. T.; Nozik, A. J., Efficiency of hot-carrier solar energy converters. *Journal of Applied Physics* **1982,** 53, (5), 3813-3818.
199. Fu, J.; Xu, Q.; Han, G.; Wu, B.; Huan, C. H. A.; Leek, M. L.; Sum, T. C., Hot carrier cooling mechanisms in halide perovskites. *Nature communications* **2017,** 8, (1), 1-9.
200. Tsai, C. Y., The effects of intraband and interband carrier-carrier scattering on hot-carrier solar cells: A theoretical study of spectral hole burning, electron-hole energy transfer, Auger recombination, and impact ionization generation. *Progress in Photovoltaics: Research and Applications* **2019,** 27, (5), 433-452.
201. Takeda, Y.; Motohiro, T.; König, D.; Aliberti, P.; Feng, Y.; Shrestha, S.; Conibeer, G., Practical Factors Lowering Conversion Efficiency of Hot Carrier Solar Cells. *Applied Physics Express* **2010,** 3, (10), 104301.
202. Wei, Q.; Yin, J.; Bakr, O. M.; Wang, Z.; Wang, C.; Mohammed, O. F.; Li, M.; Xing, G., Effect of Zinc-doping on the Reduction of the Hot-carrier Cooling Rate in Halide Perovskites. *Angewandte Chemie International Edition* **2021,** 60, (19), 10957-10963.
203. Zhang, P.; Zhu, G.; Shi, Y.; Wang, Y.; Zhang, J.; Du, L.; Ding, D., Ultrafast interfacial charge transfer of cesium lead halide perovskite films CsPbX3 (X= Cl, Br, I) with different halogen mixing. *The Journal of Physical Chemistry C* **2018,** 122, (48), 27148-27155.
204. Chen, J.; Messing, M. E.; Zheng, K.; Pullerits, T., Cation-dependent hot carrier cooling in halide perovskite nanocrystals. *Journal of the American Chemical Society* **2019,** 141, (8), 3532-3540.
205. Yang, J.; Wen, X.; Xia, H.; Sheng, R.; Ma, Q.; Kim, J.; Tapping, P.; Harada, T.; Kee, T. W.; Huang, F., Acoustic-optical phonon up-conversion and hot-phonon bottleneck in lead-halide perovskites. *Nature communications* **2017,** 8, (1), 14120.
206. Shockley, W.; Read Jr, W., Statistics of the recombinations of holes and electrons. *Physical review* **1952,** 87, (5), 835.
207. Green, M. A., Third generation photovoltaics. **2006**.
208. Herz, L. M., Charge-carrier dynamics in organic-inorganic metal halide perovskites. *Annual review of physical chemistry* **2016,** 67, (1), 65-89.
209. Downer, M.; Shank, C., Ultrafast heating of silicon on sapphire by femtosecond optical pulses. *Physical review letters* **1986,** 56, (7), 761.
210. Haug, A., Auger recombination in direct-gap semiconductors: band-structure effects. *Journal of Physics C: Solid State Physics* **1983,** 16, (21), 4159.

211. Ašmontas, S.; Gradauskas, J.; Sužiedėlis, A.; Šilėnas, A.; Širmulis, E.; Vaičikauskas, V.; Vaičiūnas, V.; Žalys, O.; Fedorenko, L.; Bulat, L., Photovoltage formation across GaAs p–n junction under illumination of intense laser radiation. *Optical and Quantum Electronics* **2016,** 48, 1-7.
212. Esmaielpour, H.; Dorman, K. R.; Ferry, D. K.; Mishima, T. D.; Santos, M. B.; Whiteside, V. R.; Sellers, I. R., Exploiting intervalley scattering to harness hot carriers in III–V solar cells. *Nature Energy* **2020,** 5, (4), 336-343.
213. Tran, M. D.; Lee, S.-G.; Jeon, S.; Kim, S.-T.; Kim, H.; Nguyen, V. L.; Adhikari, S.; Woo, S.; Park, H. C.; Kim, Y., Decelerated hot carrier cooling in graphene via nondissipative carrier injection from MoS2. *ACS nano* **2020,** 14, (10), 13905-13912.
214. Chen, Y.; Li, Y.; Zhao, Y.; Zhou, H.; Zhu, H., Highly efficient hot electron harvesting from graphene before electron-hole thermalization. *Science advances* **2019,** 5, (11), eaax9958.
215. Wang, C.; Wei, Q.; Ren, H.; Wong, K. L.; Liu, Q.; Zhou, L.; Wang, P.; Cai, S.; Yin, J.; Li, M., Efficient Gate-Tunable Hot-Carrier Photocurrent from Perovskite Multiple Quantum Wells. *Advanced Materials* **2025,** 37, (5), 2413839.
216. Chen, I.-J.; Limpert, S.; Metaferia, W.; Thelander, C.; Samuelson, L.; Capasso, F.; Burke, A. M.; Linke, H., Hot-carrier extraction in nanowire-nanoantenna photovoltaic devices. *Nano Letters* **2020,** 20, (6), 4064-4072.
217. Yu, Y.; Wijesekara, K. D.; Xi, X.; Willets, K. A., Quantifying wavelength-dependent plasmonic hot carrier energy distributions at metal/semiconductor interfaces. *ACS nano* **2019,** 13, (3), 3629-3637.
218. Ng, C.; Cadusch, J. J.; Dligatch, S.; Roberts, A.; Davis, T. J.; Mulvaney, P.; Gómez, D. E., Hot carrier extraction with plasmonic broadband absorbers. *Acs Nano* **2016,** 10, (4), 4704-4711.
219. Asmontas, S. P.; Gradauskas, J.; Seliuta, D.; Sirmulis, E. In *Photoelectrical properties of nonuniform semiconductor under infrared laser radiation*, Nonresonant Laser-Matter Interaction (NLMI-10), 2001; SPIE: 2001; pp 18-27.
220. Ašmontas, S.; Masalskyi, O.; Zharchenko, I.; Sužiedėlis, A.; Gradauskas, J., Some Aspects of Hot Carrier Photocurrent across GaAs p-n Junction. *Inorganics* **2024,** 12, (6), 174.
221. Ašmontas, S.; Gradauskas, J.; Sužiedélis, A.; Šilénas, A.; Širmulis, E.; Švedas, V.; Vaičikauskas, V.; Vaičiūnas, V.; Žalys, O. Ž.; Kostylyov, V., Photovoltage formation across Si pn junction exposed to laser radiation. *Mater. Sci.-Pol* **2018,** 36, 337-340.
222. Ašmontas, S.; Gradauskas, J.; Sužiedėlis, A.; Šilėnas, A.; Širmulis, E.; Švedas, V.; Vaičikauskas, V.; Žalys, O., Hot carrier impact on photovoltage formation in solar cells. *Applied Physics Letters* **2018,** 113, (7).

223. Aziz, E.; Xiao, J.; Golnak, R.; Tesch, M., Helmholtz-Zentrum Berlin für Materialien und Energie. *J. Large-Scale Res. Facil* **2016,** 2, A80.
224. Li, H.; Zhang, W., Perovskite Tandem Solar Cells: From Fundamentals to Commercial Deployment. *Chemical Reviews* **2020,** 120, (18), 9835-9950.
225. Jimeno, J. C.; Gutierrez, R.; Fano, V.; Habib, A.; del Cañizo, C.; Rasool, M. A.; Otaegi, A., A 3 terminal parallel connected silicon tandem solar cell. *Energy Procedia* **2016,** 92, 644-651.
226. Taguchi, M.; Yano, A.; Tohoda, S.; Matsuyama, K.; Nakamura, Y.; Nishiwaki, T.; Fujita, K.; Maruyama, E., 24.7% record efficiency HIT solar cell on thin silicon wafer. *IEEE Journal of photovoltaics* **2013,** 4, (1), 96-99.
227. Baranwal, A.; Shiki, T.; Ogomi, Y.; Pandey, S.; Ma, T.; Hayase, S., Tandem dye-sensitized solar cells with a back-contact bottom electrode without a transparent conductive oxide layer. *RSC advances* **2014,** 4, (88), 47735-47742.
228. Chiang, S.-Y.; Carbajal, B. G., Tandem junction solar cell. In Google Patents: 1979.
229. Bedair, S.; Lamorte, M.; Hauser, J., A two-junction cascade solar-cell structure. *Applied Physics Letters* **1979,** 34, (1), 38-39.
230. Wang, Y.; Zhang, M.; Xiao, K.; Lin, R.; Luo, X.; Han, Q.; Tan, H., Recent progress in developing efficient monolithic all-perovskite tandem solar cells. *Journal of Semiconductors* **2020,** 41, (5), 051201.
231. Miyata, A.; Mitioglu, A.; Plochocka, P.; Portugall, O.; Wang, J. T.-W.; Stranks, S. D.; Snaith, H. J.; Nicholas, R. J., Direct measurement of the exciton binding energy and effective masses for charge carriers in organic–inorganic tri-halide perovskites. *Nature Physics* **2015,** 11, (7), 582-587.
232. Yang, Z.; Rajagopal, A.; Chueh, C.-C.; Jo, S. B.; Liu, B.; Zhao, T.; Jen, A. K.-Y., Stable low-bandgap Pb-Sn binary perovskites for tandem solar cells. *Advanced Materials* **2016,** 28, (DOE-UW-Jen-33).
233. Nie, W.; Tsai, H.; Asadpour, R.; Blancon, J.-C.; Neukirch, A. J.; Gupta, G.; Crochet, J. J.; Chhowalla, M.; Tretiak, S.; Alam, M. A., High-efficiency solution-processed perovskite solar cells with millimeter-scale grains. *Science* **2015,** 347, (6221), 522-525.
234. Gao, P.; Tsao, H. N.; Teuscher, J.; Grätzel, M., Organic dyes containing fused acenes as building blocks: Optical, electrochemical and photovoltaic properties. *Chinese Chemical Letters* **2018,** 29, (2), 289-292.
235. Di Giacomo, F.; Fakharuddin, A.; Jose, R.; Brown, T. M., Progress, challenges and perspectives in flexible perovskite solar cells. *Energy & Environmental Science* **2016,** 9, (10), 3007-3035.

236. Wang, Z.; Shi, Z.; Li, T.; Chen, Y.; Huang, W., Stability of perovskite solar cells: a prospective on the substitution of the A cation and X anion. *Angewandte Chemie International Edition* **2017,** 56, (5), 1190-1212.
237. Stoumpos, C. C.; Malliakas, C. D.; Kanatzidis, M. G., Semiconducting tin and lead iodide perovskites with organic cations: phase transitions, high mobilities, and near-infrared photoluminescent properties. *Inorganic chemistry* **2013,** 52, (15), 9019-9038.
238. Hao, F.; Stoumpos, C. C.; Chang, R. P.; Kanatzidis, M. G., Anomalous band gap behavior in mixed Sn and Pb perovskites enables broadening of absorption spectrum in solar cells. *Journal of the American Chemical Society* **2014,** 136, (22), 8094-8099.
239. Noel, N. K.; Stranks, S. D.; Abate, A.; Wehrenfennig, C.; Guarnera, S.; Haghighirad, A.-A.; Sadhanala, A.; Eperon, G. E.; Pathak, S. K.; Johnston, M. B., Lead-free organic–inorganic tin halide perovskites for photovoltaic applications. *Energy & Environmental Science* **2014,** 7, (9), 3061-3068.
240. Yang, Z.; Chueh, C.-C.; Liang, P.-W.; Crump, M.; Lin, F.; Zhu, Z.; Jen, A. K.-Y., Effects of formamidinium and bromide ion substitution in methylammonium lead triiodide toward high-performance perovskite solar cells. *Nano Energy* **2016,** 22, 328-337.
241. Brinkmann, K. O.; Becker, T.; Zimmermann, F.; Kreusel, C.; Gahlmann, T.; Theisen, M.; Haeger, T.; Olthof, S.; Tückmantel, C.; Günster, M., Perovskite–organic tandem solar cells with indium oxide interconnect. *Nature* **2022,** 604, (7905), 280-286.
242. Zheng, Z.; Wang, J.; Bi, P.; Ren, J.; Wang, Y.; Yang, Y.; Liu, X.; Zhang, S.; Hou, J., Tandem organic solar cell with 20.2% efficiency. *Joule* **2022,** 6, (1), 171-184.
243. Xia, R.; Xu, Y.; Chen, B.; Kanda, H.; Franckevičius, M.; Gegevičius, R.; Wang, S.; Chen, Y.; Chen, D.; Ding, J.; Yuan, N.; Zhao, Y.; Roldán-Carmona, C.; Zhang, X.; Dyson, P. J.; Nazeeruddin, M. K., Interfacial passivation of wide-bandgap perovskite solar cells and tandem solar cells. *Journal of Materials Chemistry A* **2021,** 9, (38), 21939-21947.
244. Fu, F.; Li, J.; Yang, T. C. J.; Liang, H.; Faes, A.; Jeangros, Q.; Ballif, C.; Hou, Y., Monolithic perovskite-silicon tandem solar cells: from the lab to fab? *Advanced materials* **2022,** 34, (24), 2106540.
245. Tiedje, T.; Yablonovitch, E.; Cody, G. D.; Brooks, B. G., Limiting efficiency of silicon solar cells. *IEEE Transactions on electron devices* **1984,** 31, (5), 711-716.
246. Chen, Z.; Li, X.; Guo, X., Enhanced absorption in perovskite solar cells by incorporating gold triangle nanostructures. *Applied Optics* **2023,** 62, (19), 5064-5068.

247. Wu, X.; Liu, Y.; Qi, F.; Lin, F.; Fu, H.; Jiang, K.; Wu, S.; Bi, L.; Wang, D.; Xu, F., Improved stability and efficiency of perovskite/organic tandem solar cells with an all-inorganic perovskite layer. *Journal of Materials Chemistry A* **2021,** 9, (35), 19778-19787.
248. Chang, C.-Y.; Tsai, B.-C.; Hsiao, Y.-C.; Lin, M.-Z.; Meng, H.-F., Solution-processed conductive interconnecting layer for highly-efficient and long-term stable monolithic perovskite tandem solar cells. *Nano Energy* **2019,** 55, 354-367.
249. Gao, P.; Bin Mohd Yusoff, A. R.; Nazeeruddin, M. K., Dimensionality engineering of hybrid halide perovskite light absorbers. *Nature communications* **2018,** 9, (1), 5028.
250. Juarez-Perez, E. J.; Haro, M., Perovskite solar cells take a step forward. *Science* **2020,** 368, (6497), 1309-1309.
251. Shi, L.; Bucknall, M. P.; Young, T. L.; Zhang, M.; Hu, L.; Bing, J.; Lee, D. S.; Kim, J.; Wu, T.; Takamure, N., Gas chromatography–mass spectrometry analyses of encapsulated stable perovskite solar cells. *Science* **2020,** 368, (6497), eaba2412.
252. Pellet, N.; Gao, P.; Gregori, G.; Yang, T. Y.; Nazeeruddin, M. K.; Maier, J.; Grätzel, M., Mixed-organic-cation Perovskite photovoltaics for enhanced solar-light harvesting. *Angewandte Chemie International Edition* **2014,** 53, (12), 3151-3157.
253. Yi, C.; Luo, J.; Meloni, S.; Boziki, A.; Ashari-Astani, N.; Grätzel, C.; Zakeeruddin, S. M.; Röthlisberger, U.; Grätzel, M., Entropic stabilization of mixed A-cation ABX 3 metal halide perovskites for high performance perovskite solar cells. *Energy & Environmental Science* **2016,** 9, (2), 656-662.
254. Hoke, E. T.; Slotcavage, D. J.; Dohner, E. R.; Bowring, A. R.; Karunadasa, H. I.; McGehee, M. D., Reversible photo-induced trap formation in mixed-halide hybrid perovskites for photovoltaics. *Chemical Science* **2015,** 6, (1), 613-617.
255. Anaya, M.; Lozano, G.; Calvo, M. E.; Míguez, H., ABX3 perovskites for tandem solar cells. *Joule* **2017,** 1, (4), 769-793.
256. Xiong, S.; Hou, Z.; Dong, W.; Li, D.; Yang, J.; Bai, R.; Wu, Y.; Li, D.; Wu, H.; Ma, Z., Additive-induced synergies of defect passivation and energetic modification toward highly efficient perovskite solar cells. *Advanced Energy Materials* **2021,** 11, (29), 2101394.
257. Sahli, F.; Werner, J.; Kamino, B. A.; Bräuninger, M.; Monnard, R.; Paviet-Salomon, B.; Barraud, L.; Ding, L.; Diaz Leon, J. J.; Sacchetto, D., Fully textured monolithic perovskite/silicon tandem solar cells with 25.2% power conversion efficiency. *Nature materials* **2018,** 17, (9), 820-826.
258. Azmi, R.; Ugur, E.; Seitkhan, A.; Aljamaan, F.; Subbiah, A. S.; Liu, J.; Harrison, G. T.; Nugraha, M. I.; Eswaran, M. K.; Babics, M.,

Damp heat–stable perovskite solar cells with tailored-dimensionality 2D/3D heterojunctions. *Science* **2022,** 376, (6588), 73-77.
259. Liu, J.; Aydin, E.; Yin, J.; De Bastiani, M.; Isikgor, F. H.; Rehman, A. U.; Yengel, E.; Ugur, E.; Harrison, G. T.; Wang, M., 28.2%-efficient, outdoor-stable perovskite/silicon tandem solar cell. *Joule* **2021,** 5, (12), 3169-3186.
260. Liu, J.; De Bastiani, M.; Aydin, E.; Harrison, G. T.; Gao, Y.; Pradhan, R. R.; Eswaran, M. K.; Mandal, M.; Yan, W.; Seitkhan, A., Efficient and stable perovskite-silicon tandem solar cells through contact displacement by MgF x. *Science* **2022,** 377, (6603), 302-306.
261. Werner, J.; Geissbühler, J.; Dabirian, A.; Nicolay, S.; Morales-Masis, M.; Wolf, S. D.; Niesen, B.; Ballif, C., Parasitic absorption reduction in metal oxide-based transparent electrodes: application in perovskite solar cells. *ACS applied materials & interfaces* **2016,** 8, (27), 17260-17267.
262. Mailoa, J. P.; Bailie, C. D.; Akey, A. J.; Hoke, E. T.; Johlin, E. C.; Nguyen, W. H.; Sofia, S. E.; McGehee, M. D.; Buonassisi, T. In *Optical loss analysis of monolithic perovskite/Si tandem solar cell*, 2015 IEEE 42nd Photovoltaic Specialist Conference (PVSC), 2015; IEEE: 2015; pp 1-3.
263. Jiang, Y.; Almansouri, I.; Huang, S.; Young, T.; Li, Y.; Peng, Y.; Hou, Q.; Spiccia, L.; Bach, U.; Cheng, Y.-B., Optical analysis of perovskite/silicon tandem solar cells. *Journal of Materials Chemistry C* **2016,** 4, (24), 5679-5689.
264. Söderström, T.; Haug, F.-J.; Niquille, X.; Terrazzoni, V.; Ballif, C., Asymmetric intermediate reflector for tandem micromorph thin film silicon solar cells. *Applied Physics Letters* **2009,** 94, (6).
265. Bittkau, K.; Kirchartz, T.; Rau, U., Optical design of spectrally selective interlayers for perovskite/silicon heterojunction tandem solar cells. *Optics express* **2018,** 26, (18), A750-A760.
266. Albrecht, S.; Saliba, M.; Baena, J. P. C.; Lang, F.; Kegelmann, L.; Mews, M.; Steier, L.; Abate, A.; Rappich, J.; Korte, L., Monolithic perovskite/silicon-heterojunction tandem solar cells processed at low temperature. *Energy & Environmental Science* **2016,** 9, (1), 81-88.
267. Zhang, J.; Li, J.; Zheng, L.; Lu, Y.; Moulin, E.; Haug, F.-J.; Ballif, C.; Xu, H.; Dai, N.; Song, W., Simultaneous realization of light distribution and trapping in micromorph tandem solar cells using novel double-layered antireflection coatings. *Solar Energy Materials and Solar Cells* **2015,** 143, 546-552.
268. Ahmed, I.; Shi, L.; Pasanen, H.; Vivo, P.; Maity, P.; Hatamvand, M.; Zhan, Y., There is plenty of room at the top: generation of hot charge carriers and their applications in perovskite and other semiconductor-based optoelectronic devices. *Light: Science & Applications* **2021,** 10, (1), 174.

269. Yang, Y.; Ostrowski, D. P.; France, R. M.; Zhu, K.; van de Lagemaat, J.; Luther, J. M.; Beard, M. C., Observation of a hot-phonon bottleneck in lead-iodide perovskites. *Nature Photonics* **2016,** 10, (1), 53-59.
270. Bush, K. A.; Palmstrom, A. F.; Yu, Z. J.; Boccard, M.; Cheacharoen, R.; Mailoa, J. P.; McMeekin, D. P.; Hoye, R. L. Z.; Bailie, C. D.; Leijtens, T.; Peters, I. M.; Minichetti, M. C.; Rolston, N.; Prasanna, R.; Sofia, S.; Harwood, D.; Ma, W.; Moghadam, F.; Snaith, H. J.; Buonassisi, T.; Holman, Z. C.; Bent, S. F.; McGehee, M. D., 23.6%-efficient monolithic perovskite/silicon tandem solar cells with improved stability. *Nature Energy* **2017,** 2, (4), 17009.
271. Chen, C.; Song, Z.; Xiao, C.; Zhao, D.; Shrestha, N.; Li, C.; Yang, G.; Yao, F.; Zheng, X.; Ellingson, R. J.; Jiang, C.-S.; Al-Jassim, M.; Zhu, K.; Fang, G.; Yan, Y., Achieving a high open-circuit voltage in inverted wide-bandgap perovskite solar cells with a graded perovskite homojunction. *Nano Energy* **2019,** 61, 141-147.
272. Tong, J.; Jiang, Q.; Zhang, F.; Kang, S. B.; Kim, D. H.; Zhu, K., Wide-Bandgap Metal Halide Perovskites for Tandem Solar Cells. *ACS Energy Lett* **2021,** 6, (1), 232-248.
273. Finkenauer, B. P.; Akriti; Ma, K.; Dou, L., Degradation and Self-Healing in Perovskite Solar Cells. *ACS Applied Materials & Interfaces* **2022,** 14, (21), 24073-24088.
274. Fan, K.; Chan, C. C. S.; Yuan, L.; Yan, K.; Wong, K. S., New Insights into Hot-Charge Relaxation in Lead Halide Perovskite: Dynamical Bandgap Change, Hot-Biexciton Effect, and Photo-Bleaching Shift. *ACS Photonics* **2022,** 9, (7), 2304-2314.
275. Chauhan, A. K.; Kumar, P., Degradation in perovskite solar cells stored under different environmental conditions. *Journal of Physics D: Applied Physics* **2017,** 50, (32), 325105.
276. Ke, W.; Stoumpos, C. C.; Zhu, M.; Mao, L.; Spanopoulos, I.; Liu, J.; Kontsevoi, O. Y.; Chen, M.; Sarma, D.; Zhang, Y., Enhanced photovoltaic performance and stability with a new type of hollow 3D perovskite {en} FASnI3. *Science advances* **2017,** 3, (8), e1701293.
277. Eperon, G. E.; Burlakov, V. M.; Docampo, P.; Goriely, A.; Snaith, H. J., Morphological control for high performance, solution-processed planar heterojunction perovskite solar cells. *Advanced functional materials* **2014,** 24, (1), 151-157.
278. Deshpande, S. S.; Saykar, N. G.; Mandal, A.; Rahane, S.; Jadhav, Y. A.; Upadhyay Kahaly, M.; Nagy, G.; Shinde, A.; Suresh, S.; Rondiya, S. R., Unravelling Structural, Optical, and Band Alignment Properties of Mixed Pb–Sn Metal-Halide Quasi-2D Ruddlesden–Popper Perovskites. *Langmuir* **2024,** 40, (31), 16180-16189.

279. Messing, G. L.; Zhang, S.-C.; Jayanthi, G. V., Ceramic Powder Synthesis by Spray Pyrolysis. *Journal of the American Ceramic Society* **1993,** 76, (11), 2707-2726.
280. Emslie, A. G.; Bonner, F. T.; Peck, L. G., Flow of a Viscous Liquid on a Rotating Disk. *Journal of Applied Physics* **1958,** 29, (5), 858-862.
281. Chen, X.; Hu, Y.; Xie, Z.; Wang, H., Materials and design of photocatalytic membranes. In *Current Trends and Future Developments on (Bio-) Membranes*, Elsevier: 2018; pp 71-96.
282. Yamamoto, K.; Yoshida, Y.; Murakami, T. N., Rapid oxygen plasma treatment of tin oxide layers for improving the light stability of perovskite solar cells. *Japanese Journal of Applied Physics* **2024,** 63, (9), 090903.
283. Ruf, F.; Aygüler, M. F.; Giesbrecht, N.; Rendenbach, B.; Magin, A.; Docampo, P.; Kalt, H.; Hetterich, M., Temperature-dependent studies of exciton binding energy and phase-transition suppression in (Cs, FA, MA) Pb (I, Br) 3 perovskites. *Apl Materials* **2019,** 7, (3).
284. Poli, I.; Ambrosio, F.; Treglia, A.; Berger, F. J.; Prato, M.; Albaqami, M. D.; De Angelis, F.; Petrozza, A., Photoluminescence intensity enhancement in tin halide perovskites. *Advanced Science* **2022,** 9, (32), 2202795.
285. Berberan-Santos, M. N., A luminescence decay function encompassing the stretched exponential and the compressed hyperbola. *Chemical Physics Letters* **2008,** 460, (1-3), 146-150.
286. Gradauskas, J.; Ašmontas, S.; Sužiedėlis, A.; Šilėnas, A.; Vaičikauskas, V.; Čerškus, A.; Širmulis, E.; Žalys, O.; Masalskyi, O., Influence of hot carrier and thermal components on photovoltage formation across the p–n junction. *Applied Sciences* **2020,** 10, (21), 7483.
287. Masalskyi, O.; Gradauskas, J., Pre-themalizational effect of hot carriers on photovoltage formation in a solar cell. **2022**.
288. Li, Y.; Ji, L.; Liu, R.; Zhang, C.; Mak, C. H.; Zou, X.; Shen, H.-H.; Leu, S.-Y.; Hsu, H.-Y., A review on morphology engineering for highly efficient and stable hybrid perovskite solar cells. *Journal of Materials Chemistry A* **2018,** 6, (27), 12842-12875.
289. Singh, T.; Miyasaka, T., Stabilizing the efficiency beyond 20% with a mixed cation perovskite solar cell fabricated in ambient air under controlled humidity. *Advanced Energy Materials* **2018,** 8, (3), 1700677.

NOTES

NOTES

Vilnius University Press
9 Saulėtekio Ave., Building III, LT-10222 Vilnius
Email: info@leidykla.vu.lt, www.leidykla.vu.lt
bookshop.vu.lt, journals.vu.lt
Print run copies 20